IMPERIAL

IMPERIAL COLLEGE LONDON

DEPARTMENT OF PHYSICS

Cold Atom-Based Quantum Technology for Probing Fundamental Physics

Elizabeth Pasatembou

Supervised by Dr Charles Baynham and Prof. Oliver Buchmueller

2025

Submitted in part fulfilment of the requirements for the degree of Doctor of Philosophy in Physics of Imperial College London and the Diploma of Imperial College London.

Declaration of Originality

I, Elizabeth Pasatembou, declare that the work presented in this thesis is my own, unless otherwise stated. Where the work of others has been used, it is appropriately referenced. A full list of references is provided in the bibliography. In the case of collaborative work, the contributions of others are clearly identified in the relevant chapters.

Chapter 1 contextualises the original work presented in this thesis. Chapter 2 provides an overview of the AION experiment, atom interferometry and how it can be used to detect ultra-light dark matter and gravitational waves. These two chapters were prepared solely for this thesis.

The subsequent chapters (3 - 5) are based on original work carried out as part of this PhD. Chapter 3 draws on Refs. [1] & [2]. Chapter 4 is based on [2]. Chapter 5 is based on Ref. [3] with additional work carried out specifically for this thesis.

Abstract

Advancing our knowledge of the universe increasingly relies on technologies capable of extremely precise measurement. Quantum sensors have emerged as promising tools for searching for new physics by pushing the boundaries of precision in measuring time, acceleration, and gravity. Two promising platforms are long baseline atom interferometers and atomic clocks, both of which rely on cold atoms. This thesis lies at the intersection of cold-atom physics, quantum technology, and particle phenomenology.

We report experimental progress from the AION project, a next-generation atom interferometer for ultra-light dark matter and mid-frequency gravitational waves detection. We report the first results from a red magneto-optical (MOT) for ^{88}Sr atoms within the collaboration. A seed–amplifier injection-locked laser system was developed to address the $^1S_0$–$^3P_1$ transition at 689 nm, delivering 13.8 mW of light to the science chamber. Using this setup, we produced an atomic cloud at a temperature of (812 ± 4) nK in the narrow-band red MOT, marking a critical milestone in the project.

Secondly, the potential of next-generation atomic and molecular clocks in constraining theories that violate the weak equivalence principle (EP) is investigated. A search for variations in the electron-proton mass ratio is performed using publicly available data from UTC. A statistical framework is then developed to model clock noise and forecast sensitivity to signals arising in theories of dark matter, dark energy, unification, and other EP-violating scenarios, providing new, improved constraints. The framework is packaged into a tool that can be used to translate clock noise characteristics into constraints in the fundamental physics theories presented. A preliminary study, investigating the effect of

data gaps in signal recovery, shows that annual signals with amplitudes above 10^{-16} can be recovered even with up to 83% missing data.

Acknowledgements

First and foremost, I would like to thank my supervisor, Dr. Charles Baynham, for his continuous guidance and invaluable feedback throughout my PhD. His expertise and mentorship were instrumental to the successful completion of this work. I am also grateful to Professor Oliver Buchmueller for the opportunity to join his group, for his guidance, and for providing the resources that enabled this research.

I would also like to thank the rest of the AION team at Imperial, including Dr Richard Hobson, for his valuable guidance and support in the lab. Thank you to Tom, Ludo, Alice, and Leonie for sharing the lab and office with me, for the conversations and encouragement along the way, and for their contributions to the AION project work. I am also grateful to the wider AION collaboration for their contributions to the project; attending AION Days and meeting everyone was undoubtedly one of the highlights of my PhD. A special thank you to Michael, who started this PhD journey with me and became a great friend along the way. I am especially grateful to have crossed paths with David, who was a wonderful labmate and an even greater friend.

It was an immense pleasure to collaborate with Dr Benjamin Elder, Giorgio Mentasti, Prof. Carlo R. Contaldi, Prof. Claudia de Rham and Prof. Andrew J. Tolley on the "clocks-theory" project. Thank you all for the insightful discussions, and a special thank you to Ben and Giorgio for the hard work you put into the project, the many hours we spent discussing science, your encouragement, and the friendly conversations along the way.

Thank you also to the rest of my HEP friends who supported me along the journey and were always happy to lend an ear. To my PhD cohort, Jay, Naseem, Josie, Alie, James, Teddy, Kai and Jake, I feel lucky to have shared this experience with you. Thank you also to Mikael, Irene, Tiago, Koustubh, Rehanah, George, Lucas and Simon. I am forever grateful for Prof. Mitesh Patel's guidance and support. To the fundies: your support has been invaluable. And thank you, Mrs Paula B., for all that you do.

My time at Imperial was made extra special thanks to Prof. Peter Haynes and Dr Craig Whittall, who trusted me with the QuEST policy engagement role. Thank you for all the opportunities and guidance. I had the great pleasure to work alongside some of the most visionary and dedicated people who made me believe that together we can change the world; so thank you, Dimitrie Cielecki and Dr Jess Wade. Thank you also to Miranda and Isabella.

I would also like to thank the mentors, both inside and outside academia, who have encouraged, guided, and supported me over the years: Rupesh, Louise, Sarah, and Stella. A heartfelt thank you to my high school physics teacher, Dr Stelios Tsangarides, and my first science teacher, Dr Irene Hadjisavva. Your encouragement was a turning point, and I carry that with me to this day.

To my friends, thank you for being there through highs and lows. Thank you to Maria, Marios, Chadjis, Charis, Andreas H., Konstantinos, Ioannis, Lefteris, Andreas C., Michalis, Menelaos, Ektoras, and Anna-Maria. A special thank you to Eleni P. and my flatmate, Maria. Your support means more than you know.

Above all, I am grateful to my family; their unconditional love and sacrifices have made this thesis possible. To my yiayia Eleni, yiayia Elsa, pappous Grigoris, thank you for all the wisdom, kindness, and support throughout this journey; it means the world to

me. To my sisters, Eleni and Filio, thank you for being my cheerleaders and everyday supporters, and for always believing in me. To Carol, my childhood friend turned sister, I am forever thankful for your support and encouragement. I would also like to thank my godmother Eleni, godfather Avramis, Litsa, Kleanthis, Frankie, and my uncle Mike for their support throughout this journey. To my partner, Klitos, I couldn't have done this without you. Thank you for being by my side, supporting me every step of the way, and always believing in me. Τέλος, στη μαμά μου, Χριστίνα, και στον μπαμπά μου, Άριστο, τίποτα από αυτά δεν θα ήταν δυνατό χωρίς τη στήριξη και τις θυσίες σας. Ευχαριστώ που ποτέ δεν αμφιβάλατε ότι μπορώ να καταφέρω ό,τι βάλω στο μυαλό μου. Αυτό το επίτευγμα είναι τόσο δικό σας όσο και δικό μου.

Dedication

In loving memory of pappous Avramis, whose love of nature continues to inspire me.

Contents

Chapter 1

Introduction

Despite the remarkable progress of modern physics in the last century, from the discovery of quantum mechanics to the formulation of general relativity, many of the universe's deepest mysteries remain unsolved. Approximately 95% of the total energy density of the universe remains unaccounted for, approximately 68% of which is thought to be dark energy [4]. This energy is believed to be responsible for the universe's accelerated expansion, which cannot be explained by the Standard Model (SM) of elementary particles and fields. Numerous theoretical models have been proposed to address these gaps in our knowledge about the universe. These models often introduce new scalar or vector fields [5, 6, 7], modifications to general relativity [8, 9], new particles and novel interactions [10, 11], modifications to the properties of existing SM particles or the graviton [12].

Astrophysical and cosmological evidence strongly supports the existence of dark matter, which is thought to constitute approximately 85% of the mass content of the universe [4]. Observations of galactic rotation curves [13, 14], gravitational lensing [15], and the cosmic microwave background [16] all point to a nonluminous component that interacts

gravitationally but not electromagnetically with visible matter [17]. While the standard model assumes purely gravitational interaction, some theoretical extensions allow for extremely weak couplings to ordinary matter. Although early theoretical efforts focused on weakly interacting massive particles (WIMPs), increasing attention has shifted toward alternative models, including ultralight dark matter (ULDM), due to the lack of evidence of the existence of WIMPs at particle colliders [18, 19] or heavy nuclear target deep-underground experiments [20]. ULDM can be modelled as a bosonic field with a mass as low as 10^{-24} eV [21, 22]. These fields move non-relativistically through the Universe by forming coherent waves and give rise to various time-dependent signals. In the context of a scalar ULDM candidate, the field couples to SM particles, inducing time-dependent slow drifts or oscillations in fundamental constants [23, 24]. In theories involving vector candidates, apparent violations of the equivalence principle can be observed due to time-dependent differences in accelerations between different species of atoms [25].

Gravitational waves (GWs), first directly detected by LIGO [26] and Virgo [27] in 2015 [28, 29], provide another window into new physics. Their detection shines light onto new phenomena such as mergers of black holes (BHs) and neutron stars (NSs). GWs originating from these sources produce high-frequency signals ($\sim$10–1000 Hz) to which existing experiments such as LIGO and Virgo are sensitive. It is, however, known that much more massive black holes than those detected by these experiments (i.e. supermassive BHs (SMBHs)) exist in the cores of galaxies, the mergers and binary systems of which are the main target of the space-borne LISA [30] experiment. Evidence of nHz scale GWs has recently been discovered by pulsar timing arrays [31]. However, many expected sources of gravitational waves, including intermediate-mass black hole (IMBH) mergers, cosmological phase transitions, or new relic backgrounds from the early universe, lie in a poorly explored mid-frequency band ($\sim$0.1–10 Hz) [32, 33]. Filling this observational

gap requires novel detection strategies.

Dark energy (DE) [34], which is theorised to drive the accelerated expansion of the universe and estimated to make up to 68% of the total energy of the universe, remains even more enigmatic. Its simplest form, a cosmological constant (Λ), introduces a severe fine-tuning problem in quantum field theory, where the vacuum energy predicted is orders of magnitude larger than observed. Alternative models have been proposed, including dynamical scalar field models, e.g. quintessence [35], where dark energy arises from a slowly evolving scalar field $\phi(t)$ rolling down a self-interaction potential $V(\phi)$. Modified gravity theories [12] have also been proposed to explain the mystery of the accelerated expansion of the universe through modifications to general relativity on large cosmological scales.

Progress towards answering these questions is increasingly constrained by our experimental capabilities and our capacity to test for the theories rather than by theoretical limitations. The next generation of scientific breakthroughs requires new experimental approaches that can probe new physics at unprecedented scales of precision and sensitivity.

1.1 Cold Atoms based Quantum Sensors for Fundamental Physics

Parallel to advancements in theoretical physics, we have seen accelerated technological advancements in a new class of technologies, namely quantum technologies, in recent years. This year marks a century since the initial development of quantum mechanics [36], and what was once physics confined only to thought experiments has given rise to a

powerful set of technologies.

Quantum technologies use the properties of quantum systems, such as entanglement and superposition, to perform measurements to a much higher precision than classical technologies can reach. Among these are quantum sensors, which are especially powerful for testing fundamental physics as they offer unparalleled precision in measuring time, acceleration, rotation, and gravity.

At the heart of a class of these sensors are ultra-cold atoms, whose well-controlled quantum states enable interferometry and high-precision spectroscopy. Two key modalities have emerged as promising in testing various fundamental physics theories:

- **Atom Interferometers (AIs)**: Use matter-wave interference to measure gravitational acceleration, gravity gradients, accelerations, rotations and fundamental constants with high precision. Long-baseline differential atom interferometers can be used to search for gravitational wave signals, test the equivalence principle, and detect ultralight dark matter.

- **Atomic Clocks**: Use atomic transitions as a time reference, enabling tests of possible variation of fundamental constants over time caused by scalar fields and tests of general relativity.

Both atomic clocks and most atom interferometers operate using a Ramsey-type configuration, but they are applied to different metrological goals. In Ramsey spectroscopy, a central technique to both technologies, a sequence of coherent pulses prepares the atoms in a superposition of two states, allowing the relative phase to evolve freely. The atomic wave packets are then recombined to extract the accumulated phase information [37]. In atomic clocks, the phase accumulated during Ramsey interrogation is compared to a sta-

ble local oscillator. By tuning the oscillator frequency to the atomic transition and locking it to the central Ramsey fringe, precise measurements of atomic transition frequencies and the realisation of highly stable time standards are achieved [38]. Many atom interferometers use Ramsey-type light-pulse sequences in which the phase evolution is affected by external factors such as the atomic trajectories, making them sensitive to inertial effects like acceleration and rotation [39]. Thus, while both atomic clocks and atom interferometers rely on coherent splitting and recombination of matter waves, clocks are used in frequency metrology by optimising the coherence of the internal state, whereas interferometers use the spatially separated paths to probe for changes in the environment and test fundamental physics.

These two types of technology are not only complementary when testing for new physics but also share common experimental platforms. Therefore, they are a foundation for interdisciplinary efforts at the intersection of atomic physics, quantum technology, and particle phenomenology.

This thesis situates itself at this intersection. This work is part of a wider effort where the development of new technology, in this case cold-atom technology, and fundamental physics inform each other. Instrumentation and technological advancements make it possible to test new theories, while unanswered fundamental physics questions can help shape the direction of the technology itself. Therefore, this area of work is not only of high scientific significance but can also drive societal and technological impact.

As scientific inquiry drives technological advancement, pushing for more precise instrumentation and innovative technologies, the technology can have applications outside of science. Beyond their role in fundamental science, cold atom technologies, including atomic clocks and AIs, are enabling advances in navigation, communication, metrology,

and geophysical monitoring, which have significant implications in critical infrastructure, national security, and environmental and climate change monitoring, to name a few examples.

1.2 Summary of Research Areas

This thesis presents research at the intersection of cold atom quantum sensing and fundamental physics, focusing on two strands:

1.2.1 Ultra-cold atoms for AION (experimental work)

Chapters 3 and 4 describe my contributions to the Atom Interferometry Observatory and Network (AION) project, a next-generation atom interferometer aiming to detect mid-frequency range gravitational waves and ultra-light dark matter. My work includes hardware development and characterisation for the production of ultra-cold atoms as part of the efforts to carry out research and development on the technology that will underpin the development of the detector.

I contributed to establishing a state-of-the-art cold-atom lab, transforming an empty room into a functioning experimental facility for the AION project and beyond. The work included building and testing laser systems used in the AION project, as well as the vacuum chambers where cold-atom and tabletop-atom interferometer experiments have been performed.

1.2.2 Atomic clocks for dark physics searches (particle phenomenology)

Chapter 5 focuses on atomic clocks as probes of new physics. We investigate the sensitivity of various species of clocks to variations in fundamental constants, using simulated data and a statistical framework to explore phenomenological models involving scalar fields and dark matter couplings. We develop an easy to use framework that can be used by scientists operating clocks around the world to derive constraints on a set of models for modified gravity, dark matter and dark energy, which has been made publicly available.

While the earlier chapters focus on the development and characterisation of cold atom systems for atom interferometry, the final part of this thesis explores how atomic clocks, another cold-atom-based platform, can be used to test theories of fundamental physics. Both technologies share common experimental foundations, relying on ultra-cold atoms and precise control using lasers, but they can probe different but sometimes complementary aspects of new physics. Atom interferometers are sensitive to forces like gravity and acceleration, whereas atomic clocks can detect time variations in fundamental constants linked to scalar fields. By developing a statistical framework to connect noisy clock data with phenomenological models, the last part of this thesis complements the experimental work, showing how cold atom technologies can be used in different but connected ways to search for dark matter, dark energy, and violations of the equivalence principle.

1.3 Broader Contributions and Engagement

In parallel with the research presented in this thesis, I have been involved in a range of activities at the intersection of science, policy, and society.

Building a large-scale atom interferometer for scientific exploration requires collaboration at the international level. I was actively involved in the organisation of the founding *Terrestrial very-long-baseline atom interferometry* workshops, bringing together researchers from different institutions with the aim to lay the groundwork for an international TVL-BAI proto-collaboration. The summaries of the workshops are found in Ref. [40] and [41]. I organised the early career researchers' (ECRs) poster session for the second workshop and contributed to the writing of the summary paper by highlighting the importance of the engagement of ECRs in the success of such a collaboration.

Engagement of scientists with policy is essential not only to inform evidence-based decision-making but also to help ensure that emerging technologies are developed responsibly and in ways that benefit society. During my PhD, I contributed to national policy discussions on quantum technologies focused on their future development and societal impact. I contributed to the UK government's Regulatory Horizons Council's (RHC) reports on Regulating Quantum Technology Applications [42] and the Future Regulation of Space Technologies [43] (advocating for quantum technology as one of the critical space technologies). I also led and facilitated discussions between policymakers and researchers, which informed the UK Parliament's research briefing (POSTnote) on Quantum Computing, Sensing and Communications [44], highlighting the benefits and risks of quantum technologies.

Throughout my PhD, I have actively led and contributed to science outreach and public engagement activities aimed at making quantum technologies and fundamental physics more accessible to wider audiences. I have organised and delivered talks and workshops for school students and the general public, engaging thousands of people with scientific concepts related to my research. These activities have allowed me to communicate complex ideas in clear and engaging ways and have strengthened my belief in the importance

of inclusive, accessible science communication.

These experiences, while not directly part of the thesis research, have shaped the kind of scientist I am today and how I think about the role of science in society, the importance of evidence-informed policymaking, and the importance of building collaborative, interdisciplinary communities around emerging technologies and scientific research.

1.4 Thesis Overview

An overview of the AION project and how atom interferometers work is presented in Chapter 2 of this thesis. The chapter also provides an overview of the atom interferometry landscape and the scientific goals of AION, showcasing how AION complements the efforts of other experiments searching for ULDM and GWs.

The subsequent two chapters focus on my work in relation to the AION project. Chapter 3 presents the development and building of the apparatus at the Imperial AION lab, which is used for R&D purposes relating to preparing cold atoms and performing atom interferometry experiments. I present my contributions to setting up the lab and building the vacuum chambers and laser system for cooling atoms down to sub-micro-kelvin temperatures in a 3D red magneto-optical trap (MOT) using the 689 nm transition in strontium-88. Chapter 4 presents the first results from the red MOT of the collaboration, which marked a significant milestone in the development of the project, proving that the apparatus is capable of reaching temperatures that allow for the subsequent steps of the experiment to take place, including enabling atom interferometry. A significant part of these chapters is based on Ref.[1] and [2].

Chapter 5 is based on Ref. [3] and presents a set of theories relating to dark matter, dark

energy and modified gravity that can cause variations in the proton-to-electron mass ratio (μ). This work develops and applies a forecasting framework using simulated data to assess how next-generation atomic clocks can improve constraints on these theories, particularly those predicting linear drifts or oscillations in clock transition frequencies and in particular μ. The analysis highlights the potential of optical, molecular, and nuclear clocks to surpass existing bounds set by other experiments and motivates future experimental designs, including space-based missions involving clocks.

Finally, Chapter 6 summarises the key results presented in this thesis. The Appendices at the end provide supporting information and plots relating to the work presented in Chapter 5.

This thesis sits at the intersection of cold-atom-based quantum sensing and fundamental physics, contributing to a wider effort in the field to explore open questions in cosmology and particle physics using new, interdisciplinary approaches. By developing both experimental systems as part of the AION project and analysis tools, it contributes to laying the groundwork for future precision experiments that can not only test physics beyond the Standard Model but also drive technological advances with wider societal impact.

Chapter 2

The Atom Interferometry Observatory and Network

Light-pulse atom interferometry (AI) has been a rapidly evolving field originating in the 1990s [45, 46]. Atom interferometry is a technique that uses the wave-like nature of atoms to create interference patterns, allowing precise measurements of acceleration, rotation, gravity, and fundamental constants. By splitting and recombining atomic wave packets using laser pulses, atom interferometers can detect phase shifts caused by external forces acting on the atoms. Since its conception, atom interferometry has been used in inertial sensing [47] by measuring gravitational acceleration [48, 49], gravity gradients [50, 51], Earth rotations [52, 53] and for fundamental physics research [54].

Atom interferometers have been used to test fundamental constants such as Newton's gravitational constant G [55] and the fine structure constant α [56, 57]. They have also been used to test general relativity by testing the universality of free fall caused by Einstein's equivalence principle [58]. They can also test different particle physics models

by searching for dark energy (DE) [59, 60], other unknown forces, and dark matter. AIs can also be used to detect gravitational waves (GWs) by probing very minute space-time distortions caused by the passage of these GWs through the AI detector [25, 61, 62]. The detection of DM and GWs by atom interferometers is discussed in more detail in Section 2.1.5.

In this chapter I introduce the basic principles behind how atom interferometers work and present the Atom Interferometry and Observatory Network (AION) project. I will describe the different parts of the detector and its sensitivity to Ultra-Light Dark Matter (ULDM) and mid-frequency gravitational waves.

In the following sections, I introduce the AION project in more detail including the detector design (Section 2.1) and its science case (Section 2.1.6). An overview of how single-photon clock transition atom interferometry works is also presented (Section 2.1.3). Lastly, I provide an overview of efforts worldwide to construct long baseline atom interferometers for performing fundamental physics experiments.

2.1 The AION Detector

The Atom Interferometer Observatory and Network (AION) project [54] aims to use cold strontium atoms and atom interferometry to search for ultra-light dark matter and for gravitational waves (GWs) in the mid-frequency band ($\sim$ 0.01 Hz to a few Hz). Possible sources of these GWs include intermediate-mass black holes to which current and planned experiments including LISA [30], LIGO [26] and Virgo [27] are not sensitive. The NANOGrav collaboration has recently discovered evidence for low-frequency gravitational waves originating from supermassive black hole binaries providing further motivation for exploring different frequency bands [63].

This staged project is to begin with a 10 m baseline atom interferometer which will pave the way to a 100 m detector and eventually a km-scale terrestrial detector. The final stage is the development of a satellite-based detector similar to the proposed AEDGE mission [64]. The project is currently in Stage 1, with the construction of the 10 m detector planned in Oxford. AION has a similar experimental concept to the MAGIS experiment [65, 66], based in the US - the two projects collaborate closely and in later stages will operate in a networked configuration.

The AION detector will operate using single-photon strontium atom interferometry [5]. The project is motivated by the potential of differential atom interferometry, where multiple spatially separated interferometers are addressed by a common laser source. This configuration enables the rejection of common-mode noise, such as laser phase noise, thereby enhancing sensitivity to signals and enabling new capabilities in gravitational wave detection and fundamental physics.

In the 10 m detector, a common laser source will be used to operate two atom interferometers simultaneously. In subsequent stages, several atom interferometers will be used, all addressed by a common laser source, and large momentum transfer techniques will be used [67]. A differential phase measurement between the interferometers will be taken at the end of the interferometric sequence [68]. To permit long flight times, sub-microkelvin temperatures are required for the atomic cloud before launch, as well as the mitigation of systematic effects [61].

A simplified schematic diagram of the detector, with two atom interferometers in vertical configuration, is shown in Figure 2.1. The steps followed are (1) preparing the ultracold atoms in the atom source compartment, (2) launching the atoms into the baseline of the detector and let them free-fall, (3) the interferometric sequence takes place, and (4) phase

measurement of the atoms after the interferometric sequence. The experimental concept will be described in more detail in subsequent subsections.

In this setup, the clock laser is delivered from one end of the baseline and retroreflected from a steerable mirror, ensuring that the interferometer pulses are derived from a common optical wavefront. This geometry is essential in large-baseline atom interferometry setups, as it ensures that common laser phase noise cancels between different interferometers. Steering the retro-mirror allows controlled introduction of a spatial phase shear across the atom cloud, enabling single-shot phase readout where spatial fringes are generated to facilitate imaging-based phase measurement. This is referred to as the phase-shear readout technique [69]. It allows determination of both the phase and contrast of atom interferometers in a single experimental shot, eliminating the need for multiple measurements with different phases.

2.1.1 Preparing the atom sources

The AION project requires sufficient and efficient cooling of strontium atoms to ultracold temperatures to implement high-precision atom interferometry over long baselines [61]. Cold atom clouds are essential for atom interferometry experiments as they enable high precision measurements by reducing the thermal motion of atoms and ensuring that as many atoms as possible go through the desired trajectory in the interferometer sequence and contribute to the signal. Many systematic errors relating to the cloud's position and velocity are also mitigated by cooling the atoms due to preparing the atoms with well-defined initial conditions. Cooling the atoms narrows their velocity distribution, which allows for longer coherence times, resulting in maintaining the visibility of the interference fringes at the end of the interferometric sequence. It also allows for longer interrogation and flight times, which in turn increases the sensitivity of the interferometer.

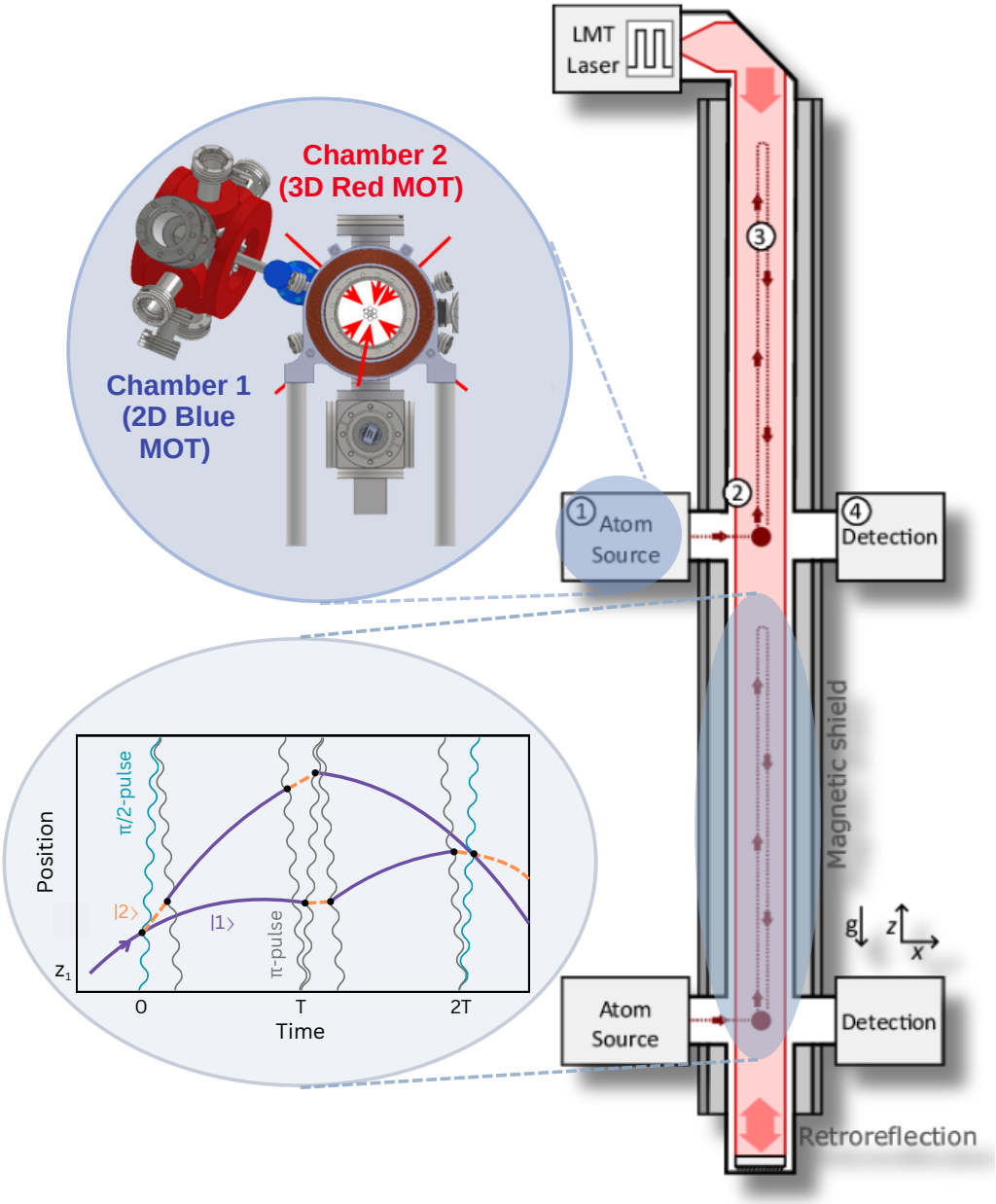

Figure 2.1: Conceptual design of the AION detector [54, 2]. Ultra-cold strontium atoms are cooled down in the atom source sections and prepared in an optical trap, transported into a magnetically-shielded baseline, and then launched and allowed to free-fall in the tube where atom interferometry takes place. A sequence of pulses will split and recombine the two atomic paths. Using the phase-shear readout technique [69], a differential phase measurement reveals information about the interaction of the atoms at the end of the interferometric sequence.

Cold atoms also experience reduced Doppler broadening of the clock transition used for interferometry, improving the efficiency of laser-atom interactions and enhancing overall interferometer performance.

A high atomic flux is required to maximise the signal-to-noise ratio and measurement rate of the interferometers, while low atomic temperatures are necessary to preserve coherence and enable high-contrast interference fringes. The source must therefore efficiently produce large numbers of ultracold atoms to optimise the overall sensitivity of the differential atom interferometry. To reach the required temperature, a sequence of cooling techniques is used before the atoms are launched into the main baseline of the detector where they undergo interferometry. This includes a 2D "blue" Magneto-Optical Trap (MOT), a 3D "blue" MOT, a 3D "red" MOT and an optical dipole trap for evaporative cooling [70, 71]. The atoms are then optically transported to the interferometry region where they are launched and interferometry takes place. The set of Ultra-High Vacuum (UHV) chambers where the atoms are loaded, cooled, and state prepared, or so-called sidearms, are attached to the side of the vertical detector next to the interferometer tube as shown in Figure 2.1. More details on the sidearm design and production are presented in Ref. [[1]].

2.1.2 The Strontium Atom

The AION project uses strontium, an alkaline-earth atom, due to its narrow-linewidth $^1S_0 - {}^3P_0$ clock transition at 698 nm used for interferometry [72, 67, 73] and convenient optical transitions which allow for efficient trapping in MOTs [74, 75, 76, 77, 78, 79, 80, 81]. For the first stage of cooling, the 2D and the 3D “blue” MOT, the strong, dipole-allowed $^1S_0 - {}^1P_1$ transition at 461 nm is used. This transition has a natural linewidth of 32 MHz. The subsequent cooling stage, the “red MOT”, operates on the intercombination transition $^1S_0 - {}^3P_1$ at 689 nm. This is a narrow transition (γ = 7.6 kHz) and can be

used to reduce the temperature of the atomic sample down to half the photon recoil limit temperature of 230 nK [74, 82]. The AION project requires the ^{87}Sr isotope since its nuclear spin permits driving the 698 nm clock transition through mixing of states via the hyperfine interaction. A simplified schematic diagram of the strontium levels and transitions is shown in Figure 2.2.

Strontium is an alkaline earth metal (Group 2 on the periodic table), appearing as a metal at room temperature. It has a low vapor pressure and strontium atoms are reactive with oxygen, nitrogen, water and silicates but it is inert against sapphire. In terms of its electronic level structure, strontium has two valence electrons. The electron pairing gives rise to various electronic states which can be grouped into spin singlet (S=0) or spin triplet (S=1) states depending on the orientation of the spin of the two electrons which can be anti-parallel for S=0 and parallel for S=1.

Four natural isotopes of strontium exist (^{88}Sr, ^{87}Sr, ^{86}Sr and ^{84}Sr), three of which are bosonic and one (^{87}Sr) is fermionic. ^{88}Sr has the highest natural abundance (82.56 %) followed by ^{87}Sr (7.02%) [83]. These two isotopes are of the most interest to this work.

The ground state of strontium is $^1S_0$ and there is a strongly allowed dipole transition between the ground and $^1P_1$ states. The first metastable excited state of strontium is the triplet state ^3P. The dipole selection rule, i.e. $\Delta S = 0$, forbids dipole transitions between the spin singlet and triplet states. However, the spin symmetry is broken by the spin-orbit interaction among excited states, allowing for inter-combination weak dipole transitions between singlet and triplet states [77].

In the case of Strontium, spin-orbit coupling introduces mixing between $^3P_1$ and $^1P_1$ states, the latter of which has a dipole-allowed transition to the ground state ($^1S_0$). As a result the $^1S_0 \rightarrow ^3P_1$ transition, which would otherwise be forbidden becomes weakly

allowed due to the state mixing [84, 85]. This results in a weakly allowed ${}^1S_0 \rightarrow {}^3P_1$ dipole transition.

The bosonic isotope ^{88}Sr has a nuclear spin of zero (I = 0) [77]. ^{88}Sr has been very widely used due to its natural abundance. Its zero nuclear spin makes it easier for it to be captured and cooled as the complications arising from hyperfine structure are not present. $J = 0 \rightarrow J = 0$ transitions are not allowed due to selection rules, which means the ${}^1S_0 \leftrightarrow {}^3P_0$ clock transition in ^{88}Sr is forbidden. This makes the natural linewidth of this transition very narrow but it also means it is not possible to excite this transition with a single photon.

The odd isotope ^{87}Sr has a nuclear spin of I = 9/2. As a result of this nuclear spin, the ^{3}P states are perturbed by the hyperfine interaction. ^{3}P$_0$ like ^{3}P$_1$ obtains a weak dipole coupling to ^{1}S$_0$ as ^{3}P$_0$ gets mixed with the ^{1}P$_1$ and ^{3}P$_1$ states due to the hyperfine interaction. This allows a single photon ${}^3P_0 \rightarrow {}^1S_0$ decay at a rate of $\Gamma/2\pi$ = 1 mHz [86]. This allows the transition to be excited within a reasonable timeframe, while still maintaining a narrow linewidth that can be well-resolved. The non-zero nuclear spin of ^{87}Sr results in a complex Zeeman structure, which complicates cooling and adds additional requirements in the process.

Using Strontium for AION

Strontium has convenient transitions for laser cooling, trapping and atom interferometry, which is why it is used for the AION detector. Strontium has two near-cycling transitions at 461 nm and 689 nm which allow for efficient and successive stages of laser cooling. The ^{1}S$_0$-^{1}P$_1$ transition is a strong one with a broad linewidth (32 MHz). This transition allows for Sr to be cooled down to a Doppler limit of 770 µK [88]. Subsequent cooling is achieved using the narrow-line ^{1}S$_0$–^{3}P$_1$ transition at 689 nm, which has a linewidth in the

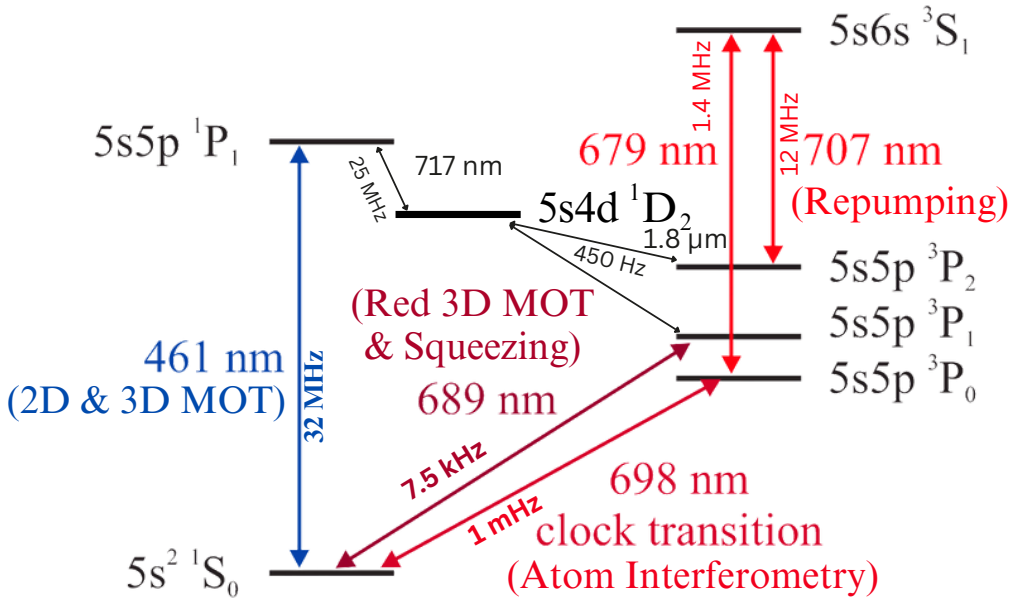

Figure 2.2: Simplified schematic diagram of the strontium levels used in cooling, trapping, and interferometry [76]. The linewidths ($\Delta\nu = \Gamma/2\pi$, where Γ is the decay rate) of the transitions are also indicated. While the 5s5p $^3P_0$ has a 1 mHz linewidth for ^{87}Sr, in the other isotopes this transition is effectively forbidden [87]. The hyperfine structure of ^{87}Sr is not shown in this diagram.

kilohertz range and supports cooling to sub-microkelvin temperatures, reaching a Doppler limit as low as 0.18 μK.

In addition to its favourable cooling transitions, strontium features an ultra-narrow clock transition at 698 nm between the $^1S_0$ ground state and the $^3P_0$ state. This transition is an extremely weakly allowed electric dipole transition, highly suppressing spontaneous emission due to its ultra-narrow linewidth (just a few millihertz), ensuring long coherence times, which are essential for precision atom interferometry. Since both the ground state and the $^3P_0$ have J = 0, they are less sensitive to first-order Zeeman shifts and are less sensitive to electric fields, reducing Stark shift perturbations. The transition is therefore very stable and robust against external magnetic and electric fields, which can cause perturbations. Additionally, auxiliary transitions at 678 nm and 707 nm allow for effective

repumping of atoms during the cooling process, improving experimental efficiency.

2.1.3 Clock Atom Interferometry

Once the atoms are cooled to a low enough temperature, they are launched into the baseline (middle part of the detector) where the interferometry sequence begins. This section provides an overview of atom interferometry and is based on References [89, 90, 91, 92, 93]

Atom interferometry exploits the wave-like nature of matter (atoms) to produce interference and make highly accurate measurements. The way atom interferometers work is analogous to the way light interferometers work but the role of matter and light are reversed. Whereas in light interferometers the source emits light that is brought into interference using mirrors and beamsplitters, in atom interferometers, the source emits atoms (matter waves) and lasers act as mirrors and beamsplitters. This is illustrated in Figure 2.3, which shows the basic operation of Mach-Zehnder-type interferometers. In a light interferometer, the light is split by beamsplitters and the two beams follow two different paths until they both hit a mirror which brings the two beams back together where they recombine and they interfere, and the interference patterns can be observed at the end of the interferometric sequence. By measuring the overall phase of the interferometer, encoded in the populations of the two output ports, the optical path length difference can be inferred.

Similarly, in atom interferometry you can split the wavefunction of the atom into a superposition of two states (ground $|g\rangle$ and excited $|e\rangle$ state), which are spatially separated due to the photon recoil which imparts momentum kicks and cause the wavepackets to physically separate and evolve in two different paths. The two states are separated by

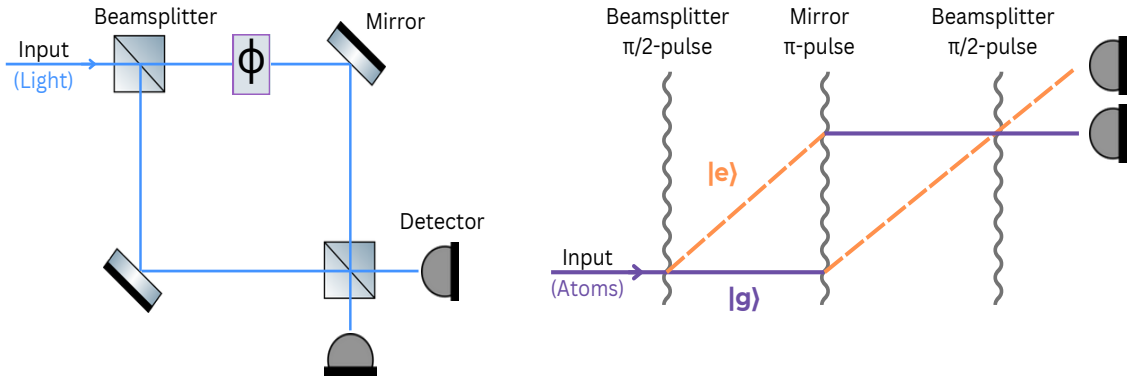

Figure 2.3: Comparison of a conventional Mach-Zehnder light interferometer (left) and a light-pulse atom interferometer (right), where laser pulses (wavy lines) act as beam splitters and mirrors for atomic matter waves.

an energy ω_A. An atom interferometer measures the phase difference between spatially delocalised, coherent superpositions of atomic clouds.

Transitions between these states, as well as the degree of superposition and spatial separation of the wavepackets, are controlled via laser pulses. At the end of the sequence, instead of getting light fringes, you get atom fringes which reveal the phase difference, $\Delta\phi$ between the two different arms (paths) of the interferometer. The phase difference can be extracted by measuring the population difference between the excited and ground states. The phase difference is calculated as

$$C\cos\Delta\phi = \frac{N_e - N_g}{N_g + N_e} \tag{2.1}$$

where N_g/N_e is the number of atoms in the ground/excited state at the end of the interferometric sequence, and C is the contrast, which denotes the oscillation amplitude. The number of atoms in the excited and ground states is measured by detectors at the end of the sequence, and the phase difference can be calculated using the equation above as long as the value for the contrast is known.

The total phase difference $\Delta\phi$, derives from two primary contributions: the quantum state evolution during free-fall motion along each interferometric path, and the local laser phase that is transferred to the atom at each atom-light interaction point.

Because the interferometer configuration effectively compares atomic motion against the reference frame established by the laser pulse sequence, $\Delta\phi$ exhibits high sensitivity to inertial forces experienced by the atom throughout the interferometric sequence. This sensitivity enables the use of atom interferometers as precision accelerometers [39]. Furthermore, given that the interferometer involves trajectories where atoms transition between ground and excited states, $\Delta\phi$ also demonstrates strong sensitivity to the fundamental constants governing these atomic transitions. This characteristic allows atom interferometers to function as high-precision atomic clocks [38].

Clock Atom interferometry - The Pulse Sequence

We will now take a closer look at how atom interferometry works, considering a single atom interferometer. A single run, termed an interferometric cycle or sequence, comprises three stages: preparation of the atomic cloud, application of the interferometer pulse sequence, and detection of the final atomic state. In this section, I focus on and explain in more detail the interferometer pulse sequence.

In a light-pulse atom interferometer, a sequence of laser pulses acts as effective beam splitters and mirrors for the atomic wave packets, coherently manipulating their states. The laser pulses couple atomic momentum states through stimulated processes (such as two-photon Bragg or Raman transitions, or single-photon clock transition in the case of strontium), imparting photon recoil momentum to the atoms while driving coherent superpositions of momentum states. In single photon transitions (where $|\mathbf{k}| \approx \Delta\omega$) as a result of momentum conservation, an atom initially in the ground state with momentum $\mathbf{p}$

(i.e. $|g, \mathbf{p}\rangle$) will be excited and acquire a momentum kick $\mathbf{k}$, resulting in the state $|e, \mathbf{p}+\mathbf{k}\rangle$. The atom undergoes Raman oscillations between the corresponding initial and final states during the light-atom interaction.

This process splits and redirects the atomic wave packets along spatially separated paths, which later recombine to form an interference pattern. The phase difference accumulated between the interferometer arms depends on inertial effects and external fields experienced by the atoms. At the end of the interferometric sequence, the relative populations in different output ports are measured to infer this phase shift. The sequence of events, from launching the atoms in the detector baseline to detecting the output populations, is illustrated in Figure 2.4.

The atoms are prepared in the ground state and launched vertically upwards, allowing them to freely fall in the interferometer vacuum tube. A series of pulses of different durations is then applied. AION uses a Mach-Zehnder-type interferometer sequence whose most simple form consists of a $\pi/2 - \pi - \pi/2$ or a beamsplitter-mirror-beamsplitter sequence. The type of pulse is determined by the duration and intensity with which the resonant radiation (laser) interacts with the atom and is defined by the Rabi frequency Ω. In this scheme, a beamsplitter corresponds to a $\pi/2$ pulse (one quarter of a Rabi period), which creates a coherent superposition of internal states, while a mirror pulse corresponds to a π pulse (half a Rabi period), which exchanges the population between the two states. Both types of pulses impart a change in momentum state $\mathbf{k}$.

To see this in practice for the interferometric sequence let's take a closer look at Figure 2.4. Panel (A) shows the atoms (in the ground state ($|g\rangle$) - indicated by a solid purple line) being launched vertically upwards. At time T = 0, a $\pi/2$ pulse interacts with the atoms, and excites approximately half of them while also imparting a momentum kick in

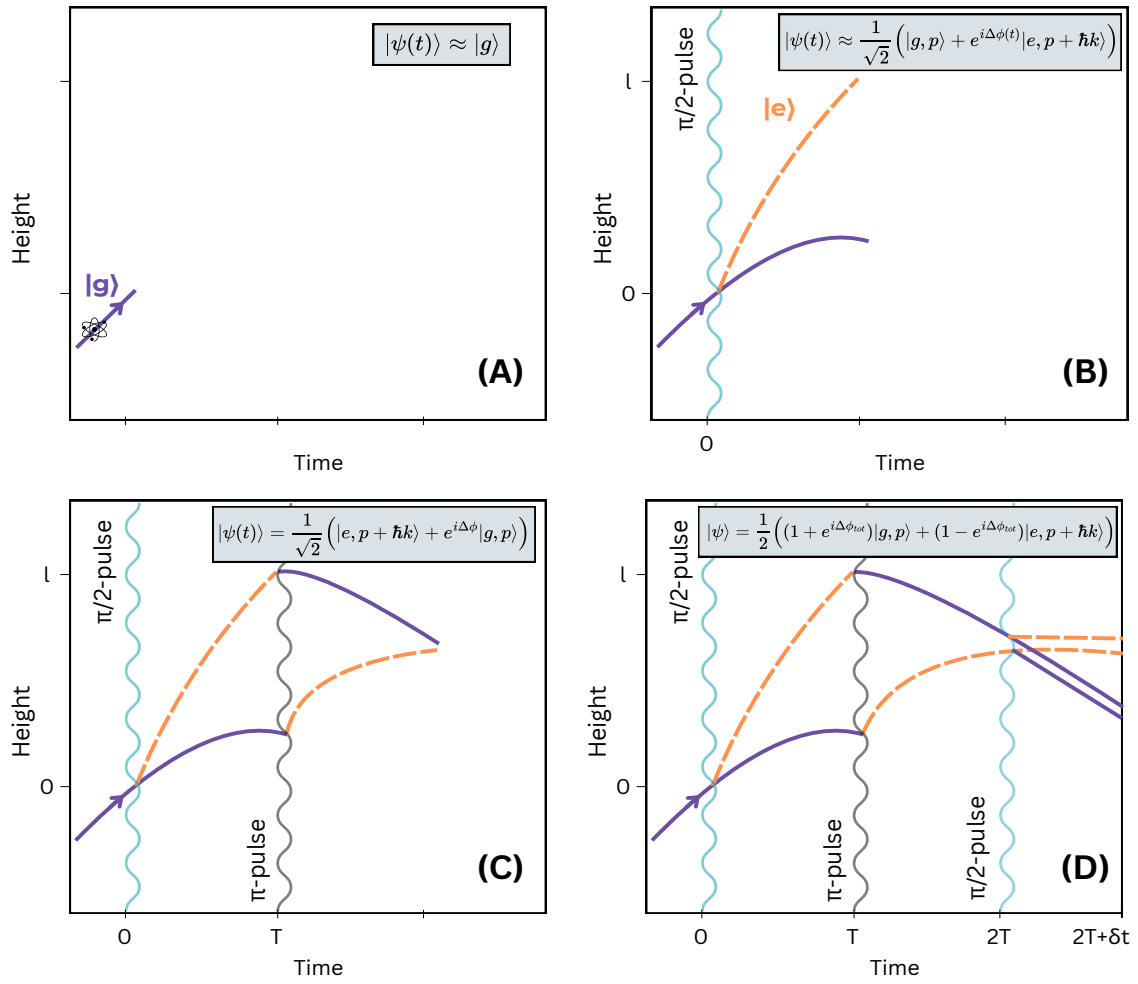

Figure 2.4: Spacetime diagram for a Mach-Zehnder interferometer sequence. The evolution of the atom's ground and excited state is shown in steps starting from the launch of the atom in the ground state (panel A); and continuing with the propagation of the atomic states after the interaction with a $\pi/2$ pulse (beamsplitter) at t = 0 (panel B); a mirror pulse at t = T (panel C) and another beamsplitter at t = 2T (panel D). After the application of the final beamsplitter, a drift time δt is allowed to pass before imaging the atoms. The total phase acquired and measured at the end of the interferometric sequence is denoted as $\Delta\phi_{tot}$. Adapted from: [94]

the excited state atoms spatially separating these atoms from the ground state ones. This creates a superposition of the two states as shown by the wavefunction on the top right of panel (B). A relative phase shift is also acquired. In panel (C), we can see a π pulse being applied at time T which acts as a mirror. This pulse causes the states of the atoms in

the two paths to swap and a momentum kick to be applied to the new excited state path, causing the two paths to recombine.

Panel (D) shows the application of another $\pi/2$ pulse at t = 2T to the two arms of the interferometer, which splits each of them into a further superposition of the ground and excited states. Some time is allowed to pass for the four atomic wavepackets to spatially separate before the measurement of the interference takes place, determining the number of atoms in the excited and ground states to infer the phase shift accumulated at the end of the interferometric sequence. The measurement happens at the "detection" part of the AION detector as shown in Figure 2.1.

Phase Shift Determination for a Single Interferometer

In this section an overview of the formulae defining the calculation of the phase difference between the two arms of the interferometer is provided which is based on Ref. [89], where the full derivation of these formulae can be found.

The total phase difference ($\Delta\phi_{tot}$) between the two arms of an interferometer can be written as a sum of three different components, namely the propagation, separation, and laser phase, written as:

$$\Delta\phi_{\text{tot}} = \Delta\phi_{\text{propagation}} + \Delta\phi_{\text{separation}} + \Delta\phi_{\text{laser}}. \tag{2.2}$$

For the equations below, we take that $\hbar = c = 1$.

The propagation phase $\Delta\phi_{\text{propagation}}$ results from the atom's free-fall evolution between light pulses and is expressed as:

$$\Delta\phi_{\text{propagation}} = \sum_{\text{upper}} \left(\int_{t_I}^{t_F} (L_c - E_i)\, dt \right) - \sum_{\text{lower}} \left(\int_{t_I}^{t_F} (L_c - E_i)\, dt \right) \tag{2.3}$$

In this equation, the summations account for all path segments in the upper and lower arms of the interferometer. Here, L_c represents the classical Lagrangian evaluated along the classical trajectory for each segment. Also, the equation accounts for contributions from the internal atomic energy level E_i. There is one term for each path segment (upper and lower) with the corresponding initial time, final time, L_c and E_i for each path.

The laser phase $\Delta\phi_{\text{laser}}$ accounts for the phase change caused by the atom interacting with the laser field used as a mirror/beamsplitter in the interferometric sequence to manipulate the wavefunction. Every time the laser interacts with the atoms, the phase of the laser ($\phi_L(t_0, \mathbf{x}_c(t_0)) = \mathbf{k} \cdot \mathbf{x}_c(t_0) - \omega t_0 + \phi$) is imprinted on the component of the state that changes momentum due to the atom-light interaction. The laser phase is defined as:

$$\Delta\phi_{\text{laser}} = \left(\sum_j \pm\phi_L(t_j, \mathbf{x}_u(t_j)) \right)_{\text{upper}} - \left(\sum_j \pm\phi_L(t_j, \mathbf{x}_l(t_j)) \right)_{\text{lower}} \tag{2.4}$$

The summations include all the interaction points occurring at times t_j, with $\mathbf{x}_u(t)$ and $\mathbf{x}_l(t)$ representing the classical trajectories of the upper and lower arms of the interferometer, respectively. The sign of each term is determined by whether the atom gains $(+)$ or loses $(-)$ momentum during the interaction.

The classical paths of two arms of the interferometer do not perfectly intersect when the last $\pi/2$ pulse is applied (at the final beamsplitter) giving rise to the separation phase $\Delta\phi_{\text{separation}}$. The resulting separation phase shift is defined as:

$$\Delta\phi_{\text{separation}} = \bar{\mathbf{p}} \cdot \Delta\mathbf{x} \tag{2.5}$$

for a separation of $\Delta\mathbf{x} = \mathbf{x}_l - \mathbf{x}_u$, where $\bar{\mathbf{p}}$ is the average classical canonical momentum of the atom after the final $\pi/2$ pulse is applied.

Sensitivity

Two types of sensitivity determine the total sensitivity of an atom interferometer to phase shift measurements; the readout sensitivity and the intrinsic sensitivity. The readout or shot-noise limited sensitivity is determined by how accurately the final phase measurement of the interferometer can be measured. This measurement is limited by the quantum shot noise, which scales as $\frac{1}{\sqrt{N}}$ [95], where N is the number of atoms that undergo the interferometric sequence unless spin squeezing is used to reduce quantum noise below the standard quantum limit (SQL). By increasing the number of atoms involved in the measurement, the precision of the measurement also increases. The intrinsic sensitivity depends on the strength of the effect under study and how much the magnitude of the resulting phase shift of the interferometers is affected by it. The sensitivity of the detector to the physics under consideration needs to be maximized by maximizing the phase shift created in the interferometer. The following section describes the methods used in AION to maximize this phase shift.

2.1.4 Differential Atom Interferometry and LMT

The AION project's experimental concept is based on a differential phase measurement which is achieved by using two or more atom interferometers in the same detector which are all addressed by a common laser source. The interferometers are operated as a single

photon atom gradiometer [25].

Figure 2.5 illustrates the principle of operation of two AIs which are separated vertically by a distance Δz in a baseline of length L. The interferometers are positioned at distances z_1 and z_2. The advantage of using more than one interferometer is that a single laser beam can be used to interrogate both interferometers simultaneously resulting in a differential phase measurement that can highly suppress laser phase noise [96], a scheme made possible by the use of strontium and its single-photon clock transition [54, 72, 97]. The phase difference measured for a gradiometer (combination of two atom interferometers) is therefore the difference of the total phase of the individual single-photon atom interferometers. This is a differential phase measurement.

Large momentum transfer (LMT) techniques [25, 67] will also be used to enhance the intrinsic sensitivity at the end of the interferometer. A series of π-pulses can be applied in opposite directions after the initial beam splitter to increase the separation between the atom interferometer arms. For n number of additional π pulses, the atoms acquire an increase in momentum of $n\hbar k$, where $k = \omega_A/c$. This principle is illustrated in Figure 2.5.

2.1.5 Ultra-light Dark Matter and Gravitational Wave Detection in Atom Interferometers

Given the overview of how differential atom interferometry operates, this section presents how scalar ULDM and gravitational waves can imprint a signal which can be observed using this technique. The main limitation of such a measurement, which defines the sensitivity of the detector to such signals, is the atom shot noise e.g. $\delta\phi \sim 1/\sqrt{N}$, where N is the number of atoms.

An atom interferometer can act as a precision accelerometer or gravitational wave sensor

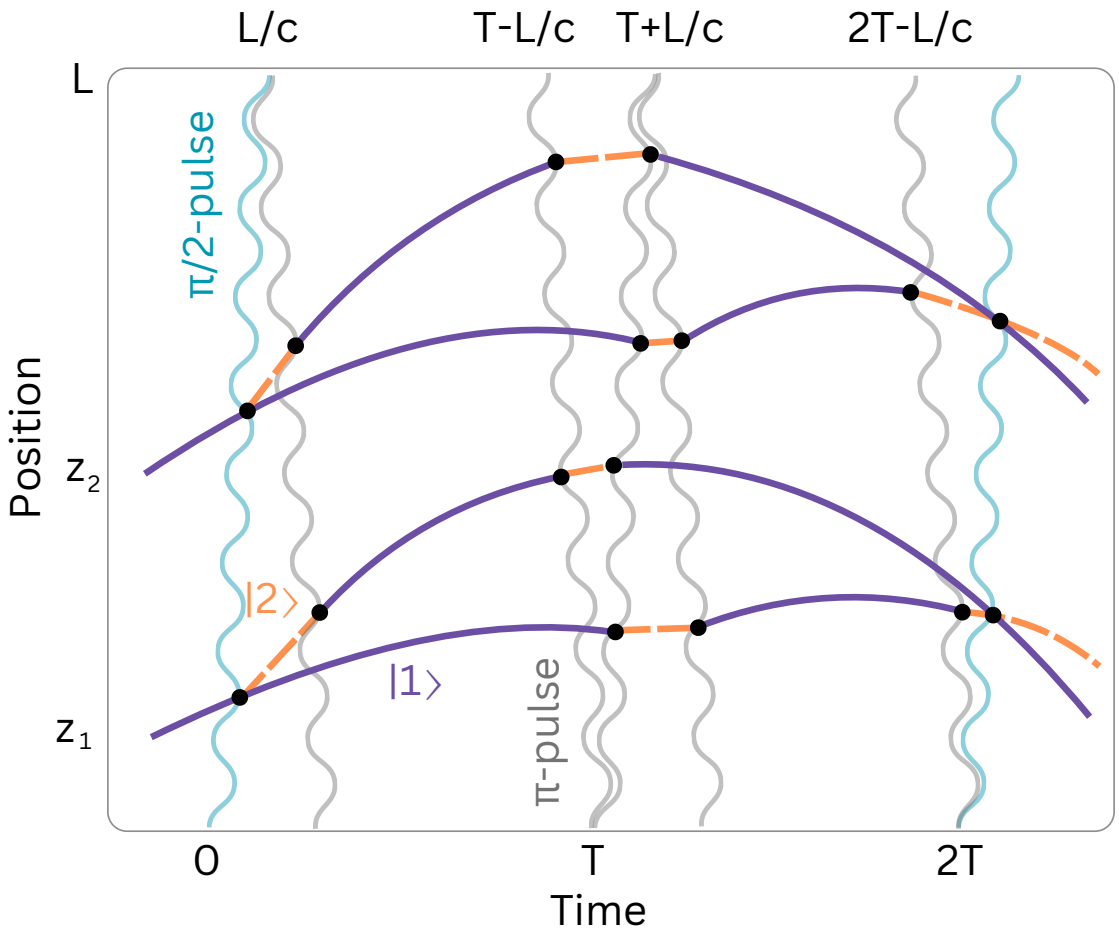

Figure 2.5: Space-time diagram of the principle of operation of a single-photon differential atom interferometer with the long momentum transfer technique applied. The vertical distance of the baseline is shown on the y-axis. There are two atom interferometers in vertical configuration with a distance $\Delta z = z_2 - z_1$ between them. The propagation of the ground (purple solid lines) and excited state (yellow dashed lines) is shown. The black circles show the atom-light interactions. The first and last light pulses act as beamsplitters ($\pi/2$ pulses), and the pulses in between are multiple π pulses that reverse the state of the atoms and impart momentum kicks to the atoms. Here the order of the LMT sequence n = 2.

by using the differences in the time each arm of the atomic wavefunction spends in the excited state. When the atom experiences acceleration, the two interferometer paths do not remain symmetric, resulting in unequal excited-state durations and a phase difference. This phase is imprinted during the short-duration laser pulse interactions, rather than ac-

cumulated during the free evolution time between them. However, the total phase shift still scales linearly with the interrogation time T, as the effect of acceleration on the light travel time across the interferometer baseline accumulates over this interval. The sensitivity is also enhanced by increasing the number of photon momentum kicks n, since a larger n leads to a longer path in the excited state. To leading order, the phase shift due to a static gravitational field scales as $\phi \sim n\omega_a g T^2/c$ [25], where ω_a is the energy splitting between internal states, g is the local gravitational acceleration, and c is the speed of light.

The phase shift in a differential atom interferometer with a baseline L arises from the phase difference ($\Delta\phi_{diff}$) accumulated at the output of the two atom interferometers. Figure 2.6 visually illustrates the effect of ultralight dark matter and gravitational waves on the differential atom interferometer.

When a gravitational wave of strain amplitude h and frequency ω passes through the system, it induces a strain h that modulates the effective separation L between the two interferometers such that the arrival time of the laser beam is changed (i.e. $\Delta T = hL$). This modulation leads to a time-dependent variation in the differential phase shift [25]. The gravitational wave changes the spacetime metric, effectively altering the light travel time between the interferometers and introducing a measurable phase difference.

To detect gravitational waves using atom interferometry, we consider the effect of a passing plane gravitational wave propagating in the x-direction. In the transverse-traceless (TT) gauge, the spacetime metric is given by [25]:

$$ds^2 = c^2dt^2 - (1 + h\sin(\omega(t-z) + \phi_0))\,dz^2 - (1 - h\sin(\omega(t-z) + \phi_0))\,dy^2 - dx^2, \tag{2.6}$$

where h is the strain amplitude of the gravitational wave, ω its angular frequency, and ϕ_0

the gravitational wave's phase at the start of the AI pulse sequence.

For an AI based on a single-photon transition, the leading-order phase shift accumulated in the interferometer at position z_1 is

$$\Delta\phi(z_1) = 4\frac{h\omega_A}{\omega}\sin^2\left(\frac{\omega T}{2}\right)\sin\left(\frac{\omega z_1}{2c}\right)\sin\left(\omega T + \frac{\omega z_1}{2c} + \phi_0\right), \tag{2.7}$$

where ω_A is the atomic transition frequency and $2T$ is the interrogation time. A detailed derivation of this is presented in Ref. [98].

With two atom interferometers located at z_1 and z_2, the differential phase shift induced by the gravitational wave is

$$\Delta\phi_{\text{diff}} = 4\frac{h\omega_A}{\omega}\sin^2\left(\frac{\omega T}{2}\right)\sin\left(\frac{\omega(z_2-z_1)}{2c}\right)\sin\left(\omega T + \frac{\omega(z_1+z_2)}{2c} + \phi_0\right). \tag{2.8}$$

In the limit where $\omega L/c \ll 1$ and $L = z_2 - z_1$, this simplifies to [54]

$$\Delta\phi_{\text{diff}} \approx 2hkL\sin^2\left(\frac{\omega T}{2}\right)\sin\left(\omega T + \phi_0\right), \tag{2.9}$$

with $k \approx \omega_A/c$ being the wave number of the interrogation laser. This expression highlights how the differential phase shift depends on the gravitational-wave strain h, the baseline length L, the interrogation time T, and the atomic transition frequency ω_A.

ULDM can give rise to a differential phase shift by inducing time-dependent variations in the atomic transition frequencies [23, 24, 99]. The ultra-light wave-like scalar dark matter field can be depicted as a classical field that oscillates in space and time. If ULDM couples to standard model particles such as electrons or photons, it induces periodic vari-

ations in fundamental constants, specifically, the electron mass and the electromagnetic fine-structure constant. As the dark matter field evolves, this induces a sinusoidal oscillating time-dependent perturbation in the atomic transition frequency. Because the laser reaches each atom interferometer at slightly different times due to the finite speed of light, any time-dependent perturbation from dark matter will manifest as fluctuations in the differential phase accumulated between the two interferometers.

A differential atom interferometer will detect a significant phase shift when the oscillation period of the dark matter wave is equal to the duration of the interferometric sequence. Since all other phase shifts are cancelled out due to the differential configuration, even small phase shift caused by very small signals can be detected, making differential interferometers very sensitive to minute dark matter effects. The phase shift caused by ULDM would scale as $\Delta\omega T$.

2.1.6 The AION Science Case

AION Sensitivity

The resulting phase depends on both the distance between the two interferometers and the time the atoms spend in free-fall (controlled by the number of LMT/π-pulses applied). Therefore, it is essential to have long baseline interferometers to achieve sensitivities that allow for the detection of these phenomena.

For this reason, the AION program is comprised of several stages each with increasing baseline distance and therefore sensitivity. The different sensitivity scenarios are summarised in Table 2.1, where a list of basic parameters is given for each. The plan is to have three different length baseline detectors each one building on the previous one. The initial AION-10-m detector will serve as a proof-of-concept detector and a starting point

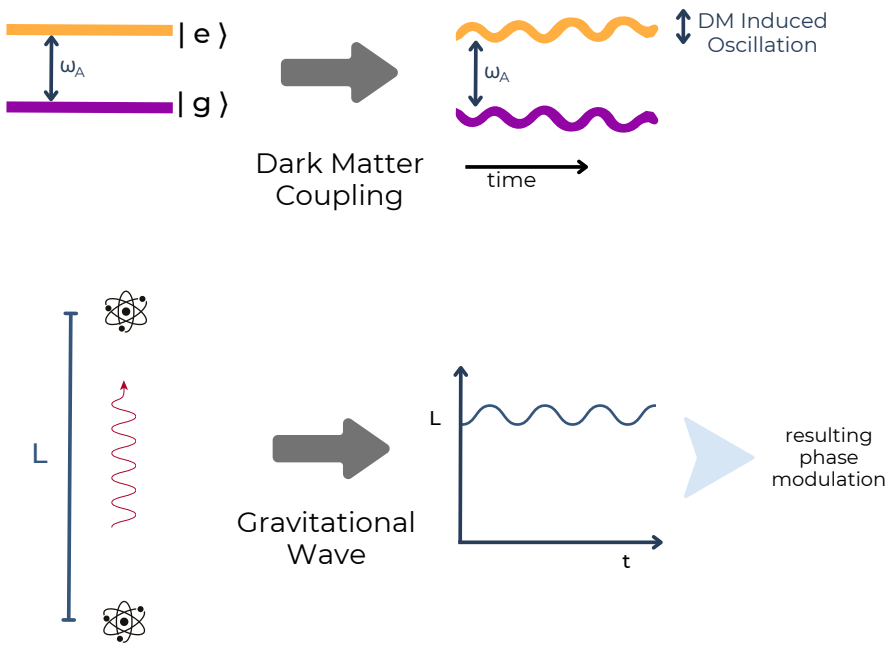

Figure 2.6: Effects of ultralight dark matter and gravitational waves on a differential atom interferometer. (Top) Ultra-light scalar dark matter couples to the atom and causes oscillations in fundamental constants e.g. the electron mass. This in turn induces periodic variations in the atom transition frequency of the atom. These variations are imprinted into the phase accumulated in the interferometers and therefore the differential phase measurement. (Bottom) Gravitational waves cause changes in spacetime as they pass through the detector. The distance between atom interferometers changes, and the change depends on the strain h of the gravitational wave. This also manifests as a differential phase shift in the interference pattern.

for AION-100. Once the 10-m detector reaches the ultimate sensitivity possible, the plan is to build a 100-m detector which will have an improved sensitivity. AION-100 will pave the way for the AION-km which will be a terrestrial-based detector. The ultimate sensitivity is projected to be achieved with a space-based detector, using a two-satellite configuration such as the proposed AEDGE mission [64].

Mid-Frequency Gravitational Waves

AION would be most sensitive to mid-frequency gravitational waves, as shown in Figure 2.6. The range of frequencies covered by AION would allow observations of mergers

Sensitivity Scenario	L [m]	T [sec]	$\delta\phi_{\text{noise}}$ [1/$\sqrt{\text{Hz}}$]	LMT [number n]
AION-10 (initial)	10	1.4	10^{-3}	100
AION-10 (goal)	10	1.4	10^{-4}	1000
AION-100 (initial)	100	1.4	10^{-4}	1000
AION-100 (goal)	100	1.4	10^{-5}	40000
AION-km	2000	5.0	0.3×10^{-5}	40000

Table 2.1: Basic parameters for different stages of the AION project including the length of the detector L; interrogation time of the atom interferometer $2T$; phase noise $\delta\phi_{\text{noise}}$; and number n of large momentum transfers (LMT). From: [54].

from intermediate-mass black holes [100] and it compliments the measurements from the LISA, LIGO, Virgo, KAGRA, INDIGO, ET and CE experiments.

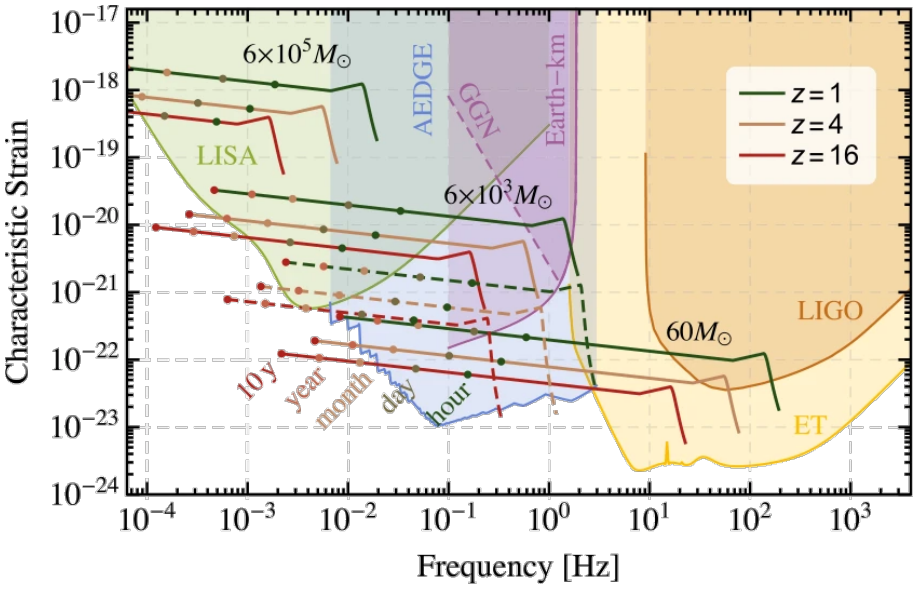

Figure 2.7: Comparison of strain sensitivities between AION and other experiments for different total mass black hole mergers at different redshifts (z). The time left before a merger is also indicated. Equal mass binaries are indicated with solid lines whereas unequal mass binaries are indicated with dashed lines. Potential gravitational gradient noise (GGN) levels for the km-scale ground-based detector is also depicted. From: [64].

Ultra-Light Dark Matter

AION can potentially detect ultra-light scalar DM through its couplings to electrons, photons and the Higgs field [101, 102]. These couplings cause oscillations in the atomic

transition frequencies as the dark matter field directly affects the values of fundamental constants through this coupling. AION can probe scalar dark matter with masses between 10^{-18} eV and 10^{-12} eV, corresponding to Compton frequencies $\omega = m_{\rm DM}c^2/\hbar$. Different configurations of the AION detectors (e.g. AION-10, AION-100) can probe for different ranges of dark matter mass and coupling strength. Figure 2.8 illustrates the sensitivity of the different AION setups to different scalar dark matter interactions in regards to the dark matter mass and the coupling strength.

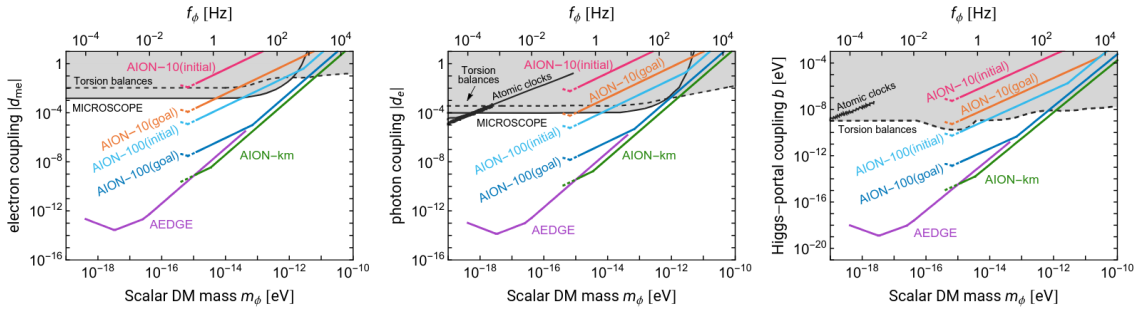

Figure 2.8: Sensitivities of the different AION detector configurations (different scale detectors) to three different dark matter interactions; scalar dark matter coupling to electrons (left), photons (middle) and through the Higgs portal (right). The plots show the parameter space that has been excluded by other experiments i.e. through equivalence principle violation searches [103], atomic spectroscopy [104], and the MICROSCOPE experiment [105]. Reproduced from: [54].

2.2 AI experiment landscape

There are currently several efforts worldwide to construct atom interferometer experiments for the detection of new physics. There are various proposal stage, prototype/proof-of-concept laboratory-based experiments as well as dedicated large-scale experiments each of which uses different cold atom technologies and technology configurations to construct a detector that could be sensitive enough to detect gravitational waves, dark matter, and other physical phenomena.

In this section, I outline the international landscape of atom interferometers. This section is based on the Terrestrial Very-Long-Baseline Atom Interferometry workshop summary paper [40] that took place in March 2023 at CERN and Ref. [106]. One of the main outcomes of the workshop was the establishment of a pathway towards an international long baseline atom interferometer proto-collaboration aiming for at least one km-scale atom interferometer-based detector to be in operation by the mid-2030s.

Several atom interferometer projects with baseline lengths of 10 to 100 meters have already been constructed or are in the planning stages. One such project is the 10-m fountain at Stanford built as part of the MAGIS collaboration [66]. Another key development is the Very Long Baseline Atom Interferometry (VLBAI) in Hannover [107] which has successfully implemented a 10-m baseline atom interferometer. Other 10-m atom interferometer projects include the Wuhan 10-m atom interferometer [108].

Next-generation atom interferometer set-ups with very long baselines are also in various stages of planning or construction. These include MAGIS-100 at Fermilab [66], MIGA in France [109] and ZAIGA in China [110]. MIGA, which is currently under construction, is expected to pave the way to the European ELGAR project [111]. Unlike most other experiments, which use vertical configurations, both MIGA and ZAIGA will operate in a horizontal configuration.

Among these next-generation projects is the Atom Interferometry Observatory and Network (AION) project, which forms the core of the next two chapters of this thesis. The program includes both a 10-meter prototype and a longer 100-meter detector (in a vertical baseline configuration), both of which are currently in the planning stages. The 10-meter detector will be built at Oxford, while possible sites for the next phase, the 100-meter baseline detector, are being investigated, including locations in the UK and at CERN

[112].

Operating the atom interferometers in a vertical configuration allows for increased sensitivity, as the interrogation times are longer due to the atoms being launched vertically and allowed to free fall for a longer period, extending the duration of interaction with laser pulses. This extended free-fall enhances the phase accumulation, as the phase shift scales with the square of the interrogation time. A key advantage is that the atomic clouds remain within the interferometry beam for the full duration of the sequence, reducing the need for frequent re-launches and thus minimising the introduction of additional differential phase noise. However, more than one baseline can be used in the horizontal configuration detectors to suppress the common-mode laser noise. All interferometers would be addressed by the same laser beam. Multi photon transitions can also be driven by counter-propagating beams, making the use of alkaline elements possible [40].

Table 2.2 gives an overview of the leading terrestrial long baseline atom interferometer projects along with their main characteristics. The table highlights their baseline lengths, atom species used and geographic locations as well as the techniques used to perform atom interferometry and manipulate and control the atoms. This comparison highlights the global effort to build atom interferometer based detectors that can explore a range of different physical phenomena.

Project	Baseline Length	Number of Baselines	Orientation	Atom	Atom Optics	Location
VLBAI	10 m	1	Vertical	Yb, Rb		Germany
MAGIS-100	100 m	1	Vertical	Sr	Clock AI, Bragg	USA
AION-10/100	10/100 m	1	Vertical	Sr	Clock AI	UK
MIGA	200 m	2	Horizontal	Rb	Bragg	France
ZAIGA	300 m	3	Horizontal	Rb, Sr	Raman, Bragg, OLC	China

Table 2.2: Comparison of different atom interferometer projects worldwide. Adapted from: [66]

The ultimate sensitivity of these detectors would be achieved by taking atom interferometers into space, benefiting therefore from huge baselines. This would not only eliminate

a lot of the noise they experience on Earth (from anthropogenic and geological sources), but they would also be able to search for additional effects that can only be probed from space. Examples of such ambitious projects include the AEDGE project [64], which is complementary to the AION program, and STE-QUEST [113].

Chapter 3

Experimental Apparatus for Ultra-Cold Atom Preparation

3.1 Introduction

The AION project requires that state-of-the-art atom interferometry techniques be used and developed to be sensitive enough to the physics it aims to discover. A key part in achieving atom interferometry is the production of ultra-cold atoms.

One of the main deliverables of the project is the building of dedicated Ultra-Cold Strontium Laboratories (UCSLs), conducting complementary R&D efforts in parallel, each having expertise in different aspects of the experiment and working on optimising different parts of the experimental process. The University of Birmingham leads the development of Large Momentum Transfer (LMT) techniques, which use sequences of light pulses to transfer multiple photon recoils to atoms, enhancing the sensitivity of interferometers to gravitational signals [67]. The University of Cambridge focuses on atom trans-

port, cooling, launch, and atom optics. This includes techniques to move ultra-cold atoms across vacuum chambers more efficiently and optimisation of the optics to increase the efficiency of cooling and atom interferometry [114, 95]. Imperial College London and the Rutherford Appleton Laboratory (RAL) lead the work on spin squeezing and high-resolution atom interferometry, aiming to make measurements below the quantum projection noise by engineering spin-squeezed quantum states of atoms [95], and to improve the resolution of interferometry. The University of Oxford is responsible for developing ultra-cold strontium atom sources and will host the first detector prototype, AION-10, in the Oxford Beecroft building [41].

This centralised production of the ultra-high vacuum (UHV) and the Lasers stabilisation (LS) systems allowed for faster production, which would otherwise take much more time by leveraging the expertise of the different institutions collaboratively. The results of this effort and more details on the approach and methods used for the centralised design and production of the UHV and LS systems are presented in Ref. [1].

During my PhD I have contributed significantly in setting up the Imperial College London UCSL and the UHV and laser systems. A major fraction of my time during my PhD has been spent on designing and assembling experimental hardware, including the assembly of the UHV chambers that are essential for cooling the atoms before they are launched into the interferometer. This chapter describes my contributions to the now state-of-the art experimental set-up, which is now able to cool atoms down to sub-micro-kelvin temperatures and perform atom interferometry using the metastable strontium-87 transition, achieving two of the main aims of the AION project's initial phase.

This chapter is organised as follows: Section 3.2 describes my work in relation to the sidearm development and assembly. A sidearm in the context of the AION project refers

to a dedicated vacuum structure, where atoms are initially cooled and prepared before being transferred into the main interferometry region. Section 3.4 presents my work in designing, building and testing the stray magnetic field compensation coils necessary for achieving ultra-cold atoms. These are followed by a presentation and discussion of the optical setup I built that is used to achieve a red MOT (Section 3.5.2). Section 3.6 discusses how optical injection is achieved and introduces an easy-to-assemble method of characterising the injection lock using heterodyne beat detection. Injection locking is necessary in the AION project to meet the demanding laser power and frequency stability, and spectral purity requirements for ultra-cold atom experiments, especially for operating the narrow-linewidth red MOT used to cool strontium atoms.

3.1.1 Hardware Requirements

The sequence for cooling the atoms in the AION experiment follows a similar set of methods as other cold strontium atom experiments [70, 115]. The sequence is outlined below:

1. Effusive emission of strontium atoms from a high-temperature oven.

2. Initial cooling and collimation of atoms using a 2D "blue" magneto-optical trap (MOT) in Chamber 1, forming a slow atomic beam.

3. Recapture and further cooling of the atomic beam in a 3D "blue" MOT within Chamber 2 (down to the Doppler limit of approximately 770 µK).

4. Additional cooling to microkelvin temperatures (down to the Doppler limit of approximately 180 nK) in a 3D red MOT.

5. Transfer of atoms into an optical dipole trap, followed by evaporative cooling.

6. Optical transport of the ultra-cold atoms to the interferometry region, either into Chamber 3 in test sidearms or the main vertical tube of the full-scale detector.

7. Atom launch, execution of interferometry, and subsequent measurement.

The relevant transitions used in the laser cooling sequence and interferometry are depicted in Figure 2.2 in Chapter 2.

Each of the institutions that work on hardware R&D for the project has a different vacuum system. While the vacuum systems at the University of Cambridge and Oxford consist of three chambers (see Ref. [1] for details), the vacuum system at Imperial is a two-chamber one, the CAD design of which is shown in Fig. 3.1.

All the stages in the cooling sequence require ultra-high vacuum to prevent unwanted particles from interfering with the cooling and interferometry sequence by preventing collisions of background gas with the atoms. Chamber 2 of the Imperial vacuum system requires that the pressure is $\lesssim 10^{-10}$ mbar.

Stages 1-2 of the cooling sequence outlined above take place in Chamber 1, and stages 2-5 happen in Chamber 2 of the vacuum system. Strong magnetic fields are required in both chambers. These are supplied by NdFeB permanent magnets in Chamber 1 due to their ability to reduce the power consumption required and the requirements for cooling. The required magnetic field gradient in Chamber 2 is supplied through the use of high-current, water-cooled coils, as it needs to be changed for different stages in the sequence. More details on the magnet design and their characterisation are presented in [1].

The sequence uses different types of lasers depending on the stage and transition requirements. The 461 nm transition is used for the 2D and 3D blue MOTs (Steps 2 and 3 of the sequence). The 689 nm transition is used in the 3D "red" MOT. Atom interferometry

in AION is performed using the 698 nm "clock" transition of the strontium-87 isotope. For narrow transitions (red MOT and atom interferometry), narrow linewidth, cavity-stabilised [1] lasers at 689 nm and 698 nm are required. For broadband transitions (blue MOT and repumping), wavemeter-locked (using a High Finesse WS wavelength meter) Toptica ECDL lasers at 461 nm, 679 nm, and 707 nm are required (see Section 3.5.1. For far-off resonance transitions (used in the dipole trap), a free-tuning laser at 1064 nm is required.

3.2 Sidearm Assembly

The sidearm at Imperial consists of two vacuum chambers, one for the 2D MOT and one for the 3D MOT and squeezing cavity. Figure 3.1 shows the CAD design of the two chambers in the sidearm frame. Chamber 1 contains the strontium oven, which limits how low the vacuum pressure can go. Therefore, there are two separate ion pumps, one for each chamber. Chamber 2 is pumped using a 20L/s ion pump along with a NEG (non-evaporable getter) cartridge pump. A differential pumping aperture of 3 mm diameter and 15 mm length separates the two chambers. Chamber 1 contains multiple viewports around its sides. Four of the viewports are used to attain a 2D MOT, and one is placed at the front, facing the outside of the sidearm and used for fluorescence imaging. The four 2D MOT viewports do not face the oven directly to avoid being coated with strontium while the oven is operating, although it is not always possible to completely avoid this. Chamber 1 requires that the background pressure be less than 10^{-9} mbar to avoid affecting the base pressure of Chamber 2.

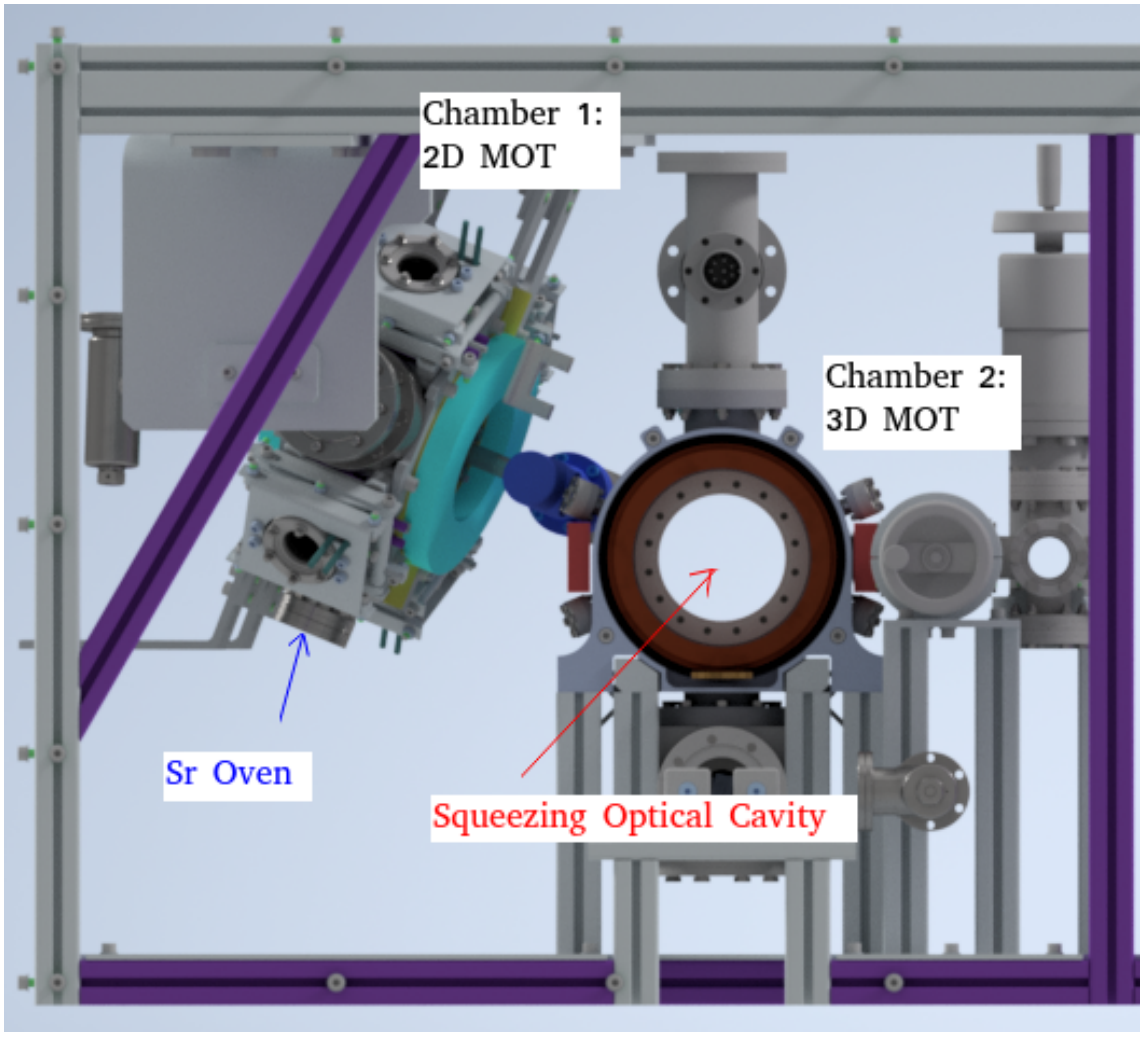

Figure 3.1: The CAD design of the two chambers in the sidearm. The position of the Sr oven and the cavity for squeezing are also indicated.

3.2.1 Ultra-high vacuum system - Chamber Assembly

The sidearm assembly began with Chamber 1, following a standard ultra-high vacuum (UHV) cleaning protocol to minimise contamination. All components exposed to vacuum were cleaned using a multi-step process. The process included cleaning pieces that would be in contact with the vacuum following a standard procedure for vacuum-standard cleaning, which included immersing the pieces in acetone to remove grease and oils, washing with decon detergent and then distilled water to remove detergent residues (separately) in

that order. An ultrasonic bath was then used to remove particles from surfaces. This was followed by pre-baking the pieces in an oven at 120°C to remove water and hydrocarbons.

Following cleaning, the chamber coated viewports were installed to provide optical access for laser cooling and spectroscopy. An internal mirror was also mounted inside the chamber for performing spectroscopic measurements. Figure 3.2 shows images taken during the assembly process.

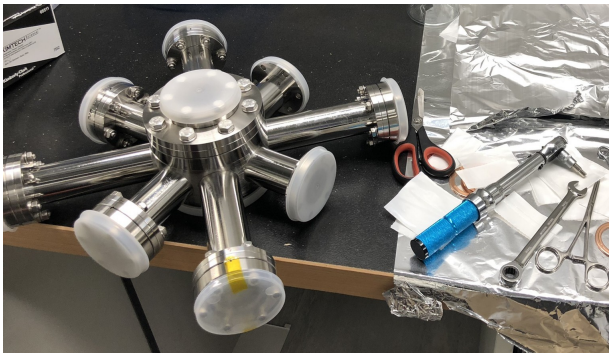

(a) Assembled Chamber 1

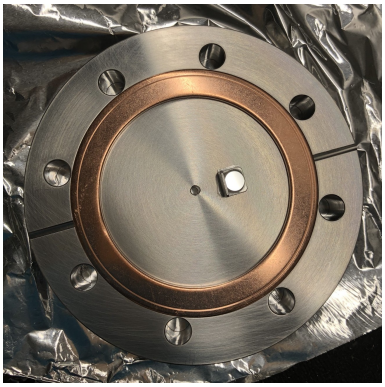

(b) Internal mirror for spectroscopy.

Figure 3.2: Assembly of Chamber 1. (a) The assembled chamber 1 (excluding the strontium oven) with installed viewports. (b) The internal mirror used for in-situ spectroscopy of trapped atoms.

After attaching the viewports and mirror, a glovebox was used to load the Sr oven with strontium. The strontium oven is made of stainless steel and was specially designed and produced for AION by the Oxford team. Pictures of the oven during the loading procedure are shown in Figure 3.3. A glovebox is used as strontium is highly reactive to oxygen. The glovebox was therefore filled with argon gas to push out as much oxygen as possible to prevent oxidization during the loading of the oven.

The oven consists of the main cylindrical oven part where strontium metal is inserted and connected to a Conflat flange (CF40) via a thin-walled stainless steel tube with low

thermal conductance. A nozzle sits near the opening of the strontium oven cylinder. The stainless steel disk nozzle was created through laser machining and is secured in place using a C-clip. It contains 150 circular channels, each 0.3 mm in diameter and 3 mm in length. Rather than being mounted flush with the cylinder's end, the nozzle was positioned further along in the oven body to minimise heat loss. The tube that connects the oven body to the flange is open to allow for six cartridge heaters and two thermocouples to be inserted to heat the oven. This design eliminates the need for any electrical feedthroughs.

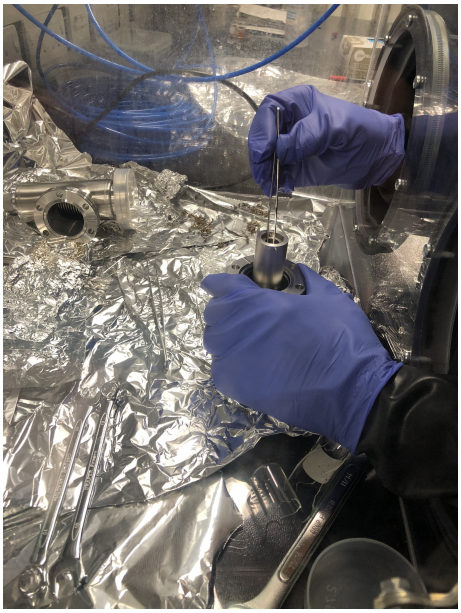

(a) Loading the oven

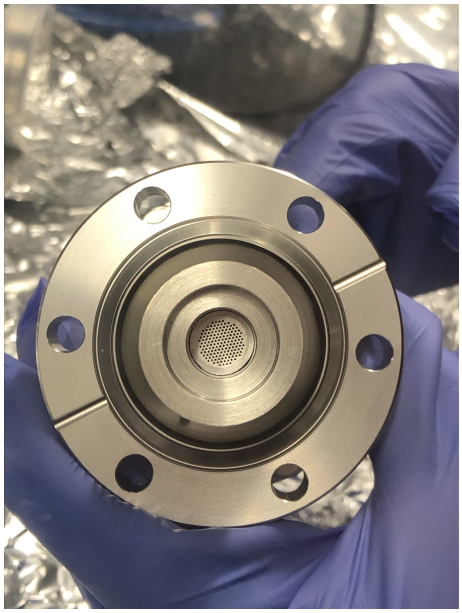

(b) Oven nozzle

Figure 3.3: Pictures taken during oven loading. Once the oven was loaded with solid strontium, the nozzle was then placed in the cylindrical body of the oven, and the vessel was vacuum sealed before being led out of the controlled box.

Once the oven was loaded with as much strontium as possible (a few grams), it was sealed and taken out of the glovebox. Chamber 1 was attached to the sidearm frame along with the ion pump. Once the chamber was correctly attached, the oven was carefully and as quickly as possible attached to the bottom inlet of the chamber to avoid as much oxidisation as possible.

Thermocouples were taped on various points on the chamber, and a Leybold TURBO-LAB high-vacuum pumping system was attached. The chamber was then wrapped in foil to reduce thermal gradients during bakeout. The turbo-pump was used to reach a pressure of the order of 1×10^{-7} mbar. Figure 3.4 shows the frame with chamber 1 installed before and during baking and vacuum pumping. The maximum temperature for the baking was determined based on what the viewports can withstand before breaking. This was determined to be around 115^oC. The thermal differences between the different viewports was attempted to be kept to a minimum. The baking was therefore done using a rate of approximately 5^oC per hour. Once baking was done the whole chamber was checked for any leaks using a helium outlet. This ensured that the vacuum was not broken during the procedure, either at the joints between the viewports and the chamber or due to any melting of the glass viewport's sealing to the rest of the structure. It must be noted that Chamber 1 was initially set up without Chamber 2, and the aforementioned procedure was carried out exclusively on Chamber 1.

Once a good vacuum was ensured, the oven was heated up to around 500^oC to release Sr atoms inside the chamber and fluorescence spectroscopy was used to verify the nominal oven flux. A picture of the fluorescing atoms is shown in Figure 3.5.

A similar procedure was carried out for assembling Chamber 2. While heater tape was used when only Chamber 1 was baked, when Chamber 2 was attached, an insulated enclosure was used to bake the whole system. It should also be noted that another difference in the Chamber 2 design for the Imperial system, in contrast to the rest of the institutions, is the addition of a cavity that will be used for spin-squeezing experiments.

During baking, the turbo pump was on for about 20 days, after which the ion pumps were turned on. To monitor the pump-down process and vacuum stability, pressure data

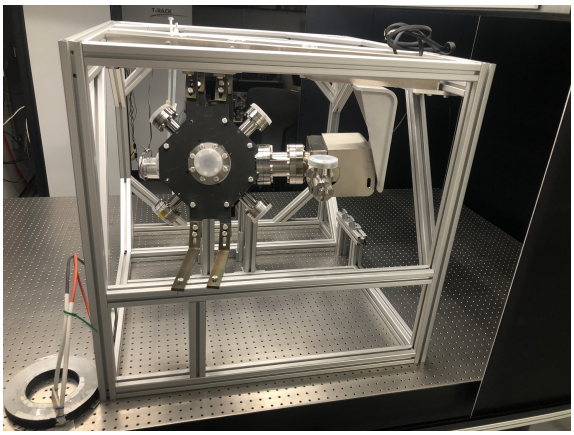

(a) Sidearm with chamber 1 and the ion pump attached

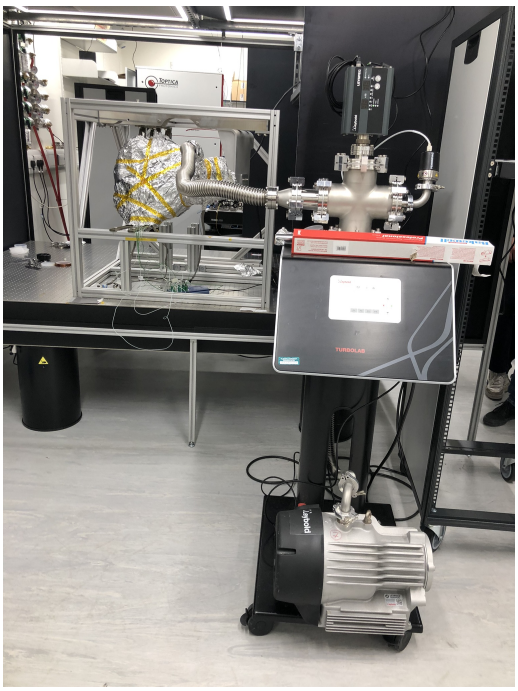

(b) Chamber wrapped in foil (used to bake the chamber) and the vacuum pump during vacuum pumping

Figure 3.4: Pictures of (a) the sidearm with chamber 1 and the ion pump attached and (b) the chamber wrapped in foil (used to bake the chamber) and the vacuum pump during vacuum pumping.

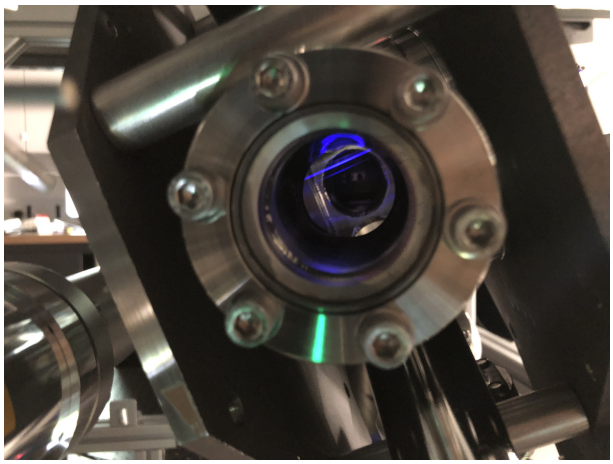

Figure 3.5: Fluorescent light (blue line inside the chamber) produced by strontium atoms during spectroscopy.

were recorded for both Chamber 1 and Chamber 2. Figure 3.6 shows the pressure of each chamber, plotted on a logarithmic scale against elapsed time in minutes, with data sampled at five-minute intervals during one of the pump down procedures. At the time the turbo pump was turned off, the pressure in the chambers was around the order of 1×10^{-8} mbar. After the ion pumps were turned on, Chamber 1 reached a steady state pressure of about 3.4×10^{-10} mbar while Chamber 2 reached a pressure of 1.3×10^{-11} mbar during the same pump down cycle.

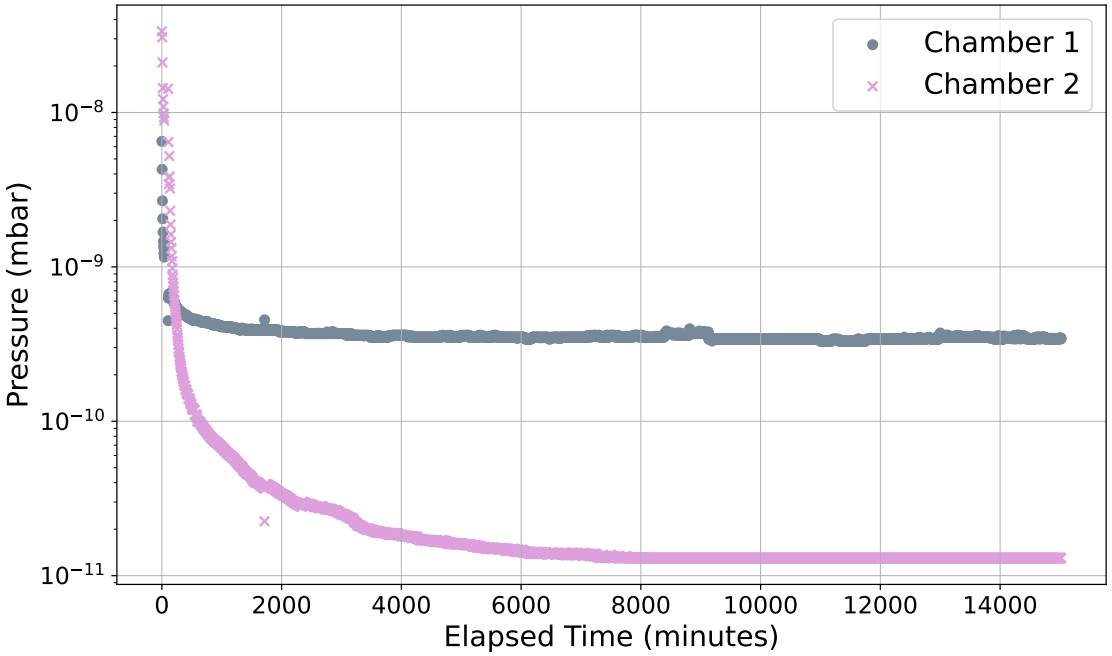

Figure 3.6: Pressure profiles of Chamber 1 and Chamber 2 during one of the ultra-high vacuum (UHV) pump-downs. The plot shows pressure (in mbar) on a logarithmic scale versus elapsed time in minutes. Data sampled at 5-minute intervals.

As mentioned in the previous subsection, the AION sidearm requires precisely controlled magnetic fields in two chambers to facilitate atom cooling and trapping. A hybrid system consisting of eight N52 NdFeB permanent magnets arranged to create a 2D quadrupole field with strong radial gradients of approximately 3.7 mT/cm in the x-y plane is used in Chamber 1. These magnets are supplemented by water-cooled aluminium tape trimming

coils capable of providing an additional maximum of 2.4 mT/cm gradient adjustment. Separate axial compensation coils (tape-wound coils) are added in addition to the above. This design minimises stray fields while allowing fine control of the MOT position and field strength.

Chamber 2 utilises only electromagnets. This allows large range gradient control and for ramping the total field to zero. There are two assemblies of square-profile hollow copper conductor coils run in anti-Helmholtz configuration. Each assembly contains two water channels for cooling. The setup also includes passively cooled auxiliary windings for DC offset field trimming. The system produces a field gradient of $39\,\mu T\,cm^{-1}\,A^{-1}$ and can sustain currents up to 200 A continuously without exceeding 30 °C due to the water cooling. With a self-inductance under 400 µH, the current can be rapidly ramped from 130 A to 10 A within 1 ms using a 40 V reverse voltage, facilitating the critical transition from blue MOT to red MOT.

The magnets and coils were therefore added to the sidearm and the two Chambers after installation of these magnets and coils, are presented in Figure 3.7.

3.3 Experimental Control

For the experimental control system for the AION experiment at the Imperial lab, we are using ARTIQ (Advanced Real-Time Infrastructure for Quantum physics) [116]. ARTIQ is a control and data acquisition system specifically designed for quantum physics experiments. It consists of both specialized hardware and software components working together.

The system is built around an FPGA-based controller that provide the precise timing and

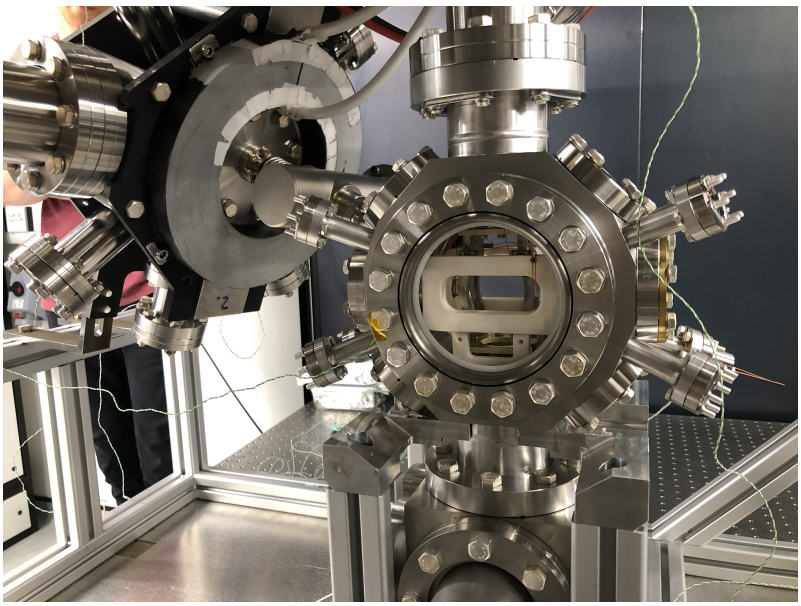

(a) Chamber 1 with coils installed.

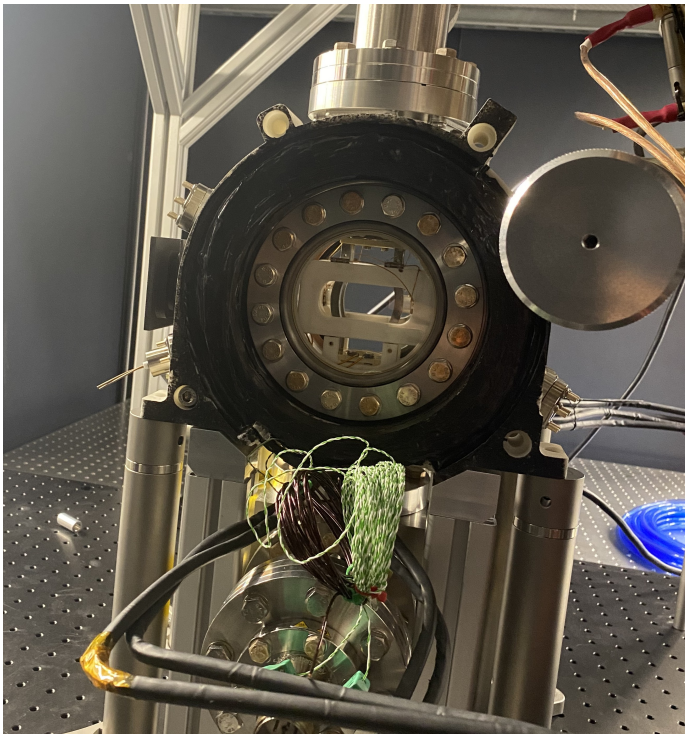

(b) Chamber 2 with coils installed.

Figure 3.7: Pictures of the two chambers after the installation of the (black painted) coils.

real-time processing capabilities essential for our experiments. The provided hardware is complemented by a Python-based programming environment that provides an accessible way to define complex experimental sequences without sacrificing performance. The code runs on the computer using a remote procedure call (RPC) mechanism.

The FPGA (the core device) used to compile and execute the time-critical code (a kernel) has a nanosecond timing resolution and sub-microsecond latency. This ensures your experimental sequences run exactly as programmed without timing jitter, which is critical when manipulating states in our atoms. The design of the FPGA is highly adaptable.

The ARTIQ hardware is called Sinara hardware. The hardware consists of different boards/devices that can be purchased and assembled in a flexible way to adapt the system according to the lab's needs.

3.4 Magnetic Field Compensation Coils - Chamber 2

External magnetic fields, e.g. Earth and stray magnetic fields from nearby equipment such as the ion pumps, interfere with the MOTs. These background magnetic fields shift the zero-point of the magnetic field gradient and alter the Zeeman splitting across the trap. As a result, the position-dependent optical forces that trap and cool the atoms become distorted or misaligned, degrading the efficiency and symmetry of the trap, particularly when the field gradient is changed. Compensation coils are therefore used to cancel out these magnetic fields. The Chamber 2 MOT coils included a pair of coils for the MOT (Y) axis. Additional coils to cover the other two axes (X-cavity axis and Z-vertical axis) are also necessary for chamber 2 to achieve as low temperatures as possible in the red MOT. As part of my contribution to this project, I designed, built, and characterised these additional compensation coils. The design process, implementation, and characterisation

of the coils are detailed in this section.

Two orthogonal pairs of coils are placed along two axes in the sidearm structure, which run in a Helmholtz configuration to produce a uniform magnetic field. There needs to be a pair of coils on the two sides of Chamber 2 (along the cavity axis) and a pair of coils at the top and bottom of the sidearm along the vertical axis to compensate for the Earth's magnetic field and the ion pump's stray magnetic field. These coils are essential for cooling the atoms in the red MOT and achieving sub-micro-kelvin temperatures as required by atom interferometry. The pair of coils along the cavity axis will be particularly important when performing squeezing.

When designing the coils, the power dissipation produced by them, the magnetic field to be compensated for, and the limited space available along the cavity axis were considered. The magnetic field at the surface of the Earth ranges from around 22 μT to 67 μT (0.22 to 0.67 G) [117, 118]. At the Blackett Lab at Imperial College London, where the apparatus described here is located, the total magnetic field intensity is around 49 μT as calculated using the International Geomagnetic Reference Field (IGRF) Calculator [119]. Each set of coils needs to compensate for at least 50 μT but were designed to compensate up to 5 Gauss (0.5 mT) of magnetic field, including a big safety margin for the ion pump magnetic field and any other stray magnetic fields that could be generated in the lab.

An enamelled copper wire of rectangular cross-section (1 mm x 2 mm) was used, which, according to calculations, dissipates less power than the same length of circular cross-section wire. The power dissipation calculations performed took into account parameters such as the wire dimensions, coil resistance, and current specifications. One of the main criteria was that the coils were to be driven with a maximum current of around 5 A, for ease of buying the coil drivers.

3.4.1 Magnetic Field Modelling

To model the magnetic field produced by a rectangular loop of wire of many turns (N) along the z-axis the following equation is derived from [120].

$$B_z = N \cdot \frac{\mu_0 I}{\pi} \frac{\alpha b}{r} \left(\frac{1}{r^2 - b^2} + \frac{1}{r^2 - a^2} \right) \tag{3.1}$$

where a is half the length of the loop, b is half the width of the loop, μ_0 is the magnetic permeability of vacuum, I is the current in the loop and $r^2 = a^2 + b^2 + z^2$. Equation 3.1 is derived by assuming that $x = y = 0$ since we want to know the magnetic field in the middle of the x-y plane and along the z-axis (perpendicular to the x-y plane) where the atoms will be found.

To decide on the number of turns we take into consideration our criteria, i.e. a) 0.0005 T of a magnetic field generated by each coil in the middle of the cavity on both axes b) a maximum of 5 A to be supplied to each coil and c) take into account the limited space around the cavity when deciding on the number of turns. To decide the number of turns, which is the ultimate limiting factor, the maximum possible dimensions that the channels can have were decided by measuring the space available around chamber 2 (for the cavity axis coils) and the dimensions of the sidearm frame. The dimensions of the rectangular loop for the cavity axis and the vertical axis were approximately (0.16×0.061) m and (0.9×0.96) m, respectively. Taking these dimensions into account, the distance from the coils to the middle of the cavity and the dimensions of the loops, the model in Equation 3.1 was used to determine the number of turns that each coil would have. Figures 3.8 and 3.9 show the magnetic field as a function of the current supplied and the number of turns for a single coil of the given dimensions.

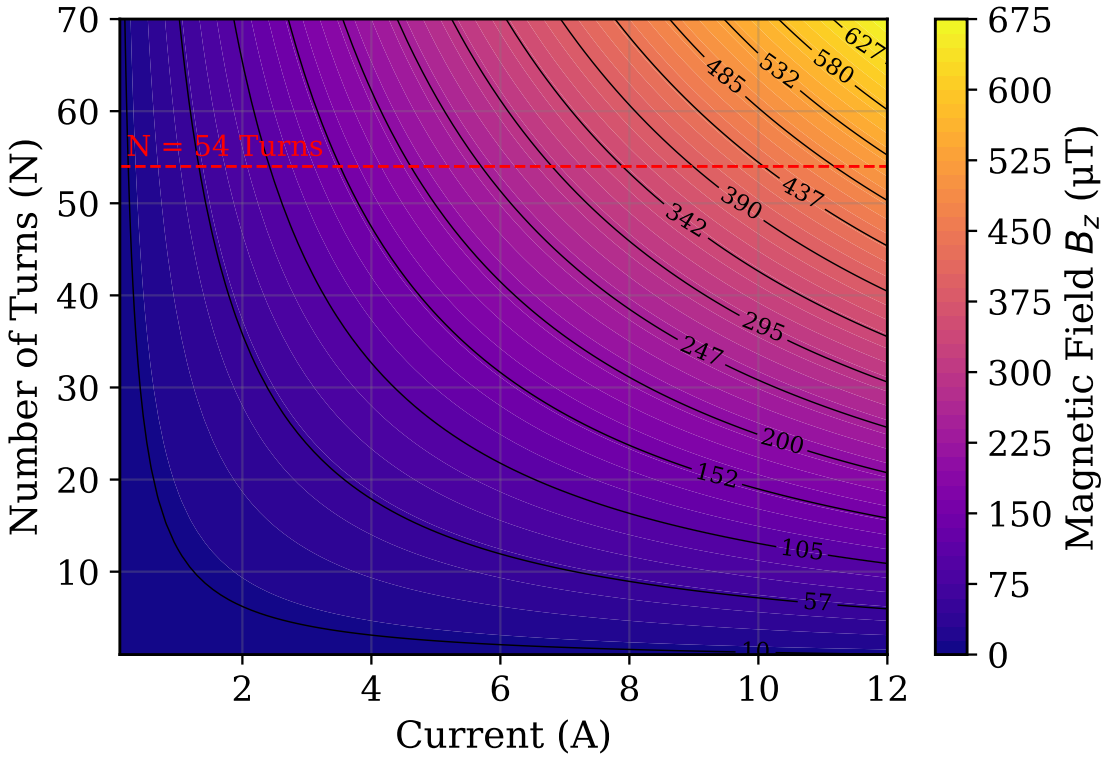

Figure 3.8: Colourmap of the magnetic field component B_z (in μT) as a function of the current (I) and the number of turns (N) in the cavity axis coil. The calculations are performed at a fixed distance $z = 116.5$ mm from the centre of the coil. The magnetic field is derived using theoretical expressions for a rectangular coil geometry with half-length $a = 0.08$ m and half-width $b = 0.0305$ m. The colour gradient indicates the magnitude of B_z, with higher values corresponding to stronger magnetic fields at the specified position. The red line indicates the chosen number of turns (N = 54).

3.4.2 Compensation Coils Design

The wire for the coil were wound around sets of channels that were designed specifically to fit the dimensions of the chamber frame and the left and right of the cavity, where we have limited space. For the top and bottom coils, off-the-shelf aluminum channels [1] were used and cut to the right dimensions to fit around the frame (926 mm and 986 mm). The channels were joined at the four corners with 3D-printed connectors designed to fit the channels. The CAD design of the corners and the coils and one of the coils are shown in

[1] https://www.aluminium-online.co.uk/product/5-8-x-5-8-x-1-8-aluminium-channel/

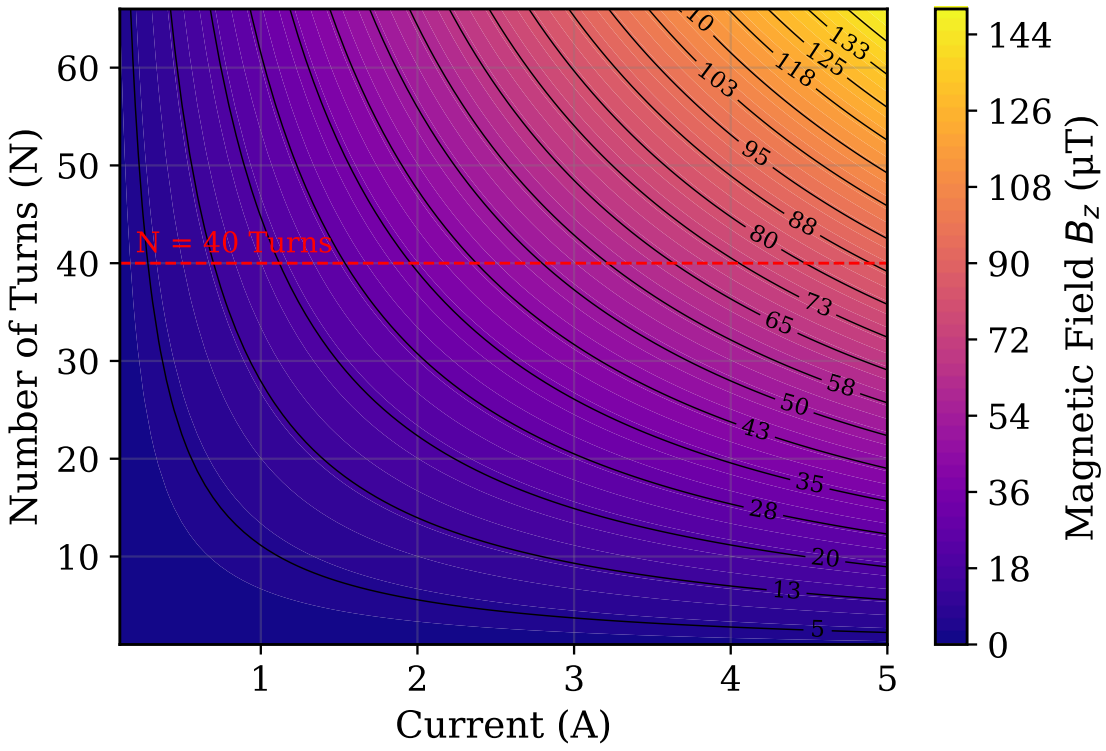

Figure 3.9: Colourmap of the magnetic field component B_z (in μT) as a function of the current (I) and the number of turns (N) in the coil. The calculations are performed at a fixed distance $z = 0.5\,\text{m}$ from the center of the vertical axis coil. The coil geometry is characterised by a half-length $a = 0.48\,\text{m}$ and a half-width $b = 0.45\,\text{m}$. The colour gradient represents the magnitude of B_z, with higher values indicating stronger magnetic fields generated at the specified position. The red line indicates the chosen number of turns (N = 40).

Figure 3.10. The top and bottom coils had 40 turns (10 layers).

For all the coils, stycast (Loctite 2850FT) mixed with Catalyst 9 (Locite Black Epoxy Encapsulant) was used to keep the wire in place and taut while winding and avoid any shorts. To wind the big coils, an in-house winding mechanism was built which was an imitation of the frame of the sidearm and was placed in a four hole flange bearing (12.7mm from RS) by attaching it to a Thorlabs post. The same bearing was used to wind the smaller coils.

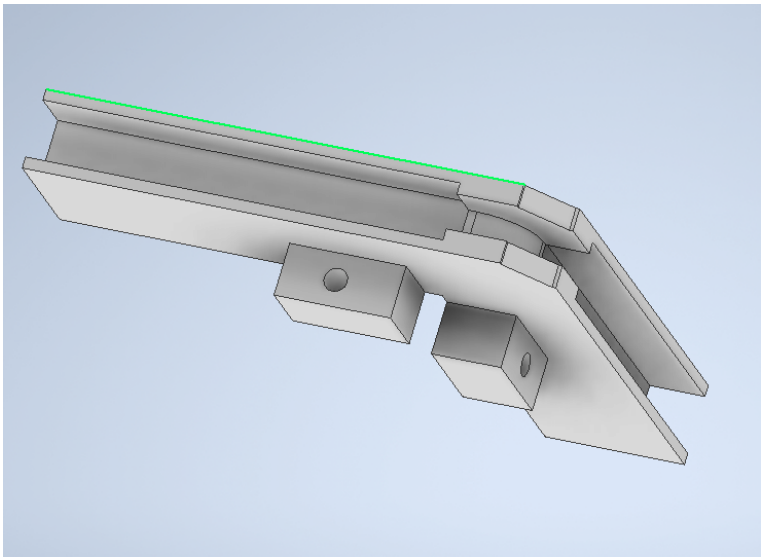

(a) CAD Design of the corners for the top and bottom coils.

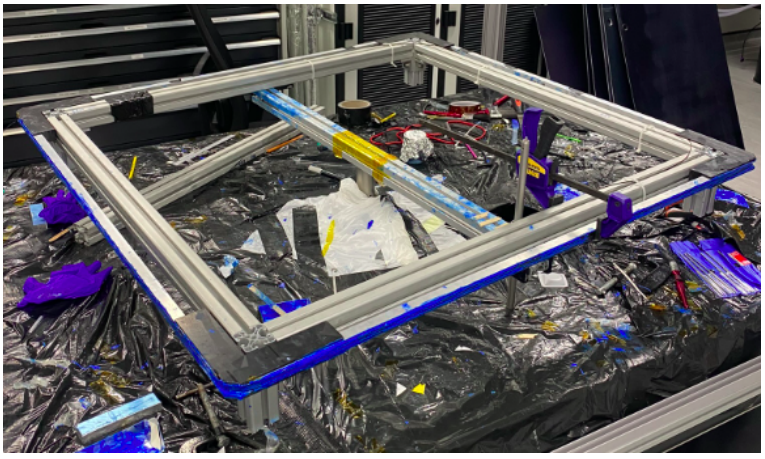

(b) Top coil after completion.

Figure 3.10: Vertical axis compensation coils.

The cavity axis channels required a more sophisticated design due to the limited space available. There also needs to be a cooling pipe with water running through it below the wires to cool down the area around and prevent the dissipated heat from affecting the rest of the delicate system. The position of these channels is indicated in Figure 3.1 by the red blocks on the left and right of chamber 2. The final design includes an empty clearance window in the middle for as little obstruction of the viewports as possible. The final design I produced on CAD as well as one of the coils installed on the chamber are

shown in Figure 3.11. The material used to print them is graphite which is stiff enough to withstand the tightly wound wire. There was a total of 54 turns in each of the coils. The first layer in each coil had 5 turns and there are a subsequent seven layers with seven turns each.

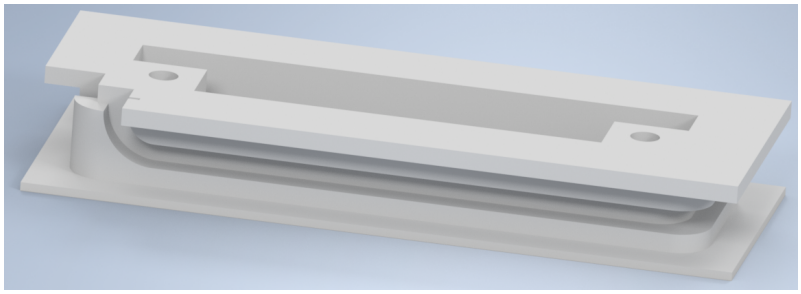

(a) CAD Design

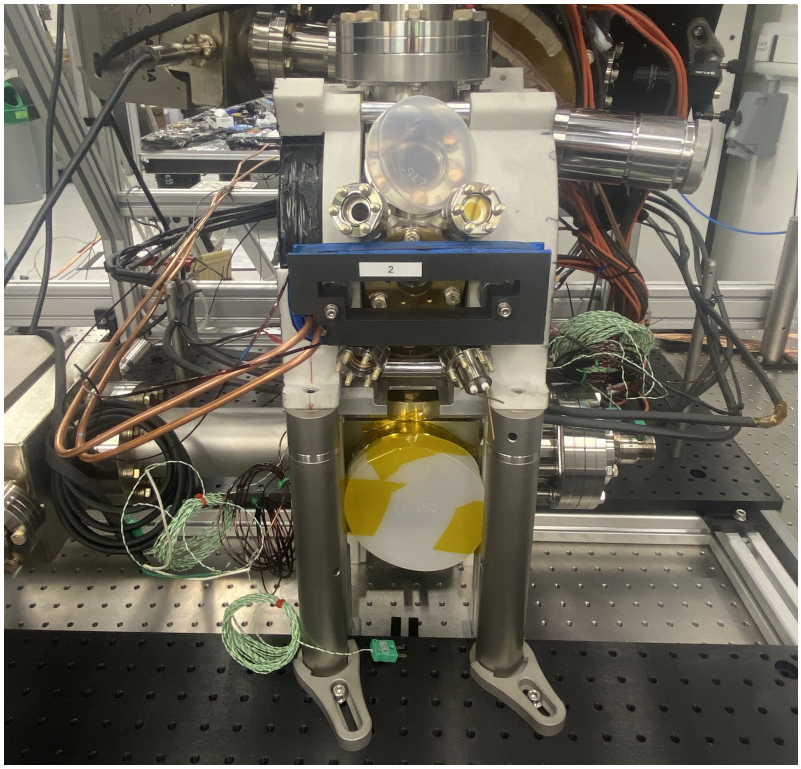

(b) Installed cavity axis coils.

Figure 3.11: Top: The CAD design of the cavity axis compensation coils channels with a channel for the cooling pipe. Bottom: One of the cavity axis compensation coils is installed on the chamber with the cooling pipes directed towards the water outlet.

The compensation coils are driven directly by Kepco BOP series bipolar power supplies.

These supplies take an analog voltage input from ARTIQ, which modulates the output current. A calibration measurement was performed to relate the ARTIQ output voltage to the resulting current passing through the coils in amps.

3.4.3 Cavity Axis Compensation Coils Testing

To ensure the coils are working as intended and produce the desired magnetic field, the cavity axis compensation coils were tested. A Bartington Hall three-axis sensor (MAG 13MS-100), which outputs 100 $mV/\mu T$ was used to measure all three field axes as the sensor is moved along the z-axis (rectangular solenoid axis). The coil was placed on the floor and the sensor was raised above the ground using some plates for the z-axis to align with the middle of the x-y plane of the coils.

Distance from the coils to the sensors was measured using markings on the floor which were determined using a ruler. The ruler was removed as it was made of steel and had an impact on the magnetic field. Measurements were taken from 40 mm and above. A measurement of the field in the X, Y and Z axes was taken along with the supplied current. The voltage was then converted to the magnetic field using the calibration value of the instrument (100 $mV/\mu T$) for all three axes. The field amplitude per amp is plotted in Figure 3.12 as a function of distance.

The plot illustrates that the data agrees with the model. Therefore, the coil is working as intended, producing the required magnetic field at the required position.

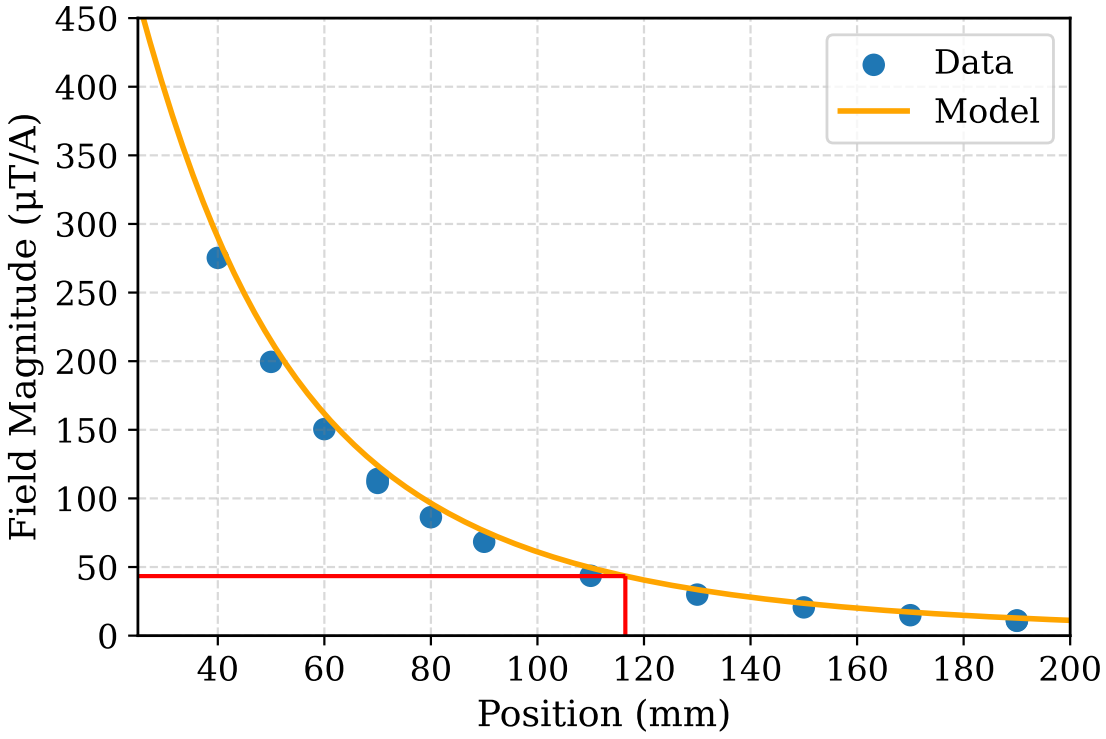

Figure 3.12: Plot of the field magnitude per amp as a function of position (distance z away from the coils). The blue points show the data measured for one of the cavity axis coils. The yellow line represents the theoretical magnetic field generated by the model in Equation 3.1; it is not a fit to the data. The red line indicates the value of the magnetic field per amp at z = 116.6 mm, which is 43.4 (according to the model). The data was taken by Charles Baynham.

3.4.4 Quantifying the Currents Needed to Compensate for Background Magnetic Fields

To determine the stray magnetic fields that should be compensated for at the location of the MOT, Zeeman absorption spectroscopy was used to determine the Zeeman splitting of the excited state caused by the magnetic fields. The spectroscopy was performed on the $^1S_0 \rightarrow {}^3P_1$ transition in ^{88}Sr. The energy shift of a Zeeman sublevel is given by:

$$\Delta E = \mu_B g_J M_J B = h\Delta\nu \tag{3.2}$$

where ΔE is the Energy shift of the atomic level, μ_B is the Bohr magneton ($\approx 9.274 \times 10^{-24}$ J/T, g is the Landé g-factor (depends on the specific atomic state), m_F is the magnetic quantum number of the hyperfine level and B is the magnetic field strength. $\Delta\nu$ is the frequency shift and h = Planck's constant ($\approx 6.626 \times 10^{-34}$ J $\cdot$ s).

A set of different known currents were supplied to each set of compensation coils along all three axes, and the resulting Zeeman splitting in the absorption spectrum was observed. This allowed for the frequency detuning of the absorption peaks to be measured. The point at which the σ^+ and σ^- peaks became symmetric around the centre (zero detuning from the transition frequency), denoted a zero net magnetic field along that axis. Therefore, the current needed to cancel out the background field was determined this way.

From the Zeeman shift measurements, the compensation coils produce magnetic fields of approximately 0.0276 mT/A (X), 0.0766 mT/A (Y) and 0.0224 mT/A (Z). These values validate the expected field strengths from the coil design.

For $M_J = 1$ and a g_J factor of 1.5 for $^{88}Sr\ ^3P_1$, it was found that the magnetic field needed to be compensated for in each axis is given by:

$$B_{\mathrm{bg},X} \approx 81 \text{ mG}$$

$$B_{\mathrm{bg},Y} \approx -7 \text{ mG}$$

$$B_{\mathrm{bg},Z} \approx -150 \text{ mG}$$

These numbers validate the ability of the compensation coils to cancel out the required magnetic field in all three axes. The magnitudes of the background fields are consistent

with the expected strength of the Earth's magnetic field at the lab location, suggesting that the primary source of these stray fields is geomagnetic.

The Zeeman spectroscopy measurements described here were not performed by me but are included to demonstrate the operation and effectiveness of the compensation coils that I built. The data shown were taken by Richard Hobson and Alice Josset, and the use of these results has been agreed upon for this thesis.

3.5 Laser Systems for Cooling and Trapping in a 3D Red MOT

This section presents the optical setup used to achieve a 3D Red MOT and is adapted from Ref. [2].

3.5.1 Laser Stabilisation System

The lasers required for the cooling sequence are outlined in Section 3.1.1. The blue MOT (461 nm) and repumping (679 and 707 nm) lasers require stabilisation at the 1 MHz level which can be achieved using software-based PID locking to the wavelength meter (High Finesse WS8). Toptica ECDLs are used to provide the lasers at all of these frequencies.

The 689 nm laser used for the red MOT and the 698 nm laser used for atom interferometry require precise frequency stabilisation and significantly higher precision than the other lasers. The 689 nm laser must be stabilised at approximately 1 kHz or better to create consistent atom samples in the narrowband stirred red MOT [75] and to match the MOT position reliably to the location of the dipole trap [70]. The narrow-linewidth 698 nm laser requires frequency stabilisation at approximately 10 Hz precision to enable reliable high-

fidelity π-pulses when addressing the clock transition, which is essential for achieving large momentum transfer operations [67, 121] in our atom interferometry scheme.

The stabilization is achieved through a notched reference cavity system purchased from Stable Laser Systems employing the Pound-Drever-Hall (PDH) technique. This approach uses frequency modulation of the laser light and detection of the cavity reflection to generate error signals that are fed back to the laser controllers. For frequencies that don't align with cavity modes, a dual sideband locking method is implemented, allowing stabilization at frequencies offset from cavity resonances. Details on the optical system design is presented in [1].

This high-precision frequency stabilization system is crucial for the reliable operation of the 3D red MOT used in the experiments described in this thesis, providing the frequency stability necessary for consistent atom sample preparation.

3.5.2 The 689 nm Laser system

This section presents the laser system used to obtain the optical beams required to achieve a narrow-band red MOT. To reach temperatures below $\sim 1\,\mu$K, the red MOT requires 689 nm laser light with $\lesssim 1$ kHz linewidth. The light is created and delivered to the 3D MOT chamber using the optical setup shown in Figure 3.13, which includes two main parts: injection locking and the 3D MOT laser light delivery optics. The 689 nm seed laser light is supplied to the laser stabilisation and MOT delivery systems by a 689 nm Toptica DL Pro ECDL, which has a maximum power output of around 25 mW and a specified free-running linewidth of 50 kHz at 5 µs. The seed ECDL is frequency stabilised to an ultra-low expansion glass optical cavity, and its linewidth is narrowed via the Pound-Drever-Hall technique [122] as described in 3.5.1.

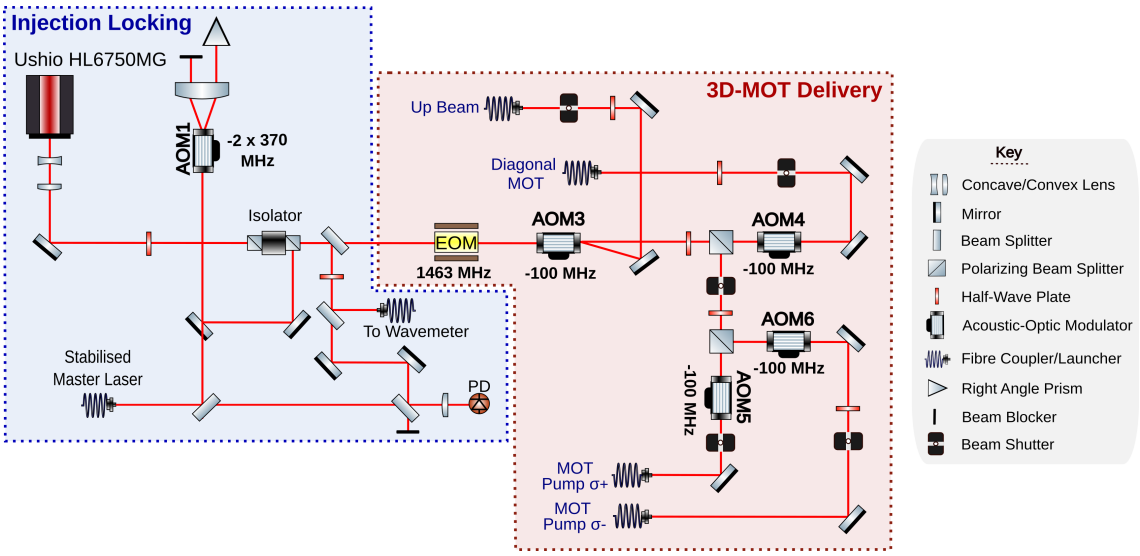

Figure 3.13: Laser system and optical setup for the delivery of light to the 3D red MOT. The RF drive of the AOMs is created using an Urukul module from the ARTIQ experimental control suite [123] which includes four AD9910 Direct Digital Synthesis devices. Light is delivered to the atom chamber via polarisation-maintaining optical fibres. The fast-modulation capability of the AD9910 is used to implement intensity feedback loops using signals from photodiodes after polarisation cleanup optics near the atoms. Sawtooth modulation for the broadband MOT stage is implemented using the AD9910's linear ramp generator and applied to AOM1, used for modulating the seed laser's frequency pre-injection. AOM1 is driven using an Mini-Circuits ZHL-1-2W-S+ amplifier, while all other AOMs are driven using ZHL-3A-S+ amplifiers.

For optimal operation of the frequency-modulated broadband red MOT, the intensity of the red light should be several hundred times the transition's saturation intensity ($3\,\mu W\,cm^{-2}$) - more than can be delivered from the seed laser alone. [124, 125] To achieve this, a Ushio HL6750MG diode is included in the delivery system, which has a maximum power output of around 50 mW and a nominal central lasing wavelength of 685 nm. This diode is injection-locked to the seed light with a controllable offset.

The diode is housed in a temperature-stabilised aluminium enclosure, which was designed by the Cambridge team. Light from the cavity-stabilised seed laser is passed through a double-pass acousto-optic modulator (AOM) system and an optical isolator and then

injects the amplifier laser diode. AOM1 permits fast control of the MOT beam frequency, used for example in the broadband MOT stage. Cylindrical lenses are used to shape the laser diode output into a circular beam. Once the injected beam passes through the isolator, it proceeds to take two paths, one through the rest of the MOT delivery system and the other to the injection characterisation setup. Details on injection locking and how it is achieved and characterised are discussed in Section 3.6. The AOMs in the 689 nm set-up are controlled using the ARTIQ crate depicted in Figure 3.14.

Figure 3.14: ARTIQ crate configuration used to control the 689 nm laser system AOMs. The setup includes a Kasli seed controller (which provides sequence timing control), Urukul AD9910 Direct Digital Synthesizers (DDS) boards for generating RF signals to drive AOMs, Mirny (PLL/VCO-based microwave frequency synthesiser) modules, and a Sampler (analog-to-digital converter (ADC)) module used to digitise analog signals.

The 100 MHz AOMs are used for active intensity control and are driven by a SU-Servo module from the ARTIQ experimental control system. This provides FPGA-based PI control of the beam intensity delivered to the chamber. For the ARTIQ SU-Servo feature, the “Urukul” unit is used in combination with a DAQ input board (“Sampler”) to form a laser-intensity servo. The photodiode signal is digitized and passed through a transfer

function implementing proportional and integral gain and used to modulate the RF drive to the single-pass AOMs in Figure 3.13.

To characterise the RMS noise of the intensity of the beam in-loop of the servo, we measured the voltage over a period of approximately 0.12 s. A Fast Fourier Transform was then applied to the voltage time series data to filter out any noise that lies outside the range between the first non-DC frequency up to 20 kHz. The filtered frequency components are then converted back to the time domain and the Root Mean Square Noise is calculated.

At the photodiode setpoint of 1.5 V (used for the broadband red MOT stage), the RMS noise, integrated over the frequency range of 50 Hz to 20 kHz, is measured to be 0.16 mV. This translates to an in-loop absolute intensity noise of $0.256\,\mu W\,cm^{-2}$.

For the results presented in this thesis, ^{88}Sr is used for the initial testing of the MOTs. In future experiments and in AION, ^{87}Sr will be used, which adds additional requirements for the laser system to address the hyperfine structure levels. To meet these requirements, the frequency of the 689 nm light will be modulated by a resonant free-space electro-optic modulator (EOM) driven at 1463 MHz. The +1 frequency sideband of the EOM will be tuned to address the $F = 9/2 \rightarrow 9/2$ transition, resulting in "stirring" of the red MOT, a method used to redistribute the population in the m_F sublevels and increase the efficiency of trapping [126]. The carrier beam will be used to target the $F = 9/2 \rightarrow 11/2$ transition for trapping. This configuration has since been successfully demonstrated by the rest of the team at Imperial.

3.6 Injection Lock Characterisation

Injection locking refers to the technique whereby a laser is forced to operate on a specific frequency by injecting light of the required frequency into the laser resonator [127, 128, 129]. The low-noise, low-power Toptica laser is injected into the high-power amplifier laser to get a high-power and low-noise resulting laser beam of the required frequency and narrow linewidth [130]. For the diode to be injected, it needs to be within certain cavity mode bounds to get a stable injection lock. There is a locking range defined by the injection field amplitude related to the peak diode cavity mode and the mode spacing. In this case, the peak cavity mode can be tuned by changing the current supplied to the diode by the diode controller or by changing the diode's temperature. Recent works on injection locking methods and characterisation are presented in [131, 132, 133].

In this section, we present the method used to achieve and characterise the injection lock in our laser system. Following the work presented in [134, 135], we create a lock-detection signal using a heterodyne beat between the seed laser and the injected diode. In this work, we use a double-passed AOM to tune the relative frequency of the injected diode, and we verify that the injected light can be used to create a cold red MOT.

Figure 3.13 indicates the full optical set-up used to achieve injection locking while 3.15 shows the electronics and control setup used for the characterisation of the injection lock.

The seed laser and the injected amplifier laser beam are coupled to a high-resolution HighFinesse WS8-10 wavemeter for frequency monitoring. The position of the seed beam is aligned geometrically to overlap with the counterpropagating amplifier beam, and the diode current is then tuned until injection is achieved, which is monitored by observing the frequency of the two beams on the wavemeter. The frequency of the injected beam is 680 MHz (frequency change due to the double pass AOM) less than that of the seed laser

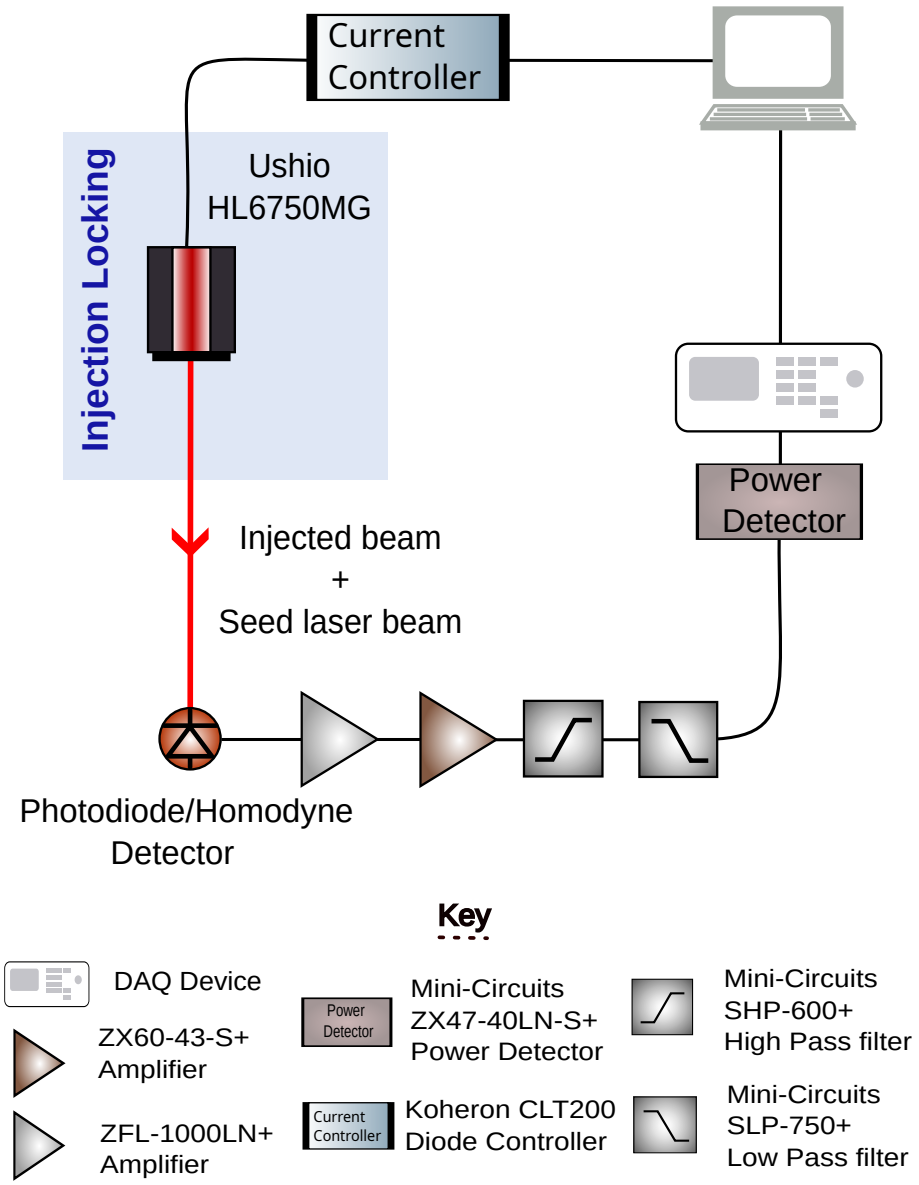

Figure 3.15: Setup for achieving amplifier injection and characterisation of the injection lock. The optical system used to achieve injection and get a beat note is shown in the blue box in Figure 3.13. The beat note is generated at the photodiode/heterodyne detector by interfering light from the injected amplifier diode and the seed laser. The rest of the system is used to control the diode current and temperature and perform current sweeps for the characterisation of the injection lock.

frequency.

To diagnose and optimise the injection more carefully, a photodiode is used to detect the

beat note created by combining the seed laser with the injected beam. The beat note can be displayed on a spectrum analyser for a first evaluation of the injection. An example of a beat note showing injection is shown in Figure 3.16a.

The injection lock can be characterised using the configuration shown in Figure 3.15. This configuration allows the heterodyne beat signal to be monitored on an oscilloscope and for the voltage of the power detector input signal to be measured as a function of time. A triangle waveform is generated which is used to sweep the current of the laser diode and produce a plot of the input power as a function of current as shown in Figure 3.16b. The range of currents over which the injection stays locked can therefore be found.

The diode was operated near 68 mA, producing a 42.5 mW beam directly at the diode output. From this, a total of 13.8 mW is available at the science chamber after the light propagates through all the distribution optics, AOMs and after fibre coupling. The amplifier diode stays injected over a window of $\sim$ 0.6 mA width. The lock is passively stable for periods of up to five days without automated intervention.

This method has some benefits over other methods found in the literature, e.g., a scanning cavity [129]. It can easily be assembled using an AOM, a photodiode, and a power detector as the main components to detect the heterodyne beat. Unlike the scanning cavity technique, the injection detection scheme is insensitive to large changes in the seed laser frequency, which is useful for the experiment as strontium isotopes are switched regularly. The use of a heterodyne signal for detection reduces sensitivity to optical alignment drift, allowing for high passive stability. In contrast with previously published heterodyne detection schemes [134], AOM1 in Figure 3.13 serves a dual purpose: we both create a beat note for lock detection, while also enabling fast, phase-coherent frequency modulation of the injected light without the losses that would be incurred by using an additional

AOM. The spectrum of the detected beat forms a clear diagnostic of injection quality that is useful while setting up initial parameters, and can be simply rectified to a DC signal using cheap, off-the-shelf components for use by an automated relocking algorithm.

3.7 Conclusion

In this chapter, I presented the experimental setup used for R&D purposes for the AION experiment at Imperial College London. This apparatus is used to cool atoms down and, at later stages of the experiment, perform experiments for spin squeezing. This chapter presents the laser and optical setup used to realise the narrowband red MOT, the results from which are described in the next chapter. The laser system is a simple and easy-to-assemble seed-amplifier injection-locked system, capable of generating $\sim 50\,\mathrm{mW}$ at 689 nm. We have demonstrated an easy-to-assemble method of characterising the injection lock by using an AOM to generate a beatnote by combining the seed and injected beam. The injection lock system was characterised using a beat note spectrum and by performing a current sweep and determining an injection lock window showing the range over which the amplifier laser stays injected. We have demonstrated that the amplifier diode stays injected over a range of $0.6\,\mathrm{mA}$.

3.7.1 My Contributions

The work presented in this chapter was carried out as part of the AION collaboration. I contributed to the commissioning of the cold atoms laboratory at Imperial College London in collaboration with the rest of the team. I led the experimental development of the compensation coils and the narrowband red magneto-optical trap (MOT) for ^{88}Sr atoms. This included assembling and aligning the optical setup, including injection locking, contributing to the implementation of the vacuum system and setting up the experiment, ac-

quiring data, and analysing results. Guidance was provided by Dr Charles Baynham and Dr Richard Hobson, with technical support from members of the Imperial AION group, including David Evans, Alice Josset, and Ludovico Iannizzotto-Venezze. Unless otherwise stated, the work presented in this chapter reflects my direct contributions.

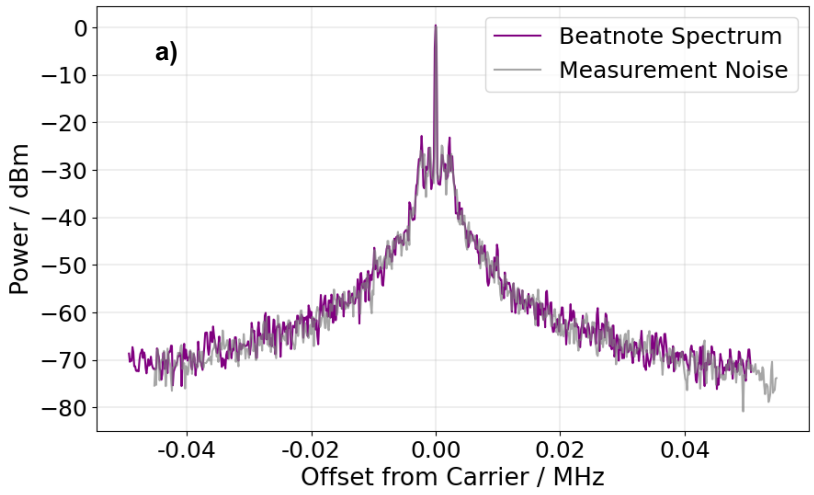

(a)

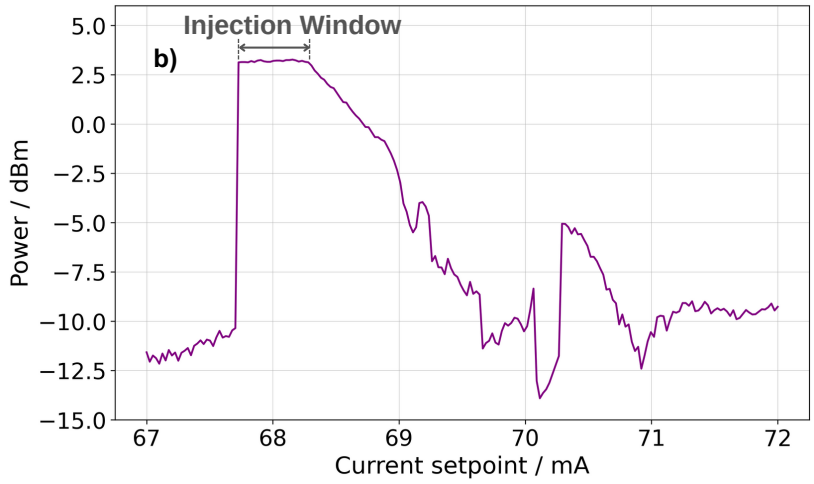

(b)

Figure 3.16: *(a)* The beat spectrum of the heterodyne signal measured by the photodiode using a bandwidth of 100 kHz. The beatnote spectrum is centered around the carrier frequency which is the difference in frequency between the seed and the injected beams. A background noise trace was also taken of an independent, high stability 680 MHz RF source revealing a source of measurement noise. The authors suspect phase noise within the spectrum analyser but note that the injected signal is indistinguishable from the ideal case within the precision of our instrument. *(b)* Injection characterization data as taken from the power detector. The injection signal exhibits strong hysteresis, as is common with injected systems. This scan was performed downwards in current over the setpoint ($\sim$ 68.0 mA). The flat region with the maximum power is the range of currents over which the diode is injected. This injection window is around 0.6 mA wide. This scanning trace was used to optically align the system and mode-match the injection beam to the diode's output by maximising the width of the injection window as changes were made.

Chapter 4

Getting Cold Atoms: Broadband and Narrowband Red MOT Experiments

This chapter presents the development and characterisation of the second stage of the cooling sequence, which employs broadband and narrowband magneto-optical traps (MOTs) on the Sr-88 atom's $^1S_0 \rightarrow {}^3P_1$ intercombination transition at 689 nm. The results and experimental details of the preceding 2D and 3D "blue" MOTs were presented in Ref. [1].

Following initial slowing and capture in a blue MOT operating on the broad 461 nm transition. We then move to a red MOT operating on the red 689 nm transition to cool atoms to a lower temperature. Atoms are transferred from a blue MOT to a modulated broadband red MOT to address a wide range of velocities. Subsequent compression and further cooling are achieved in a narrowband red MOT, enabling final temperatures below 1 μK.

Section 4.1 provides a concise theoretical background on laser cooling and magneto-

optical trapping relevant to the work described in this chapter. Section 4.2 outlines the experimental implementation of the two-stage red MOT, with the main focus being the broadband and narrowband red MOTs' cooling sequences. Section 4.3 describes the methodology used to extract atomic cloud temperatures via time-of-flight imaging, including the calibration procedures for both stages of the red MOT. The results of the temperature characterisation for both the broadband and narrowband MOTs are presented in Section 4.4.

Parts of this chapter are adapted from Ref. [2]. For the work presented in this chapter, the bosonic ^{88}Sr isotope was used since the isotope's natural abundance and lack of hyperfine structure make initial trapping easier. It should be noted however, that for interferometry, the ^{87}Sr isotope will be used and is now routine usage in the lab.

4.1 Laser Cooling and Trapping: Brief Introduction

The ability to control the motion of atoms by cooling and trapping them has revolutionised the field of atomic physics with many application across fields. Laser cooling exploits the momentum exchange between photons (lasers) and atoms to reduce the thermal motion of atoms, while magneto-optical traps (MOTs) combine this cooling force with spatial confinement using magnetic field gradients and polarised light. The success of laser cooling led to its pioneers, Steven Chu, Claude Cohen-Tannoudji and William Phillips, being awarded the 1997 Nobel prize in physics [136, 137, 138].

This section provides a brief introduction to laser cooling and magneto-optical traps (MOTs), which are used in the AION experiment to cool atoms to sub-microkelvin temperatures, which is the focus of this chapter. For a more detailed discussion of laser cooling and magneto-optical traps, the reader is referred to Refs. [139, 85, 140, 141, 142,

143, 144, 145], which provide comprehensive overviews of the underlying principles and techniques.

Similarly to matter, light has both momentum and energy. When a photon is absorbed by an atom, conservation of momentum requires that it also absorbs the photon's momentum, $\vec{p}_{\text{ph}} = \hbar\vec{k}$ Here $\hbar$ is the reduced Planck constant and $\vec{k}$ is the wave vector of the light, with magnitude $|\vec{k}| = 2\pi/\lambda$, where λ is the light's wavelength. We consider the case where an atom with two states (for simplicity) moves with velocity $\vec{v}$ and a laser light illuminates it with a k-vector $\vec{p}$ antiparallel to the $\vec{v}$. The atom absorbs the photon and gets excited, and the momentum of the atom changes from $m\vec{v}$ to $m\vec{v} - \hbar\vec{k}$. Since the atom and the light are moving in opposite directions, $\vec{k}$ and $\vec{v}$ are antiparallel, so the momentum and velocity of the atom are reduced.

When the atom decays spontaneously back to the ground state, it emits a photon and experiences a recoil due to the emitted photon's momentum. However, because spontaneous emission is distributed symmetrically in all directions, the momentum imparted by emitted photons averages to zero over many such events. As a result, through repeated absorption and spontaneous emission cycles, the atom's velocity decreases, effectively cooling the atom.

The magnitude of the scattering force that slows the atom down is the product of the photon momentum and the scattering rate.

The scattering rate, denoted as R_{scatt}, is given by

$$R_{\text{scatt}} = \frac{\Gamma}{2} \cdot \frac{\Omega^2/2}{\delta^2 + \Omega^2/2 + \Gamma^2/4} \tag{4.1}$$

which derives from $R_{\text{scatt}} = \Gamma\rho_{22}$ where ρ_{22} represents the population of the excited state. Here, Γ is the natural linewidth of the atomic transition, δ is the frequency detuning of the laser from resonance and Ω is the Rabi frequency [146, 139].

The frequency detuning $\delta = \omega - \omega_0 + kv$ represents the difference between the laser frequency ω and the atomic resonance frequency ω_0, incorporating the Doppler shift kv due to the motion of the atom. The saturation parameter $s_0 = I/I_{\text{sat}}$ and the Rabi frequency Ω are related by $I/I_{\text{sat}} = 2\Omega^2/\Gamma^2$. Here, I is the laser intensity and I_{sat} the saturation intensity. Each photon carries momentum $\hbar k$, leading to a scattering force on the atom given by

$$F_{scatt} = \hbar k \frac{\Gamma}{2} \frac{s_0}{1 + s_0 + 4\left(\frac{\delta}{\Gamma}\right)^2} \tag{4.2}$$

4.1.1 Optical Molasses

To cool all three axes of motion of the atoms coming out of the oven, three orthogonal pairs of counter-propagating laser beams are used. These beams originate from the same laser source and therefore have the same frequency. While this arrangement might seem ineffective at first since opposing beams exert equal and opposite forces, this is only true for atoms at rest, which is the condition laser cooling aims to create.

In the case that the atoms are in motion, the Doppler effect breaks this symmetry. The scattering force is velocity-dependent due to the Doppler effect, which plays a big role in laser cooling. An atom moving toward a laser beam sees the light blue-shifted in its rest frame, making red-detuned light appear closer to resonance. Conversely, an atom moving away from the beam (i.e. co-propagating with it) sees the light red-shifted, moving it further from resonance. As a result, the atom preferentially absorbs photons from the

beam opposing its motion, leading to a net radiation pressure force that slows it down.

The scattering force experienced by an atom as a function of its velocity v, due to two counter-propagating laser beams in a 1-D laser cooling setup is give by:

$$F_{net} = F_+ + F_- = \hbar k \cdot \frac{\Gamma}{2}\left[\frac{s_0}{1+s_0+4\left(\frac{(\Delta-kv)}{\Gamma}\right)^2} - \frac{s_0}{1+s_0+4\left(\frac{(\Delta+kv)}{\Gamma}\right)^2}\right] \tag{4.3}$$

where $\Delta = \omega - \omega_0$. A visual representation of the above expression, indicating the force vs. velocity curves for two counterpropagating laser beams, is depicted in Figure 4.1.

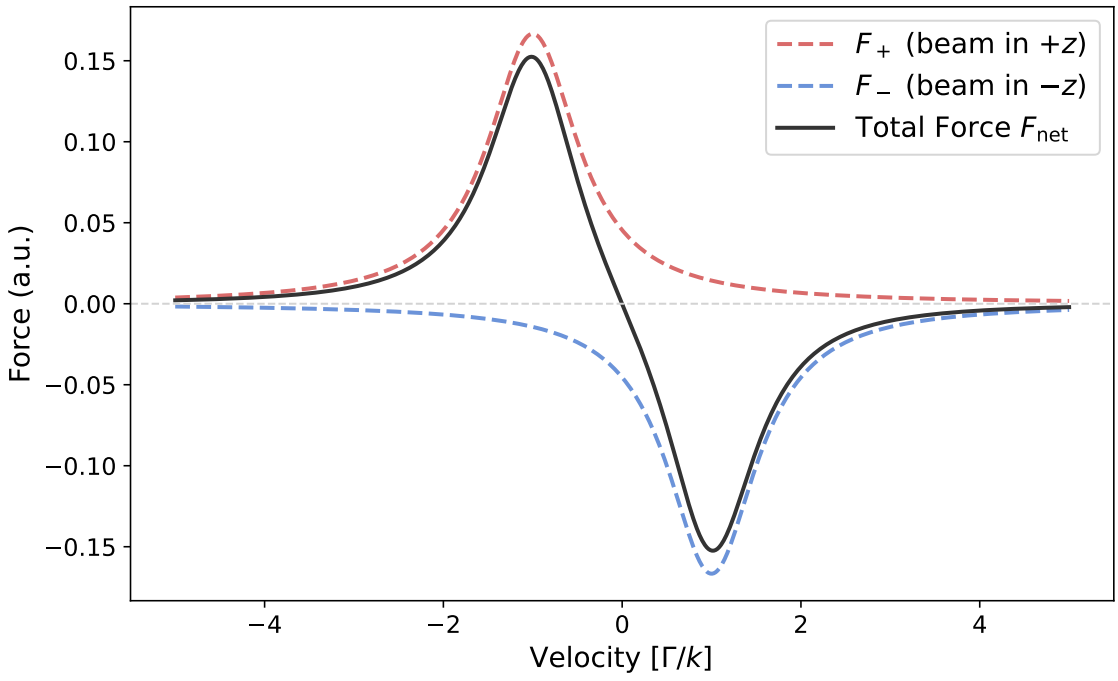

Figure 4.1: Scattering force as a function of atomic velocity for two counter-propagating red-detuned laser beams. The red and blue dashed curves represent the velocity-dependent scattering forces from beams propagating in the $+z$ and $-z$ directions, respectively. Due to the Doppler shift, atoms absorb more photons from the beam opposing their motion, resulting in a net cooling force (black curve). This force is approximately linear near zero velocity and is responsible for the damping effect central to Doppler cooling.

The Doppler cooling limit determines the lowest temperature achievable by laser cooling using purely Doppler-based scattering forces. This limit occurs because of the balance between the cooling effect of velocity-dependent photon absorption and the heating resulting from random recoils from spontaneous emission. The limit depends on the natural linewidth, Γ, of the cooling transition used and is given by [88, 147],

$$T_D = \frac{\hbar\Gamma}{2k_B} \tag{4.4}$$

Narrower linewidth transitions give rise to lower Doppler temperature limits. The broader transition at 461 nm has a Doppler limit of around 770 µK while the intercombination narrow line transition in strontium at 689 nm has a Doppler limit of around 0.18 µK. Going below that limit can be achieved using sub-Doppler cooling techniques such as Sisyphus cooling and evaporative cooling [145, 138].

4.1.2 Magneto Optical Traps

The optical molasses technique reduces the thermal motion of atoms through Doppler cooling, resulting in a cloud of slower-moving atoms near the intersection of three orthogonal pairs of counter-propagating laser beams. However, because optical molasses does not provide spatial confinement, the atoms eventually diffuse away. This limitation can be overcome by using a magneto-optical trap (MOT) [148, 149], which combines a magnetic field gradient with carefully chosen laser beam polarisations to localise and trap the atoms near the centre of the setup. A MOT is therefore achieved using polarised laser beams in combination with a pair of coils carrying currents in opposite directions so that they generate a quadrupole magnetic field. A schematic diagram of a MOT set-up is depicted in Figure 4.2. The magnetic field does not confine the atoms by itself. In the MOT,

the quadrupole magnetic field creates a position-dependent imbalance in the scattering forces from the laser beams, resulting in a net radiation force that effectively confines the atoms in space. The basic concept of MOT is shown in Figure 4.2 (a), using a simple transition from $J = 0$ to $J = 1$ as an example.

At the centre of the magneto-optical trap (MOT), the magnetic field produced by the anti-Helmholtz coil pair cancels out, resulting in $B = 0$. Away from this point of zero field exists a uniform field gradient that causes perturbations in the atomic energy levels via the Zeeman effect. For a $J = 0 \rightarrow J = 1$ transition, the excited state splits into three sublevels with $M_J = -1, 0, +1$ whose energies vary linearly with position along the z-axis (Figure 4.2 (a).

The counter-propagating laser beams are circularly polarised as shown in Figure 4.2 (b). Their frequency is tuned slightly below the atomic resonance frequency of the transition used. The Zeeman shift leads to an imbalance in the radiation force through the following mechanism. In the one-dimensional example where an atom moves away from the centre of the trap along the positive z-axis, the $\Delta M_J = -1$ transition frequency is closer to matching the laser frequency. This happens because the laser is intentionally tuned slightly below the atom's natural resonance frequency (red-detuned) when $B = 0$, triggering absorption, which slows the atoms down. Due to the polarisation of the laser beams, the atom is more likely to absorb photons from the beam propagating in the negative z-direction, which is circularly polarised to drive the σ^- transition [148, 139]. This results in a momentum kick in the negative z-direction, producing a scattering force that pushes the atom toward the centre of the trap. A similar process occurs when the atom moves in the negative z-direction, where absorption from the beam travelling in the positive z-direction is favoured and pushes the atom back to the centre.

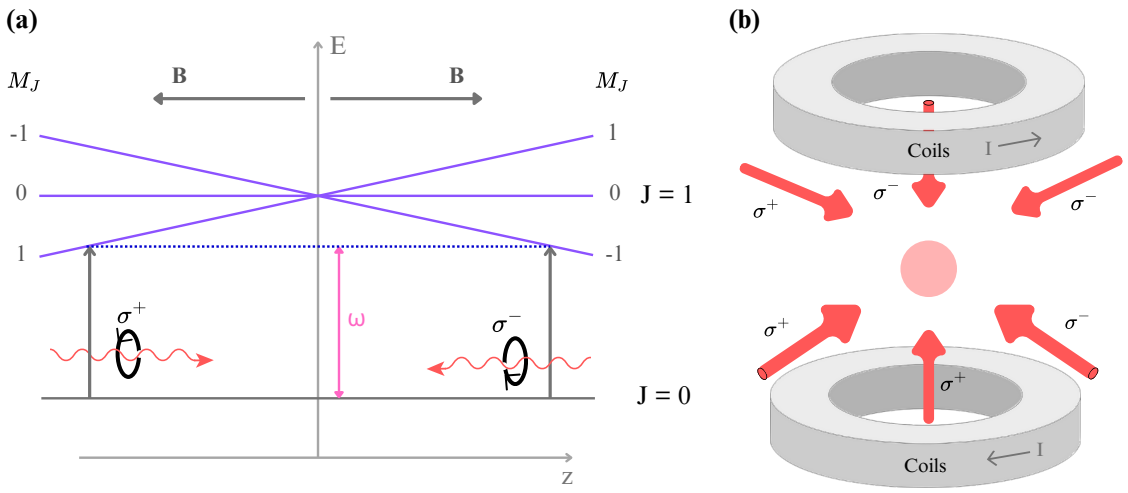

Figure 4.2: Illustration of the Magneto-Optical Trap (MOT) principle. (a) Zeeman splitting of the $J = 1$ sublevels ($M_J = 0, \pm 1$) in a quadrupole magnetic field, shown for a $J = 0 \rightarrow J = 1$ transition. The energy levels vary linearly with position along the z-axis. The horizontal dashed line indicates the laser frequency (ω) in the atom's rest frame. (b) Schematic of the MOT setup with counter-propagating circularly polarized laser beams and a pair of anti-Helmholtz coils producing a magnetic field gradient to enable three-dimensional trapping.

4.2 Red MOT Sequence

The previous chapter presented the experimental setup details and hardware used for the red MOTs. This section focuses on the experimental sequence used to achieve the red broadband and narrowband MOTs and characterise the temperature of the atomic clouds and the first results from these two steps of the cooling sequence in the AION experiment.

4.2.1 The 2D and 3D Blue MOT

The atom cooling sequence begins with a two-stage blue MOT process operating on the $^1S_0$ to $^1P_1$ transition in ^{88}Sr at 461 nm. The blue MOT cools the hot beam of atoms as they come out of the oven down to a few mK.

First, a 2D blue MOT in chamber 1 creates a pre-cooled atomic beam. To achieve this, two

circularly polarized 45 mm beams are used that are retro-reflected to form four trapping beams. Light that is detuned by -2Γ from the ^{88}Sr $^1S_0$ to $^1P_1$ transition is used in this stage. The magnetic fields are provided by the permanent magnets. A near-resonant push beam directs these pre-cooled atoms through a 3 mm differential pumping aperture into chamber 2.

The atoms are then captured in a 3D blue MOT in chamber 2 using three orthogonal beams (15 mm diameter) that are retro-reflected, creating six trapping beams that are detuned from the ^{88}Sr $^1S_0$ to $^1P_1$ transition by -2Γ. The laser beams perpendicular to the atomic beam trajectory feature greater intensity compared to the beam along the MOT coil axis, enhancing the system's ability to efficiently capture incoming atoms moving predominantly in the radial direction. Quadrupole coils operating at 100 A generate a field gradient of 4.9 mT cm^{-1}. Repumping lasers at 679 nm and 707 nm return atoms that decay to the $^3P_0$ and $^3P_2$ states to the coding cycle.

The 3D blue MOT is loaded by applying Doppler-cooling light at 461 nm and repumping light at 679 nm and 707 nm, addressing the $^3P_0$ – $^3S_1$ and $^3P_2$ – $^3S_1$ transitions respectively. More details about the results from this step are presented in Ref. [1].

The following subsections describe the experimental details and results from the subsequent two cooling steps, namely, the broadband and the narrowband red MOTs that operate on the 689 nm transition. Sections 4.2.2 and4.2.3 present the experimental sequence of the two red MOTs. Section 4.3 describes the method used to analyse the results and take temperature measurements of the atomic cloud after the red broadband MOT stage and the narrowband red MOT stage. Section 4.4 presents the results of the temperature measurements.

4.2.2 Broadband Red MOT

The laser and magnetic field cooling sequence used both to load and to characterise the temperature of the atom cloud trapped in a red broadband MOT is presented in Figure 4.3.

The broadband red MOT stage is performed to increase the efficiency of atom transfer from the blue to red MOT cooling stages. This is achieved by applying saw-tooth modulation to the red light's frequency to effectively broaden the narrow transition and address a wider range of velocity classes in the atomic cloud. We apply a positive ramp from detuning $\delta = -6\,\text{MHz}$ to $\delta = 0\,\text{MHz}$, repeated at 30 kHz.

For this stage of cooling, we apply three circularly polarised, orthogonal, retro-reflected beams, each with a 9 mm $1/e^2$ radius and 2.4 $\text{mW}\,\text{cm}^{-2}$ peak intensity. The beams retroreflect through an achromatic quarter-waveplate suitable for both blue and red wavelengths. One beam propagates coaxially with the paired anti-Helmholtz coils that create the MOT field gradient [1, §3.2.3]. The other two propagate at 45° angles to gravity. This sequence was used to produce atomic clouds of temperature in the order of 10 µK. The results and presented in Section 4.4.1.

4.2.3 Narrowband Red MOT

The next step in the cooling procedure in the AION project is a narrowband red MOT. The experimental sequence used to achieve the narrowband red MOT is presented in Figure 4.4, which indicates the laser and magnetic field cooling sequence used both to load and to characterise the temperature of the atom cloud trapped in a red narrowband MOT.

After initial capture in the broadband MOT, we transition to "capture" and "compression" phases in which the 689 nm light is no longer frequency modulated and the beam detuning, beam intensities and field gradient are linearly ramped as shown in Figure 4.4.

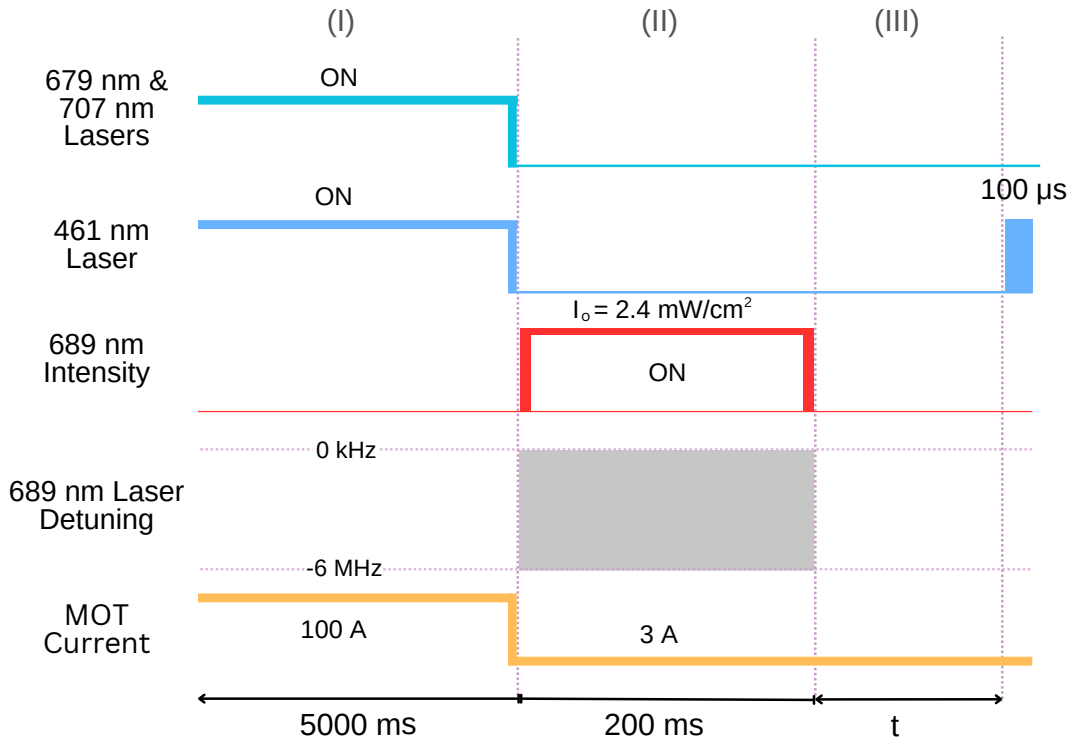

Figure 4.3: Cooling sequence timing diagram for the broadband red MOT. In stage (I) The 3D blue MOT is loaded for 5000 ms while the quadrupole coils are driven with a current of 100 A, which gives a magnetic field gradient of approximately 3.9 mT cm^{-1} (calibrated using measurements taken on identical coils in Ref. [1, §3.2.3]). The 461 nm laser and therefore the blue MOT is then turned off and the 689 nm laser is turned on (with an intensity of $I_o = 2.4$ mW cm^{-2}) transferring the atoms to the red broadband MOT over 200 ms (stage II). The cloud is led to expand for a variable time (t) (stage III). The detection of Sr atoms for monitoring the dynamics of the red MOT is done using the 461 nm transition. A probe beam interacts with the atoms and the resulting fluorescence is detected via CMOS cameras (BFS-PGE-50S5M-C PoE GigE Blackfly S Monochrome camera). The fluorescence pulse and the camera exposure are on for 100 µs. The setup includes two cameras, imaging the atom cloud in the horizontal x-y plane and the plane along gravity (x-z plane).

These "narrowband" stages result in a cooler and more compressed cloud (sub-millimeter scale) suitable for later loading into a crossed optical dipole trap. The sequence parameters shown in Figure 4.4 (broadband scan rate, broadband modulation depth, phase duration, starting and ending field gradient, beam intensity and frequency detuning) were individually manually optimized through iterated 1-dimensional scans. We found that the

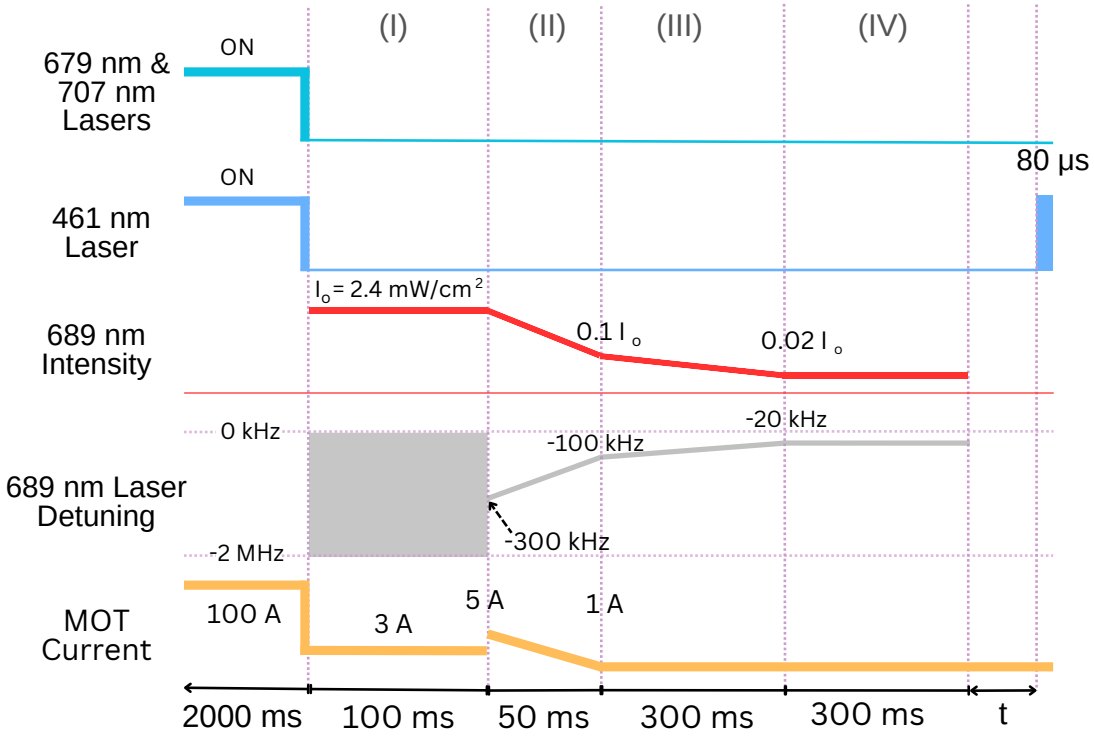

Figure 4.4: Cooling sequence timing diagram. The 3D blue MOT is loaded for 2000 ms while the quadrupole coils are driven with a current of 100 A, which gives a magnetic field gradient of approximately 3.9 mT cm^{-1} (calibrated using measurements taken on identical coils in Ref. [1, §3.2.3]). The 461 nm laser and therefore the blue MOT is then turned off and the 689 nm laser is turned on (with initial intensity I_o = 2.4 mW cm^{-2}) transferring the atoms to the red broadband MOT over 100 ms (stage I). The current is reduced to 3 A over this step while the frequency is modulated to broaden the transition. In stage (II), the frequency modulation is turned off and atoms are trapped in a single-frequency MOT. The cloud is compressed by decreasing the detuning and intensity of the beam as well as the MOT current. The atoms are then held in the narrowband red MOT for 300 ms (stage (IV)). The cloud is led to expand for a variable time (t). The detection of Sr atoms for monitoring the dynamics of the red MOT is done using the 461 nm transition. A probe beam interacts with the atoms and the resulting fluorescence is detected via CMOS cameras (BFS-PGE-50S5M-C PoE GigE Blackfly S Monochrome camera). The fluorescence pulse and the camera exposure are on for 80 µs. The setup includes two cameras, imaging the atom cloud in the horizontal x-y plane and the plane along gravity (x-z plane).

MOT loading efficiency was approximately insensitive to changes of up to 50 % around the reported values (with the exception of the ramp parameters of the broadband phase), however our manual search did not account for parameter correlations. With more thor-

ough searches of the sequence parameter space, we anticipate improvements in both atom number and ultimate temperature.

This process enables the cooling of atoms to temperatures below sub-μK. The results from this stage are presented in Section 4.4.2.

The next section provides a detailed explanation of the method used to characterize the temperatures of atomic clouds in both broadband and narrowband red MOTs.

4.3 Temperature Measurement Method

The relationship between the temperature T and the $1/e^2$ radius $r(t)$ of the cloud is given by [150]

$$T = \frac{m}{4k_B t^2}\left[r(t)^2 - r(0)^2\right] \quad , \tag{4.5}$$

where m is the mass of a strontium atom and k_B is Boltzmann's constant. $r(0)$ is the radius of the cloud at time $t = 0$ before the cloud starts expanding and, with T, is a free parameter of the fit.

Time-of-flight (TOF) fluorescence imaging is used to determine the temperature of the atomic cloud. We image in a plane parallel to gravity so that the known acceleration of the cloud under free-fall can be used to calibrate the size of one pixel in the image plane (see Figure 4.10). For the TOF images, the 689 nm light is turned off then the atoms are allowed to freely expand for variable amounts of time, t between 0 ms to 35 ms and 0 ms to 40 ms for the broadband (BB) and narrowband (NB) MOT measurements respectively taking 20 (BB) 30 (NB) points (pictures) at various times within this range. This process is repeated 20 (for the BB MOT) and 30 (for the NB MOT) times. Images are taken by pulsing the 461 nm MOT beams for 80 µs synchronously with a gating trigger

pulse to our camera, optically filtered by an FBH460-10 band-pass filter centered around 460 nm. Example images from the narrowband and broadband red MOT results are shown in Figures 4.5 and 4.6, respectively.

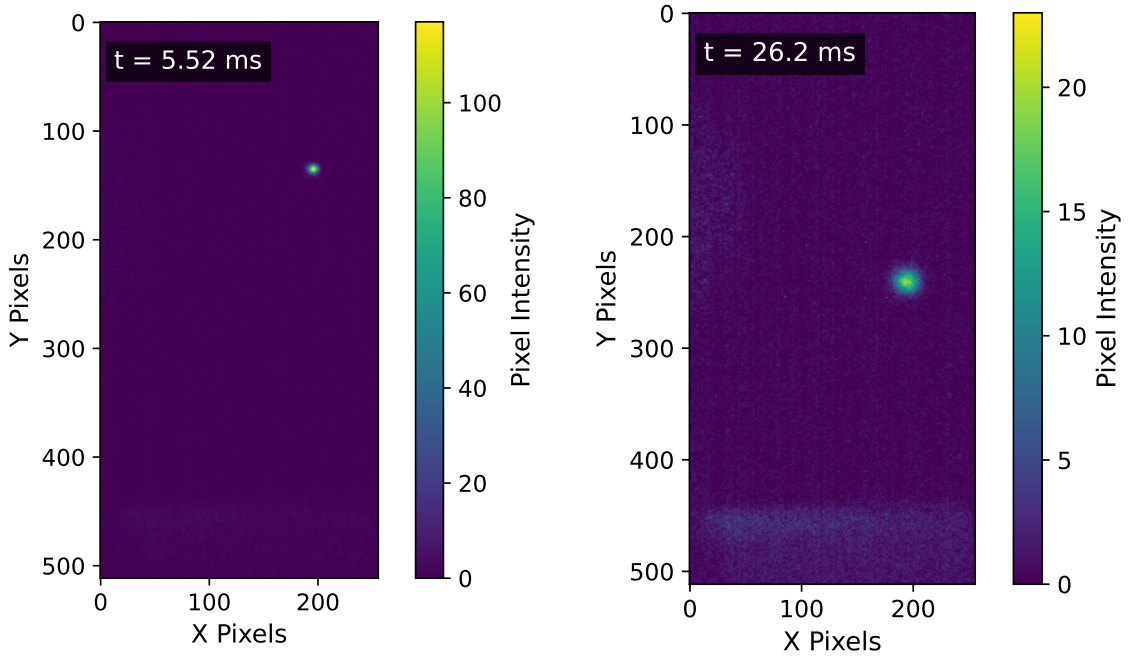

Figure 4.5: Example 2D images from the narrowband red MOT TOF measurements. The picture on the left was taken at t = 5.5 ms and the picture on the right at t = 26 ms after the cloud is released to expand in a vacuum. The images show the pixel intensity before normalisation. The reflection from the cavity can also be seen at the bottom of the right image.

A 2D Gaussian fit was then applied to the TOF images to determine the cloud widths and positions at variable expansion times for each repeat dataset and therefore determine the temperature of the cloud in the red MOTs. The process is outlined below.

4.3.1 Extracting the Atomic Cloud Widths from the TOF Images

The general equation for a 2D Gaussian function with rotation is given by:

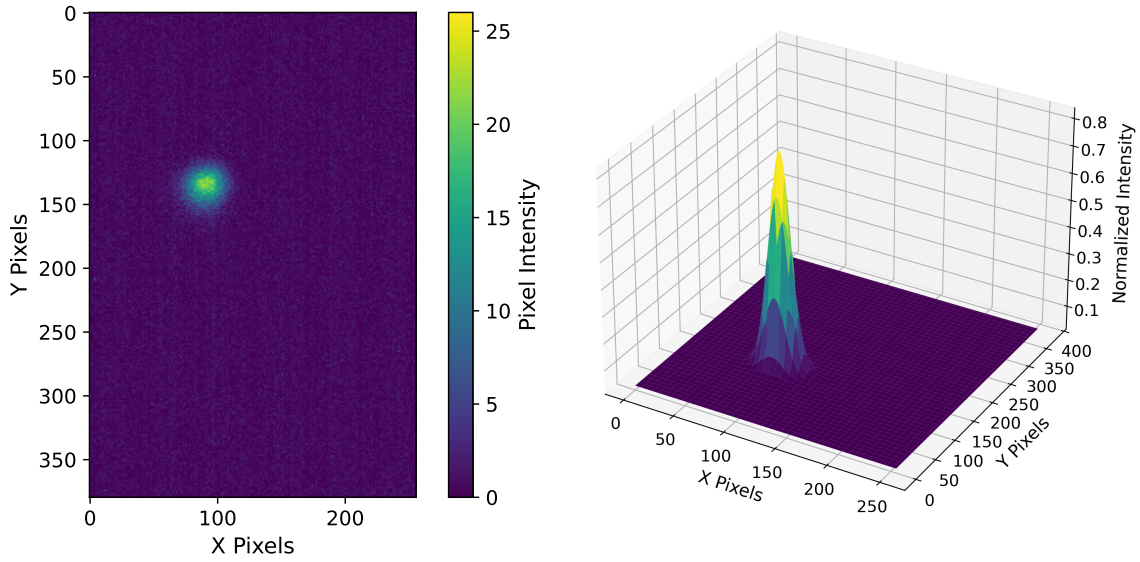

(a) 2D Image

(b) 3D Gaussian Fit

Figure 4.6: Example image from the broadband red MOT time of flight measurement. This picture was taken at ≈ 5.5 ms after the cloud is released to expand. The 2D image is shown on the left and the 3D Gaussian fit is displayed on the right. The 2D image shows the pixel intensity before scaling whereas the 3D Gaussian fit plot shows the normalised pixel intensity.

$$g(x,y) = \text{offset} + A\exp\left(-\left[a(x-x_0)^2 + 2b(x-x_0)(y-y_0) + c(y-y_0)^2\right]\right), \tag{4.6}$$

where:

$$a = \frac{\cos^2\theta}{2\sigma_x^2} + \frac{\sin^2\theta}{2\sigma_y^2}, \quad b = -\frac{\sin(2\theta)}{4\sigma_x^2} + \frac{\sin(2\theta)}{4\sigma_y^2}, \quad c = \frac{\sin^2\theta}{2\sigma_x^2} + \frac{\cos^2\theta}{2\sigma_y^2}.$$

Here:

- A is the amplitude of the Gaussian.

- (x_0, y_0) are the coordinates of the center of the Gaussian in the 2D image.
- σ_x and σ_y are the standard deviations along the x- and y-axes, respectively.
- θ is the rotation angle of the Gaussian, measured counterclockwise from the positive x-axis. The rotation angle of the Gaussian was set to zero as it was assumed that the camera was aligned well.

In the narrowband red MOT pictures, there was light reflected from the bottom of the cavity (see Figure 4.5 which appears as noise and is picked up when the pictures were fitted. Therefore, the images were cropped before the analysis was carried out to specify the rectangular region of interest (ROI) in each image and avoid fitting the wrong region. The broadband red MOT pictures did not have such reflections so they were directly fitted without cropping them. The pixel coordinates of the images were then used to create 2D coordinate grids (x and y) for fitting.

The gaussian function specified in Equation 4.6 was fitted to each of the images of the TOF measurements. Before the fitting, each image was normalized by dividing all pixel values by the maximum value of the given image to scale between 0 and 1 to ensure consistent scaling across images and improve the fitting process. The normalisation did not have an effect on the fitting of the broadband red MOT pictures but it significantly improved the fitting of the narrowband red MOT pictures, This might be due to the fact that the narrowband red MOT pictures had higher background noise and that the maximum pixel intensity is higher than that in the broadband red MOT pictures.

To fit the 2D Gaussian model to the images, the `curve_fit` function from the `scipy.optimise` library was used to optimise the parameters of the Gaussian function defined in Equation 4.6.

To ensure successful optimisation and fitting initial guesses were determined as follows:

- **Amplitude** (A): the maximum intensity of the picture.
- **Center** (x_0, y_0): The middle of the picture.
- **Standard Deviations** (σ_x, σ_y): The standard deviations of the x- and y-coordinate grids in the image.
- **Offset**: The minimum intensity value in the images.

Optimisation was then performed using the `curve_fit` function on the flattened coordinate grids (x,y) and the corresponding pixel intensity values of the pictures. Using the initial guesses and bounds, the optimised parameters ($A, x_0, y_0, \sigma_x, \sigma_y$, offset) were then calculated. The covariance matrix was also produced, from which the uncertainties in the fitted parameters was calculated as the square root of the diagonal elements of the matrix. The $1/e^2$ radii of the atomic cloud in x and y are also calculated as: $r_x = 2\sigma_x$ and $r_y = 2\sigma_y$.

For each time point, the mean position in x and y, as well as r_x and r_y, was calculated. For the narrowband red MOT calculations, only the first 16 points (0 ms to 20.7 ms) from each repeat were used, as after that, the Gaussian fitting is not as accurate on some pictures. This is mainly because the cloud expands too much, making it harder to distinguish between the background and the pixels that belong to the atomic cloud. The errors of these quantities were also calculated as the standard error of the mean (SEM) ($\sigma/\sqrt{n}$).

To determine the pixel calibration constant to convert the pixels into distance moved by the atomic cloud falling freely under gravity, the following kinematic equation is used:

$$y = y_0 + \frac{1}{2} g t^2 \cdot k_{\text{pixel}}$$

Where y(t) is the position of the object at time t, y_0 is the initial position of the cloud, k_{pixel} is the pixel calibration constant and g = 9.81 m/s^2. This equation assumes that the initial velocity is zero (at time t = 0) therefore the $v_0 t$ term is neglected.

The calibration constant is determined by fitting the model in the equation 4.3.1 to the experimental data (y-position and time) using the `curve_fit` function. The standard error of the mean in y is then used as the sigma parameter in the fit, to weight the residuals during the least squares optimisation.

The resolution of the pictures in m/pixel was calculated as the inverse of the calibration constant and the uncertainty of the resolution was calculated as the standard error of the pixel calibration constant obtained from the covariance matrix divided by the square of the calibration constant value.

Using this technique, we determine the camera resolution to be (32.9 ± 0.1) µm/pixel and (30.9 ± 0.1) µm/pixel for the pictures taken for the broadband and narrowband red MOT respectively. Figures 4.7 and 4.8 show plots of the vertical position (y-axis) against the expansion time, along with the fitted model used to determine the image resolution.

The atomic cloud radii were converted from pixels to µm, and Equation 4.5 was used to fit the horizontal and vertical radii as a function of expansion time to determine the temperature of the atomic cloud in the MOT in the two dimensions. The uncertainty from the calibration constant was also added to the radii uncertainty in quadrature. The best-fit values for the temperature and the initial radius r_0 in both dimensions were obtained using the `curve_fit` optimization method. The error on the temperature in the two dimensions is calculated as the square root of the diagonal element of the covariance matrix of the fit for the given quantities.

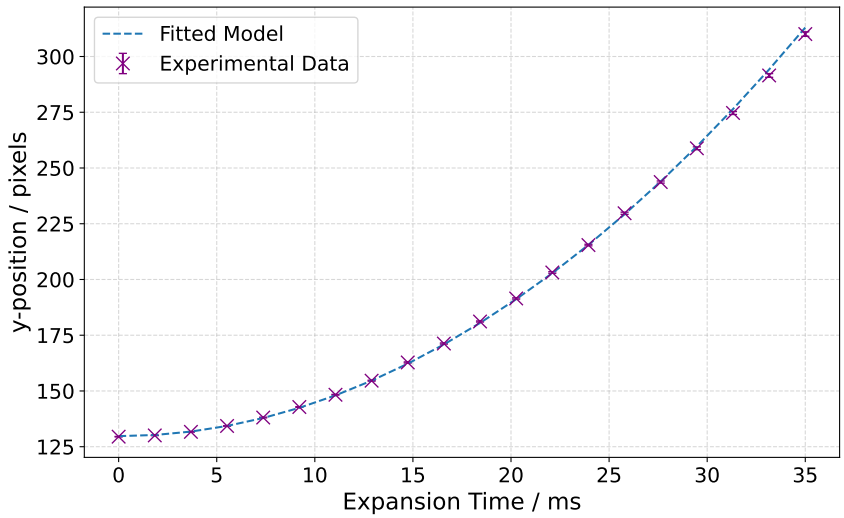

Figure 4.7: Plot of the vertical position (y-position) of the atom cloud as a function of expansion time for the broadband red MOT dataset. The data points represent the mean y-positions obtained from Gaussian fits to the images, with error bars indicating the standard error of the mean. The fitted model, shown as a dashed curve, was used to determine the image resolution of (32.9 ± 0.1) µm/pixel.

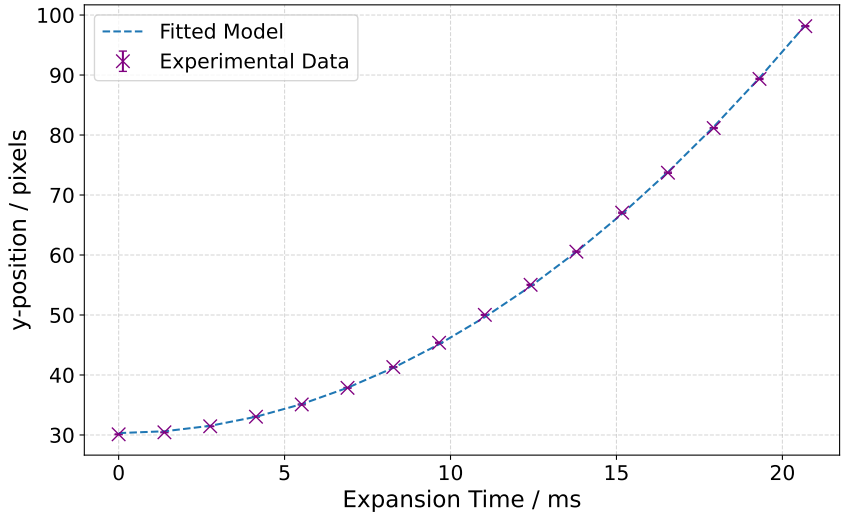

Figure 4.8: Plot of the vertical position (y-position) of the atom cloud as a function of expansion time for the narrowband red MOT dataset. The data points represent the mean y-positions obtained from Gaussian fits to the images, with error bars indicating the standard error of the mean. The fitted model, shown as a dashed curve, was used to determine the image resolution of (30.9 ± 0.1) µm/pixel).

4.4 Red MOT Temperature Results

The temperature results of the atomic cloud in the broadband and narrow-band red MOTs are presented in this section. The experimental sequences described in Section 4.2 were implemented for these results.

4.4.1 Broadband Red MOT

The results for the temperature measured in the broadband red MOT are presented in this section. Figure 4.9 shows an example of three TOF measurements, as well as the result of fitting Equation 4.5 to the measured cloud widths in the horizontal and vertical (i.e. along gravity) directions. We find horizontal and vertical temperatures in the final red MOT stage of the broadband (13.14 ± 1.09) µK and (13.12 ± 1.31) µK, respectively. The $1/e^2$ widths of the unexpanded cloud are (997 ± 6) µm and (1038 ± 9) µm in the horizontal and vertical directions respectively.

4.4.2 Narrowband Red MOT

The results of fitting Equation 4.5 to the measured cloud widths of the narrowband red MOT TOF measurements in the horizontal and vertical (i.e. along gravity) directions are shown in Figure 4.10. We find horizontal and vertical temperatures in the final narrow-band red MOT stage of (812 ± 4) nK and (778 ± 14) nK respectively. The $1/e^2$ widths of the unexpanded cloud are (319 ± 1) µm and (261 ± 1) µm in the horizontal and vertical directions respectively.

The results from the red MOTs indicate how we were able to go from a few milli-Kelvin temperatures (in the blue MOT) to $\approx 10\,\mu$K in the broadband red MOT and then to sub-µK in the narrowband red MOT. The Doppler limit limits the temperature in the red MOT to

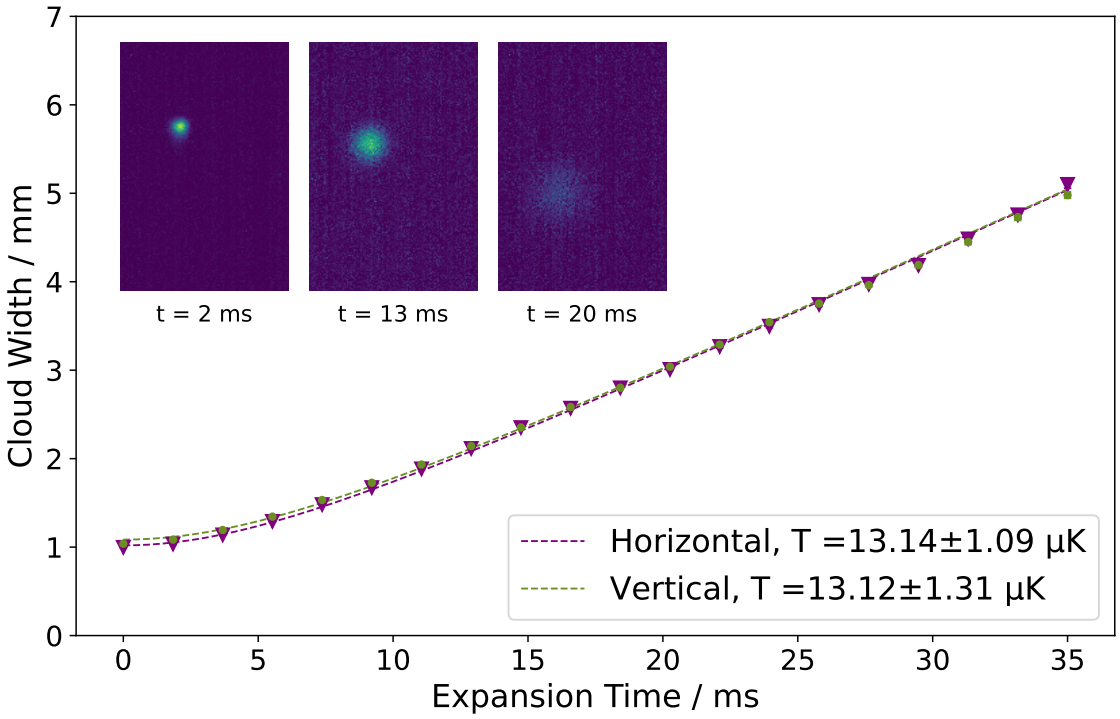

Figure 4.9: Time-of-flight measurements of the atomic cloud taken after the atoms are released from the broadband red MOT stage. Each datapoint consists of 20 randomised repeats whose standard error is taken as the statistical uncertainty. *(inset)* Sample raw images of the expanding atomic cloud.

0.18 μK, and to go colder than that, other techniques are to be employed i.e. evaporation in a dipole trap, which is the next step in the cooling sequence.

4.5 Conclusion

This chapter presents the first results of a narrowband red MOT operated on ^{88}Sr atoms at Imperial College London. An atomic cloud was cooled down to a temperature of (812 ± 4) nK in a narrowband red MOT. The atom cloud temperature is comparable to those obtained in previous works [151, 82], which report a temperature of $\sim 1\,\mu$K. This temperature is low enough to efficiently load an optical dipole trap - the next step towards differential atom interferometry. This is an important milestone for the AION collabora-

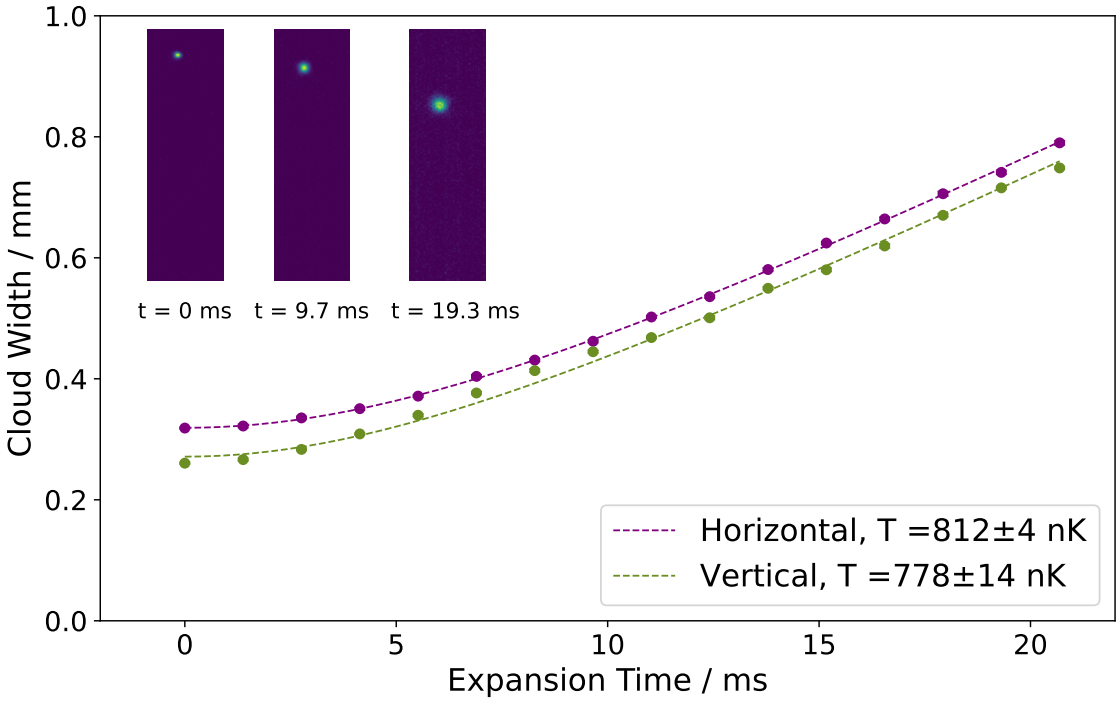

Figure 4.10: Time-of-flight measurements of the atomic cloud taken after the atoms are released from the final red MOT stage. Each datapoint consists of 30 randomised repeats whose standard error is taken as the statistical uncertainty. *(inset)* Sample raw images of the expanding atomic cloud.

tion as we move from tabletop experiments to the realisation of a long baseline detector used to detect gravitational waves, ultra-light dark matter and beyond.

Since these results were obtained, the experiment has progressed. The atoms were successfully loaded into a dipole trap, and the cooling sequence was also carried out using 87Sr isotope, which will be used in the actual AION detector in the future. The AION team at Imperial has built a prototype of a single-photon long-baseline atom interferometer using the 87Sr clock transition. The prototype detector aimed for searching for dark matter and gravitational waves can operate at the Standard Quantum Limit (SQL) with the only noise source present in the measurement being the expected atom shot noise. These results have been published on arXiv (see Ref. [152]).

4.5.1 My Contributions

I led the analysis of the red MOT results for ^{88}Sr atoms. This included the development of the data analysis methodology, implementation of the analysis code, and interpretation of the results. The raw data used in this analysis were acquired by other members of the Imperial AION team. Parts of this chapter are based on work published in [2], the writing of which I led as first author and in collaboration with the rest of the team.

Chapter 5

Prospects for detecting new dark physics with the next generation of atomic clocks

The world's most precise clock to date can reach relative uncertainties of 10^{-19} [153], a level of precision which would lose less than a second over the age of the universe. This level of precision opens up new avenues for testing fundamental physics theories by searching for variations in Nature's constants. In many theories beyond the Standard Model, "fundamental constants" such as the proton-to-electron mass ratio (μ) and the fine structure constant (α) are not fixed but can vary dynamically over time [154, 155, 156, 7]. This behavior is exhibited in a wide variety of dark matter, dark energy, and modified gravity theories. Atomic, molecular and ion clock transition frequencies depend on those fundamental constants and are therefore sensitive to their variations [157]. By comparing the frequencies of two different atomic/molecular transitions, we obtain a unit-

less observable that is sensitive to fundamental constant variations [158, 159]; the level of constraint produced by such a comparison depends on both the precision of the clocks involved and their intrinsic sensitivity to the fundamental constants under question [160].

Earlier studies of temporal variations of fundamental constants searched for linear drifts in the atomic clock frequency ratios between two clock species [161, 158, 160, 162]. Drift rates were extracted from linear fits to the data, with μ and α dependence derived through computational calculations of atomic structure. More recently, frequency measurements of atomic clocks have also been used to search for oscillatory fundamental constant variations caused by hypothetical gravitational potential couplings to μ and α by investigating the possibility of annual sinusoidal variations caused by the varying gravitational potential as the Earth orbits the Sun [163]. Previous studies that have searched for such variations in μ[1] have used neutral strontium vs. caesium-fountain [165], hydrogen maser vs. caesium [166], and ytterbium ion vs. caesium [167] comparisons. These studies have searched for violations of general relativistic local position invariance with no such variations observed to date, resulting in some of the strictest constraints on fundamental theories currently known.

In parallel, over the past several decades, there have been enormous advancements in the development of different types of clocks, including atomic, molecular, and ion clocks. There are over 450 atomic clocks in over 80 national laboratories worldwide, contributing to International Atomic Time (TAI) alone [168]. It is estimated that there are thousands of atomic clocks worldwide in telecommunication networks, GPS satellites, and research institutions and universities. The most precise and accurate atomic clock has recently recorded a systematic uncertainty of 8×10^{-19} [153]. Dedicated efforts to build networks of clocks with unprecedented sensitivity to temporal variations of the fundamental con-

[1] See [164] for a similar search for α variations using atomic dysprosium.

stants are also ongoing [169, 170]. The pace of progress in both theoretical fundamental physics and optical frequency metrology motivates a coordinated approach that integrates theory and experiment.

The purpose of this work is threefold. First, we overview wide classes of new physics theories focusing on those with specific predictions that atomic clocks can measure. Second, we carry out a preliminary search for those signals by compiling existing publicly available data from the BIPM Circular T database [171]. Third, we introduce a tool to apply statistical methods and generate constraints based on the characteristics of the clocks in question that can be used to test the sensitivity of clocks to fundamental physics theories, specifically a wide variety of modified gravity, dark energy and dark matter theories. This tool can also be used to forecast the degree to which future atomic clock advancements can result in stronger bounds on fundamental physics, and we use it to explore several such possibilities in this work.

This chapter is based on the paper "Prospects for detecting new dark physics with the next generation of atomic clocks" which has been accepted for publication in Physical Review D [3], and is structured as follows.

Section 5.1 gives an overview of atomic clocks and their performance. Section 5.2 provides an overview of the fundamental theories that we test. Secs. 5.3 and 5.4present an illustrative analysis using publicly available data from optical atomic clocks to produce constraints on those theories and to provide forecasts on state-of-the-art/future clock experiments and projections for their testability with atomic clocks. Section 5.5 presents a publicly available tool that can be used to derive constraints using the characteristics of atomic clocks as input. We conclude in Sec. 5.7.

In addition to the main content of the paper, it includes a study on the effect of gaps on

the recovery of a sinusoidal signal with a period of one year. This analysis and its results are presented in Section 5.6.

Conventions: Throughout this work, we use natural units in which $c = \hbar = 1$, the mostly-plus metric convention, and we define the reduced Planck mass in the usual way as $M_{\rm Pl} = (8\pi G)^{-1/2} \approx 2 \times 10^{18}$ GeV.

5.1 Atomic Clocks

This section provides an overview of what atomic clocks and, therefore, frequency standards are and is based on References [38] [172]. An overview of the noise sources and errors in atomic clocks is also given to introduce the errors considered when searching for fundamental physics signals.

Frequency standards require a system with a well-defined reference frequency. This system can provide a frequency reference that is stable and a way to define a unit of time. Time intervals are defined by counting cycles of a frequency generator.

Atoms are an ideal frequency standard as atoms from the same species are identical. The natural oscillation frequency of an atom can therefore be used to create an atomic frequency standard. To make an atomic frequency standard, a sample of atoms or molecules and a way to produce an oscillatory signal that is in resonance with the natural oscillations (that of a particular transition) of the atoms are required. An atomic clock is therefore made by counting the cycles of the oscillatory signal produced (e.g. from the laser). Figure 5.1 illustrates the principle of operation of a clock.

In an atomic clock, a source of radiation is generated by a local oscillator (e.g. a quartz oscillator, laser, or synthesizer). This oscillatory signal of the local oscillator is tuned to

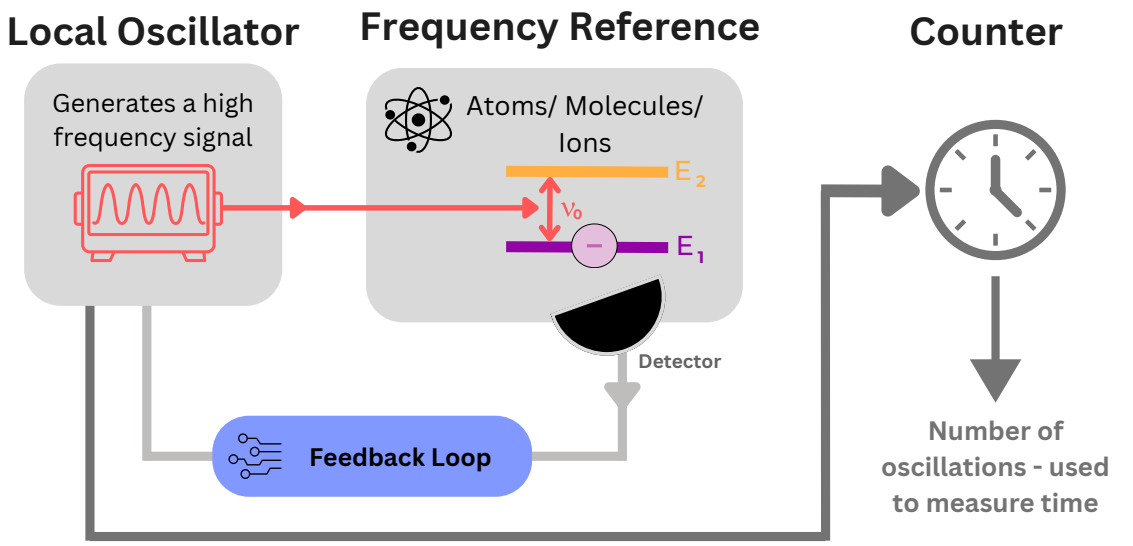

Figure 5.1: Principle of operation of an atomic clock. The atomic clock relies on the precise frequency of the atomic/molecular/ion transitions as a reference. A local oscillator generates a signal that is used to excite the atoms, and a feedback loop adjusts its frequency to match the atomic transition frequency. Once the local oscillator matches the atomic reference closely, the stable frequency is counted using a counter that measures the number of oscillations to determine the time.

match the frequency of an atomic transition. The atoms are typically prepared in a known internal state (e.g. the ground state) and then exposed to the oscillator's radiation. If the frequency matches the transition frequency, it induces transitions to the excited state. The outcome of these changes of state is then detected through various techniques, e.g. fluorescence or absorption spectroscopy, depending on the clock architecture. The system uses this signal to continually adjust the oscillator frequency to match that of the atom's transition frequency.

5.1.1 Noise Sources and Errors

The extent to which the frequency of a local oscillator can be synchronised with the unperturbed resonance frequency of atoms is constrained by the presence of noise in the measurement procedures employed for establishing this synchronisation, either through

external environmental effects, e.g. magnetic and electric fields that induce perturbations to the natural frequencies of the atoms or through noise in the stabilisation or readout processes. Although ways of mitigating these "systematic" frequency shifts are used, there are still errors in the correction processes which need characterisation.

Therefore, there are two types of errors in frequency standards (a) statistical errors originating from measurement fluctuations (b) errors in the systematic effect corrections [38]. The errors are typically characterised in terms of fractional frequency errors $\Delta f/f_0$, where f_0 is the frequency of the reference transition and Δf is the frequency error.

Statistical Errors

Defining the frequency of the clock transition used as f_c (considering there is a shift from f_0 due to systematic effects) we first suppose that the local oscillator has a frequency of f_s which is very close to f_c and is a perfect oscillator. Under this assumption, the fractional frequency deviation can be measured as $y \equiv (f_c - f_s)/f_0$ which is averaged over various probe durations τ. The Allan variance is a commonly used measure for the clock noise performance [38, 173] and is defined as

$$\sigma_y^2(\tau) = \frac{1}{2(N-1)} \sum_{i=1}^{N-1} [y(\tau)_{i+1} - y(\tau)_i]^2 \tag{5.1}$$

The Allan variance represents the squared fractional frequency fluctuations over averaging intervals of duration τ. In the equation above, N represents the total number of fractional frequency values, i is the sequential measurement index out of the N values and $y(\tau)$ is the average fractional frequency difference over the measurement interval τ. In this version of the Allan variance, it is assumed that there is no dead time between measurements. The quantity $\sigma_y^2(\tau)$ is a measure of instability, but it is usually referred to as "stability". More

sophisticated methods of calculating the variance are found in [173]. It is worth noting that there are no perfect standards to compare clocks to. Therefore, $\sigma_y^2(\tau)$ is calculated by comparing two imperfect clocks and contains noise from both.

Systematic errors, by contrast, must be assessed through insight into the physical effects that cause them. These range from static offsets of unknown magnitude to time-varying offsets with non white frequency noise. In this work, static offsets do not affect our conclusions. Therefore, conservatively assume that all reported systematic uncertainties result in frequency noise with a 1/f power spectral density (PSD).

5.2 Theoretical Models

For the work in this chapter, we assume that new physics is captured by a real scalar field ϕ and the leading-order interactions with ordinary matter can be written as

$$\mathscr{L}_{\text{int}} \sim \frac{\phi}{M_p} m_p \bar{p} p + \frac{\phi}{M_n} m_n \bar{n} n + \frac{\phi}{M_e} m_e \bar{e} e \,. \tag{5.2}$$

In this work, we focus on effective couplings to composite particles, i.e. protons and neutrons. While these interactions could be decomposed further into couplings to fundamental Standard Model particles [154, 174], the effective description is sufficiently general and a good approximation for describing and probing low-energy phenomena in atomic clock experiments. As such, Equation 5.2 can be considered representative of a wide range of theoretical models that investigate fundamental constituents and their interactions.

For this analysis, we assume that protons and neutrons couple equally to the scalar field ($M \equiv M_p = M_n$). The key physical scale is then determined by the differential coupling

between nucleons and electrons:

$$M_{\rm eff} \equiv \left(M^{-1} - M_e^{-1}\right)^{-1} \ . \tag{5.3}$$

While many modified gravity models assume universal couplings - often motivated by a Jordan-frame metric - our framework is more general and permits non-universal couplings, which are typical in searches for equivalence principle violations [175, 176, 177].

From the interaction Lagrangian above, one can infer how the proton-to-electron mass ratio μ depends on the scalar field ϕ. For each fermion $\psi \in p,n,e$ we have one term where of the corresponding fermion becomes $m_\psi(\phi) = m_\psi(1+\phi/M_\psi)$. Therefore, the effective time-varying mass ratio of the particles is

$$\begin{aligned}\mu_{\rm eff}(t) &= \frac{m_p(1+\phi(t)/M_p)}{m_e(1+\phi(t)/M_e)} \\ &\approx \mu\left(1+\frac{\phi(t)}{M_p}-\frac{\phi(t)}{M_e}\right) = \mu\left(1+\frac{\phi(t)}{M_{\rm eff}}\right) \ .\end{aligned} \tag{5.4}$$

In general, the scalar field $\phi = \phi(\vec{x},t)$ may depend on both position $\vec{x}$ and time t. However, this study focuses on cosmological signals that are spatially uniform, so we take $\phi = \phi(t)$. We also account for spatial variations that, due to Earth's orbital motion, manifest as time-dependent changes in Earth's reference frame, effectively giving $\phi = \phi(\vec{x}_{\rm Earth}(t),t) = \phi(t)$.

An experiment may place limits on how the effective mass ratio $\mu_{\rm eff}(t)$ changes over a given time interval, expressed as $\Delta\mu = \mu_{\rm eff}(t_2) - \mu_{\rm eff}(t_1)$. By normalizing this change to

the average value $\bar{\mu}$, we obtain the relation

$$\frac{\Delta\mu}{\bar{\mu}} = \frac{\Delta\phi}{M_{\rm eff}}\,, \tag{5.5}$$

which links the observable variation in μ to the corresponding change in the scalar field ϕ in the given timescale. From this, it is clear that we require two ingredients to be able to measure a signal in atomic clocks: (a) a non-universal coupling to a combination of neutrons, protons and electrons i.e. a universal coupling corresponding to $M_p = M_n = M_e$, or $M_{\rm eff} \to \infty$ would produce $\Delta\mu = 0$ and (b) a variation in ϕ that takes place over the experimental timescale. The nature of this variation is theory-dependent and may originate from either local or cosmological sources. In this work, we classify three distinct types of signals, each associated with a different scenario in fundamental physics.

- **Modified gravity & tests of fundamental physics:** The interaction between the scalar field and matter, as described in Eq. (5.2) suggests that matter acts as a source for the scalar field. This behaviour appears in many theories and models that involve a screening mechanism [12]. These include the Vainshtein mechanism [178, 179, 9], the Chameleon screening mechanism [180], or other screening mechanisms that effectively reduce the coupling between the scalar field and matter [181, 182, 183, 184, 185]). Close to the Earth, the Sun is a dominant source of such scalar fields. As the Earth orbits around the Sun, there is a variation in the distance between the two of about $\sim$1%. This change induces a periodic change in the scalar field of $\phi \sim \sin(2\pi t/\text{year})$, which in turn leads to an oscillation in the mass ratio μ with a period of one year and a known phase.

- **Dark energy:** In many models, dark energy is represented by a slowly evolving

scalar field known as quintessence [186, 35], which evolves over time under the influence of its potential $V(\phi)$. This results in the production of a field that evolves over time $\phi = \phi(t)$. This induces a corresponding change in μ. On the timescales relevant for current experiments (typically a few years), this variation can be approximated as linear: $\phi \sim \sqrt{\rho_{\rm KE}}t$, where $\rho_{\rm KE}$ is the kinetic energy of the dark energy field, constrained to be much less than $(2.4\ \text{meV})^4$.

- **Dark matter:** Models involving ultra-light dark matter predict that background field oscillations are produced of the form $\phi \sim \sin(mt)$, where m is the scalar particle mass spanning in the range $10^{-23}\ \text{eV} < m < \text{eV}$ [187]. It is therefore predicted that the oscillations produce sinusoidal variations in μ over timescales of $10^{-15}\ \text{s} < m^{-1} \lesssim 1$ year.

A summary of the signals used in this work is presented in Table 5.1. The table also summarises some of the analysis results presented in this chapter and compares them with the best (to our knowledge) existing constraints. The most relevant existing bounds on such signals include other clock experiments, the Planck [16] and MICROSCOPE [177] satellites, and lunar laser ranging [188]. The comparison of our results with those from other experiments is presented in subsequent sections.

5.3 Existing and simulated clock data

In this Section we conduct a preliminary search for the signals described in Section 5.2. We utilise publicly available data from Circular T (Section 5.3.1) and employ a Markov-Chain-Monte-Carlo (MCMC) and a Fisher matrix technique to project the sensitivity of different combinations of clocks (Section 5.3.2). Lastly, we use simulated data from state-of-the-art atomic clocks to forecast their sensitivity to potential signals, thereby es-

Signal type	$\Delta\mu/\bar{\mu}$ signal	CaF/Sr (projected)	Sr/Cs (projected)	Circular T [171]	Best existing constraint	Units
Modified Gravity	$A\cos\left(\frac{2\pi t}{\text{year}}\right)$	7.8×10^{-18}	1.4×10^{-16}	4.3×10^{-17}	2.3×10^{-16} [189]	None
Dark Energy	At	1.7×10^{-25}	3.1×10^{-24}	1.6×10^{-20}	1.1×10^{-24} [167]	s^{-1}
Dark Matter	$\frac{A}{\omega}\cos(\omega t+\delta)$	1.5×10^{-24}	2.8×10^{-23}	3.6×10^{-17}	See Fig. 5.2	s^{-1}

Table 5.1: Summary of types of signals in variations of μ due to fundamental physics. All values stated are the standard uncertainties in the associated parameter A as defined in the first column, i.e. σ_A. This represents approximately the largest such signal that could reasonably escape detection. For the dark matter signal, the values in the table show the forecast error on A assuming a fiducial value of $\omega = 2\pi\,\text{yr}^{-1}$ after marginalizing over that parameter as well as the phase δ. The full frequency dependence of this constraint is illustrated in Fig. 5.2. Each of these generalized signal types will be connected to fundamental physics theories in Sec. 5.4.

tablishing constraints on relevant theoretical models based on their noise profiles. The constraint plots produced using the simulated data generation of state-of-the-art atomic clocks are presented in Sec. 5.4.

Throughout this work, we use the framework presented in Ref. [159] to relate the frequency ratios of atomic clock pairs to potential variations in the fundamental constant μ. The sensitivity of a specific atomic or molecular transition, denoted by ν_i, to changes in a fundamental constant represented by $X = \{\alpha, \mu\}$, is quantified by a sensitivity coefficient denoted as K_X.

The sensitivity to variations in a particular fundamental constant X for a given frequency ratio R = ν_1 / ν_2 is directly proportional to the difference between the sensitivity coefficients:

$$\frac{\Delta R}{R} = [K_{X,1} - K_{X,2}]\,\frac{\Delta X}{X}\,. \tag{5.6}$$

A higher value of K_X indicates greater sensitivity of the specific transition to variations

of X. For optical electronic transitions $K_{\mu,opt} = 0$; for molecular vibrational transitions $K_{\mu,vib} = -\frac{1}{2}$; and for hyperfine microwave (MW) transitions $K_{\mu,MW} = -1$ [169, 190]. For K_α, the sensitivity coefficients depend on the detailed atomic structure of the atom or molecule considered. See Ref. [159] for a discussion on how these sensitivity coefficients are derived.

The transition frequencies of the atomic clocks considered in this work can be written in the form [159]:

$$\begin{aligned} \nu_{\text{opt}} &= A \cdot F_{\text{opt}}(\alpha) \cdot cR_\infty \,, \\ \nu_{\text{vib}} &= C \cdot \left(\frac{m_e}{m_p}\right)^{\frac{1}{2}} \cdot cR_\infty \,, \\ \nu_{\text{MW}} &= B \cdot \alpha^2 F_{\text{MW}}(\alpha) \cdot \frac{m_e}{m_p} \cdot cR_\infty \,, \end{aligned} \tag{5.7}$$

with the Rydberg constant $R_\infty = \frac{c}{4\pi\hbar}\alpha^2 m_e$. The $F(\alpha)$ terms account for relativistic perturbations to the atomic structure, which can be significant in heavier elements. [2]

5.3.1 Testing the models on Circular T data

To provide a baseline for constraints on the classes of signal described in this paper, we performed a preliminary study using publicly available data published monthly by the BIPM through Circular T [171]. The BIPM provides a monthly release of the BIPM's Time Department data, allowing for local realisations of UTC(k), which are maintained by national institutes, to trace back to the Coordinated Universal Time (UTC). UTC is a globally recognised time standard used as a reference for timekeeping and is established

[2] It should be noted that for the microwave hyperfine transition frequency, Eq. (5.7) neglects two small but potentially non-negligible effects: the variation of the nuclear magnetic g-factors [191, 192] and the variation of the nuclear radius [193, 194]. In this work, we use effective couplings to entire nucleons, so a discussion of effects due to varying nuclear structure is beyond the present scope of discussion but would be an interesting exploration in future work.

using data from atomic clocks operated by over 80 contributing institutes worldwide [195, 196]. Since the definition of the SI second is based on the frequency of the hyperfine transition in caesium, most clocks contributing to TAI are caesium-based with $K_\mu = -1$. However, in recent years, contributions from clocks based on optical transitions have emerged [171] which have $K_\mu = 0$. In this work, we exploit this difference in sensitivity to test for variation in μ by assuming that the mean value of TAI is entirely determined by the caesium transition, and comparing individual strontium and ytterbium optical clocks against this total mean to extract a cross-species frequency ratio.

The data used to produce the constraints and the mapping from that data to $\Delta\mu/\mu$ are presented in Appendix A. For this analysis, values of d, the negative fractional frequency deviation of TAI, for individual optical frequency clocks as reported in Circular T are used as described in the same Appendix. It is assumed that this value is proportional to $\Delta R/R$ and therefore to $\Delta\mu/\mu$ where R is the ratio of frequencies of the optical clock considered to the mean caesium transition frequency.

After collating the data for all the optical clocks contributing to Circular T (Fig. A.1, in Appendix A), we use Bayesian inference to evaluate the posterior distribution of the unknown parameters in our models. Three models were used: (a) a sinusoidal model with a fixed period of one year with the amplitude as the only free parameter, (b) a linear model with the gradient as the unknown parameter, and (c) a sinusoidal model with an unknown period and phase. We use the `emcee` Python package [197] to perform an MCMC analysis of the (log)-posterior distribution in the theoretical parameters given the data.

The constraints produced from this analysis are presented in Table 5.1 for comparison with the other constraints on the associated parameters stated. It should be noted that this analysis is limited by assuming that the quoted uncertainties are reliable and that there are

no correlations between measurements of the same clocks.

We also assume that all optical clocks from all the different laboratories are affected in the same way by the physical phenomena, and that the uncertainties in the measurement of $\Delta R/R$ is affected by a gaussian noise, with no correlations between different clock pairs. As a point of comparison, the maximum allowed signals in the data that could have escaped detection are summarised in Table 5.1.

5.3.2 Forecasts with state-of-the-art atomic clocks (Fisher information)

To forecast the possible observation of variations in fundamental constants using current state-of-the-art atomic clocks, a Fisher forecast method is adopted, along with a MCMC analysis, to evaluate the projected sensitivity of the experiments to potential signals of fundamental constant variations. Those methods are widely used in cosmology [198] as tools for parameter estimation forecasts, which inform the development of future experiments.

The Fisher matrix method is a Bayesian inference approach, and the method is used to detect potential variations in the ratio of the measured frequencies of two clocks over time. For the clock projections, we simulate a datastream sampled with a cadence of 1 second, coming from the superposition of the frequency ratio $\Delta R/R$ induced by our set of theories and the instrumental noise from a realistic noise model built on the physical properties of the clocks considered.

This data stream is Fourier transformed into the frequency domain to facilitate the analysis of the signal characteristics and separate it from noise. The noise is assumed to be Gaussian and stationary with zero mean, and we assume the datastream is ungapped. The

relaxations of these assumptions are not expected to significantly impact the forecast, even if the analysis will become much more challenging in practice. The Fisher approximation of the posterior distribution of the unknown parameters is then analytically computed to have a quick and reliable estimate of the confidence intervals to produce analytical and interpretable forecasts. An MCMC evaluation of the full forecast posterior distribution has been done to check the validity of the Fisher approximation. The clock characteristics used in this part of the analysis can be found in Appendix B Table B.1.

5.3.3 Forecasts - Simulated Data

This Section presents the method used to create simulated clock data to derive constraints on the various models using Bayesian inference. A numerical simulation is implemented to generate synthetic datasets consisting of a signal embedded in noise.

The analysis is carried out in the frequency domain instead of the time domain. This is because the noise profile includes a $1/f = 2\pi/\omega$ dependence noise term (flicker/pink noise), which implies correlations in the noise of the data points in the time domain, making the analysis more complex and computationally expensive as the correlations would need to be explicitly handled. Working in the frequency domain, where the covariance matrix of the data is diagonal, removes this requirement and simplifies the analysis.

We first generate noise with white and pink noise components for two clocks by modelling the noise profile of the clocks using the one-sided power spectral density (PSD) for a single clock, as indicated in Eq. B.1. The values for the coefficients used for each clock are presented in Table B.1. The total duration of the simulated signal is three years with a cadence of one second. Two clocks are required for sensitivity to variations in fundamental parameters, therefore, the combined resulting PSD of the two clocks is the

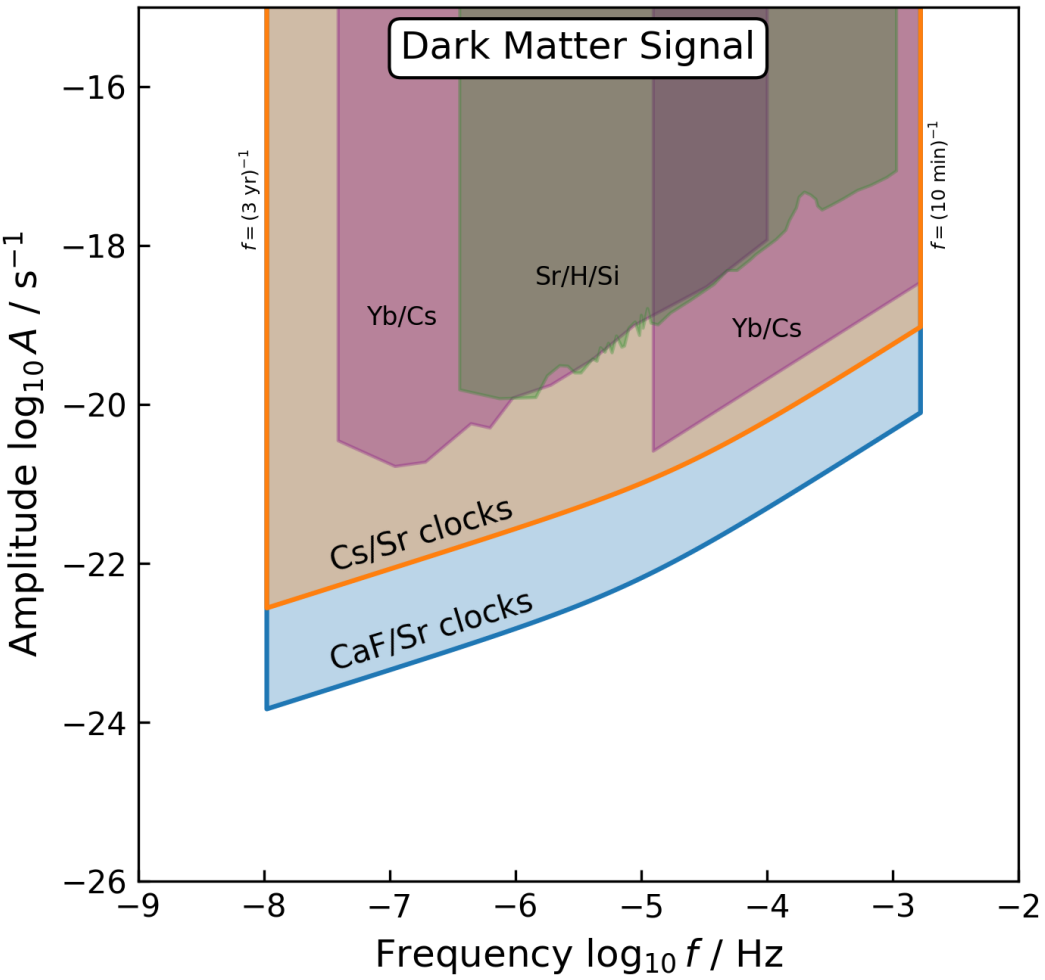

Figure 5.2: Comparison of projected and existing constraints on oscillations in $\mu_{\mathrm{eff}}(t)/\bar{\mu} = 1 + A/\omega \cos(\omega t + \delta)$. This signal is associated with ultralight dark matter theories. Also shown are currently-leading constraints from clocks in this frequency range [199, 200, 190]. Note that this figure is in terms of the ordinary frequency f, not the angular frequency $\omega = 2\pi f$.

combination of the individual PSDs for each clock assuming that the noise streams of the individual clocks are uncorrelated. The resulting PSD is a summation of the individual clocks PSD. The combinations of clocks used are presented in Fig. B.1b (bottom plot).

The signal predicted by the theories considered is parametrized in the frequency domain

and then added to the simulated noise stream. The injected signal is determined in the frequency domain for all different scenarios by taking the Fourier transform of the time-domain signals outlined in Table 5.1. The MCMC analysis is then performed on the resulting dataset to obtain samples from the posterior distribution of the unknown parameters.

The values for the coefficients of the PSD are included in Table B.1. The MCMC sampling method described in the previous section is used to derive the posterior distributions for the different free parameters in question for the different models. The results are then used to investigate the relationship of different parameters of the models in question. Plots investigating the relationship of different parameters are presented, and the constraints on the space parameters imposed by different pairs of atomic clocks are also shown.

This was done for each of the signals listed in Table 5.1. The results for two representative samples of clock combinations are also listed in that table. The "dark matter" signal is slightly more involved because the threshold for detection of A now depends on the typical frequency of the signal ω. We therefore include additional information for this case as a worked example. The approach may be generalized straightforwardly for the other two fundamental physics signals types. One key distinction of the modified gravity signal is that the phase of the oscillations is set by the position of the Earth relative to the Sun, the details of which are discussed in Sec. 5.4.1.

For the dark-matter-like signal, we show the upper bound that the experiment can pose on the amplitude parameter A as a function of the value of the frequency of the signal, which is the curve

$$A > \sigma_A = \sigma_A(\omega_0)\frac{\omega}{\omega_0}\frac{N(\omega)}{N(\omega_0)} \tag{5.8}$$

where $N(\omega)$ is the noise power spectral density at frequency $\frac{\omega}{2\pi}$ and $\sigma_A(\omega_0)$ is the value of the forecast error in the measurement of the parameter A at the reference frequency $\omega_0 = \frac{2\pi}{1\text{yr}}$. The curve is shown in Fig. 5.2, with the values of $\sigma_A(\omega_0)$ displayed in Table 5.1.

5.3.4 Existing varying-μ searches

Variations in μ have been previously discussed in the literature in a variety of contexts. In this section, we briefly review a few of the most relevant existing measurements.

Six years of clock data were examined for oscillatory signals associated with dark matter with an Rb/Cs clock pair [201]. However, this particular clock pair has a sensitivity coefficient difference for μ of 0, making it difficult to perform a direct comparison in this work. Indeed, a nonzero sensitivity coefficient K_μ (described at the beginning of Sec. 5.3) is a key advantage of the clock pairs we focus on in this work. In the interest of facilitating comparison, we translate our bounds into the dark matter model used in that work. For details on how this was done, see Ref. [3].

A comparison of Cs/Yb/Sr clocks was combined to produce estimates of signals equivalent to our modified gravity and dark energy signals [189]. The uncertainty on the amplitude of the yearly modified gravity signal was $\sigma_A = 2.3 \times 10^{-16}$, which is directly comparable to our results. It is seen in Table 5.1 that this is roughly in line with our Sr/Cs clock projections and about 1.5 orders of magnitude weaker than our CaF/Sr projections. A comparison of non-continuous clock data over a period of roughly 13 years was also undertaken to search for a linear drift in μ, which was measured to be $\dot{\mu}/\bar{\mu} = (5.3 \pm 6.5) \times 10^{-17}/\text{yr}$. Converting this uncertainty into units of s^{-1} allows for a direct comparison to our dark energy signal, and rules out $A \gtrsim 2.1 \times 10^{-24}$ s^{-1}. Refer-

ring to Table 5.1, we see that the measurement is roughly in line with our Sr/Cs clocks projection and about one order of magnitude worse than the CaF/Sr projection.

Frequency comparisons between a strontium clock, silicon cavity, and hydrogen maser were performed to search for ultralight dark matter [199]. Those bounds are stated in terms of a scalar-electron coupling parameter d_{m_e} which is related to our $M_{\rm eff}$ by

$$M_{\rm eff} = \frac{\sqrt{2}M_{\rm Pl}}{d_{m_e}} \,. \tag{5.9}$$

Those bounds are included in Fig. 5.6. To translate the bounds to the amplitude signal of Fig. 5.2, we use Eq. (5.25) to compute the signal amplitude as

$$A = \frac{\sqrt{2\rho_{\rm DM}}}{M_{\rm eff}} \tag{5.10}$$

where we have used the local density for dark matter as described in Sec. 5.4. Also of note is a search using Yb/Cs clocks which ran for 298 days [200], and is also included in Fig. 5.2. In a similar vein there are a number of experiments that constrain ultralight dark matter in this range, particularly NANOGrav [31] which appears on Fig. 5.6. More generally a number of constraints on the ultralight dark matter-Standard Model interactions are summarised in [202].

More recently, data from Yb, Sr, and Cs clocks was used to search for oscillatory ultralight dark matter signals [190]. This data is in 600s intervals and was collected over a period of two weeks. Since the dark matter signal in Table 5.1 is normalized to 1 year, this result is omitted from the table, but it is included in Figs. 5.2 and 5.6. These bounds cover a similar frequency range as explored here, and are approximately one order of magnitude weaker than our current projections.

The coupling between clock frequencies and the Newtonian gravitational potential were measured in [166], and was summarized for a variety of atomic species. Unfortunately, this result is not directly comparable to our approach without additional theoretical modelling, as the modified gravity models we focus on in this work fall off differently from the Newtonian potential. In future work, it would be interesting to translate their results into bounds on specific modified gravity models. A similar approach was taken in [167], although that work also constrained a linear temporal variation in μ to be $\dot{\mu}/\mu = (-8 \pm 36) \times 10^{-18}$ yr^{-1}. This corresponds to a maximum dark energy signal amplitude of $A \leq 1.1 \times 10^{-24}$ s^{-1}, making it, along with MICROSCOPE, one of the best current constraints on the EP-violating dark energy signal.

It was recently proposed to search for chameleon particles by employing two identical clocks, where one of the clocks is placed inside a massive source object (or with such an object nearby) to search for redshift effects [203]. Such effects could, in principle, be searched for with the clocks under present consideration as well, although in this work, we focus on equivalence-principle violation searches through varying-μ as this is a unique feature of the clock combinations we are considering. It would be interesting to explore the potential for these clocks to search for the above signal, particularly for short-range forces, in future work.

5.4 Projected constraints on fundamental physics

This Section presents projected constraints on fundamental physics theories from state-of-the-art clocks for all three signals described in Section 5.2. These signals are associated with modified gravity, dark energy, and dark matter, respectively. In each case, the underlying physics is modelled as a single real scalar field ϕ, coupled to matter via

the interaction Lagrangian given in Eq. (5.2). The coupling to matter, along with spatial and/or temporal variations in the local scalar field value, leads to variations in the apparent electron-proton mass ratio $\mu_{\rm eff}$. In this section, we mainly emphasize the results on a few of the most novel or promising routes for detecting new fundamental physics rather than a broad overview of all possible theories that could be tested.

5.4.1 Fifth forces and screening

A direct scalar-matter coupling of the form Eq. (5.2) generically implies that the scalar field mediates a new "fifth" force between matter particles. There are a wide range of fifth force models in the literature, which are reviewed in [204, 205, 206, 12]. While clocks are not directly sensitive to this new force, they are sensitive to that force's potential, which is proportional to the local field value ϕ, as is clear from Eq. (5.4). The Sun, like all massive bodies, is a source for that potential. As the Earth orbits the Sun, the Earth-Sun distance varies at the level of $\sim 1\%$, leading to variations in ϕ (and hence the proton-electron mass ratio μ) on a one-year period. A similar approach was taken in [207], although that work focused on theories without scalar self-interactions and on variations in the fine structure constant α and particle masses.

For our purposes, many models can be analyzed via the same procedure where the additional degrees of freedom behave as a scalar in some limit. Then we can first consider the scalar field's equation of motion around the Sun in order to find $\phi(r)$, where r is the distance to the Sun. Then, we supply $r(t)$, which describes the Earth's distance to the Sun as a function of time. This allows us to compute variations in $\mu_{\rm eff}$ as a function of time via Eqs. (5.4). In this Section, we focus on a pair of modified gravity models, and further models are discussed in [3].

Leading theories of gravity which depart from four-dimensional General Relativity on large cosmological scales are associated with theories where the graviton is effectively massive either as a resonance or as an effect from extra dimensions [208, 209, 210, 211] or as a four-dimensional local theory of gravity [212, 213, 9]. While Lorentz-invariant theories of massive gravity (whether they are effective or not) involve additional degrees of freedom (or polarizations), that could in principle mediate fifth forces, they also come hand in hand with a Vainshtein screening mechanism [178, 214] which is best understood in the decoupling limit [215], where one of the degrees of freedom behaves as a scalar field (dubbed the Galileon) [216, 217]. The Vainshtein mechanism naturally ensures that scalar self-interactions suppress the fifth force sourced by massive objects and lead to a smooth massless limit. This theory is introduced in more detail in Ref. [3], while here we give a brief overview of this theory's relevant properties.

The Galileon is characterised by both a scalar-matter interaction set by the parameter M, as well as several nonlinear self-interaction terms which are set by the parameters Λ, c_4. Note that Λ is related to the scale of the graviton mass m_g in this theory by [218]

$$\Lambda^3 \approx m_g^2 M_{\rm Pl} \, . \tag{5.11}$$

Around a spherical source object of mass $m_{\rm obj}$ the Galileon's equation of motion is:

$$\left(\frac{\phi'}{r}\right) + \frac{2}{\Lambda^3}\left(\frac{\phi'}{r}\right)^2 + \frac{2c_4}{\Lambda^6}\left(\frac{\phi'}{r}\right)^3 = \frac{m_{\rm obj}}{4\pi M r^3} \, . \tag{5.12}$$

The terms on the left follow from the theory's ordinary kinetic term, its cubic self-interactions, and its quartic self-interactions in its Lagrangian, respectively. There are three parameters: Λ sets the overall strength of the Galileon's self-interactions, c_4 controls the relative strength of the quartic interactions, and M controls the strength of the

coupling to matter. Note that in the interest of simplicity we have coupled the Galileon to nucleons with equal strength and not at all to electrons (that is, in this section we take $M_e \to \infty$)[3].

Far away from the source, the cubic and quartic terms are strongly suppressed relative to the kinetic term, which may be intuitively understood by observing the additional factors of ϕ'/r in the equation of motion. As such, at large r, the field's behaviour is dominated by the ordinary kinetic term, giving a field profile that goes as $\phi \sim 1/r$, much like in Newtonian gravity. Closer to the body, the Galileon's self-interactions become significant, and the cubic interactions dominate the left-hand side of Eq. (5.12). Within this region, the falloff is reduced to $\phi \sim 1/\sqrt{r}$. The boundary between these two regimes is termed the "cubic Vainshtein radius" R_3. Closer still to the massive body, the quartic terms dominate, and the field profile tends towards a constant. Summarizing, we have

$$\phi(r) \sim \begin{cases} m_{\rm obj}^{1/3} & \text{for} \quad r < R_4^4/R_3^3 \,, \\ m_{\rm obj}^{1/2} r^{-1/2} & \text{for} \quad R_4^4/R_3^3 < r < R_3 \,, \\ m_{\rm obj} r^{-1} & \text{for} \quad R_3 < r \,. \end{cases} \tag{5.13}$$

The Vainshtein radii $R_{3,4}$ depend on the mass of the source and parameters of the theory and are given in Ref. [3].

As the Earth orbits the Sun, its distance varies as

$$\begin{aligned} r(t) &= a \frac{1-\varepsilon^2}{\varepsilon \cos(2\pi t/\text{year}) + 1} \,, \\ &= a \left(1 - \varepsilon \cos(2\pi t/\text{year}) + O(\varepsilon^2)\right) \,, \end{aligned} \tag{5.14}$$

[3]Strictly speaking, the source in Eq. (5.12) should not be the total mass, but only the fraction of the source's mass made up of nucleons. However, this distinction corrects the value of $m_{\rm obj}$ at the level of a part in 10^3 which makes a negligible difference to our present estimates.

where $a = \text{AU}$ is the average Earth-Sun distance and $\varepsilon = 0.0167$ is the eccentricity of Earth's orbit. This leads to yearly sinusoidal variations in ϕ, and therefore also in μ via Eq. (5.4). These variations are to be compared with the result of the statistical analysis searching for sinusoidal variations in μ with a one-year period, which is summarised in Table 5.1. Note that (unlike the case with dark matter) the phase of this signal is known and is set by the position of the Earth relative to the Sun.

To solve for the scalar field, we Taylor expand as

$$\phi(r) = \phi(a) + \phi'(a)(r-a) \ . \tag{5.15}$$

Only the second term varies in time via $r = r(t)$. Combining, we find

$$\frac{\mu(t)}{\bar{\mu}} = 1 + \frac{\phi'(a) a \varepsilon}{M} \cos(2\pi t/\text{year}) \ . \tag{5.16}$$

The result of this analysis is shown in Fig. 5.3. This analysis was done for a CaF/Sr clock pair over a period of three years, which was shown in Table 5.1 to be one of the most sensitive clock systems to the yearly periodic modified gravity signal.

We can make some general observations about these results. First, we can identify the three distinct regimes, depending on the size of Λ, corresponding to the regions where the quadratic, cubic, and quartic self-interaction terms each dominate. When Λ is large, the Vainshtein radii are smaller than the Earth-Sun distance and the Sun is therefore unscreened. Decreasing Λ, we see a region dominated by the cubic self-interaction term, and constraints weaken because of the stronger screening. Decreasing Λ further still we see a region dominated by the quartic term, with constraints that are weaker still thanks to the strong screening effect.

Also plotted on the figure are the constraints from MICROSCOPE [176, 177], a satellite-borne test of the universality of free-fall towards Earth. When screening is inactive (that is, at large Λ), the bounds from MICROSCOPE are superior to the projected bounds from clocks. However, in the screened regime the situation reverses and clocks appear more promising. This may be understood intuitively by examining Eq. (5.12). In the unscreened regime, which is to say when $R_{V3,4}$ are both smaller than the Earth-Sun distance and Earth-MICROSCOPE distance, the signal is proportional to m/r. For our clock setup we take $m = m_\odot$ and $r = \text{AU}$, while MICROSCOPE has the much smaller $m = m_\oplus$ and $r = R_{\text{microscope}} \approx 7000$ km. MICROSCOPE measures a much smaller source (the Earth) but at a far shorter distance, which more than compensates for the smaller source. Hence the constraints from MICROSCOPE are comparatively stronger. However, once screening becomes active, the signal instead goes as $m^{1/2}/\sqrt{r}$ and $m^{1/3}$ for the cubic and quartic regimes, respectively. In these cases, the falloff of the signal is smaller, so there is a comparatively smaller penalty for the Sun-clock measurement's longer baseline. It is for this reason that the clock constraints compare favorably against MICROSCOPE within the screened regime of the Galileon. Notably, we find that the constraint on M is improved by an order of magnitude over MICROSCOPE for the Λ that gives a graviton mass of order the Hubble scale, $m_g \sim H_0 \sim 10^{-33}$ eV.

This pattern is also evident in our second sample theory. For this, we present a parametrized interaction model. This model describes the field sourced by a spherical object of mass m_{obj} as

$$\phi' = \Lambda^2 \left(\frac{m_{\text{obj}}}{8\pi M}\right)^\alpha (\Lambda r)^{-\beta} \ . \tag{5.17}$$

Although we did not derive this from a Lagrangian, this phenomenological description encapsulates the behavior of a large number of modified gravity theories, which correspond to different choices of the parameters Λ, M, α, and β. Once again, for our pro-

jected clock constraints, we will choose $m_{\rm obj} = m_\odot$ and $r = r(t)$ is the Earth-Sun distance over time given by Eq. (5.14). The scalar field parameters α, M characterize the scalar-matter coupling, Λ is a mass scale related to the scalar field's self-couplings, and β describes how quickly the scalar field's potential falls off with distance from a source which is affected by the nature of the interactions (see for instance [211] for an example where additional extra dimensions lead to a different scaling). As a simple example, a free scalar field with a gravitational-strength Forecastscoupling to matter corresponds to $\alpha = 1, \beta = 2, M = M_{\rm Pl}$, and Λ cancels out. Projected clock constraints on this generalised interaction model for several sets of fiducial parameter values are presented in Fig. 5.4. Once again, we can observe the same general pattern as the Galileon: theories where the field drops off more slowly than $1/r$ compare more favorably against MICROSCOPE. For both modified gravity models, we see that the projected clock bounds are currently weaker than those deriving from lunar laser ranging (LLR) [188, 219, 220, 221]. A further factor of 100 improvement in clock sensitivity beyond what is projected here would result in clock bounds that are competitive with LLR.

5.4.2 Dark energy

One of the simplest models of dynamical dark energy is quintessence [186, 35], which involves a scalar field field rolling down some self-interaction potential $V(\phi)$:

$$\mathscr{L}_\phi = -\frac{1}{2}(\partial\phi)^2 - V(\phi)\ . \tag{5.18}$$

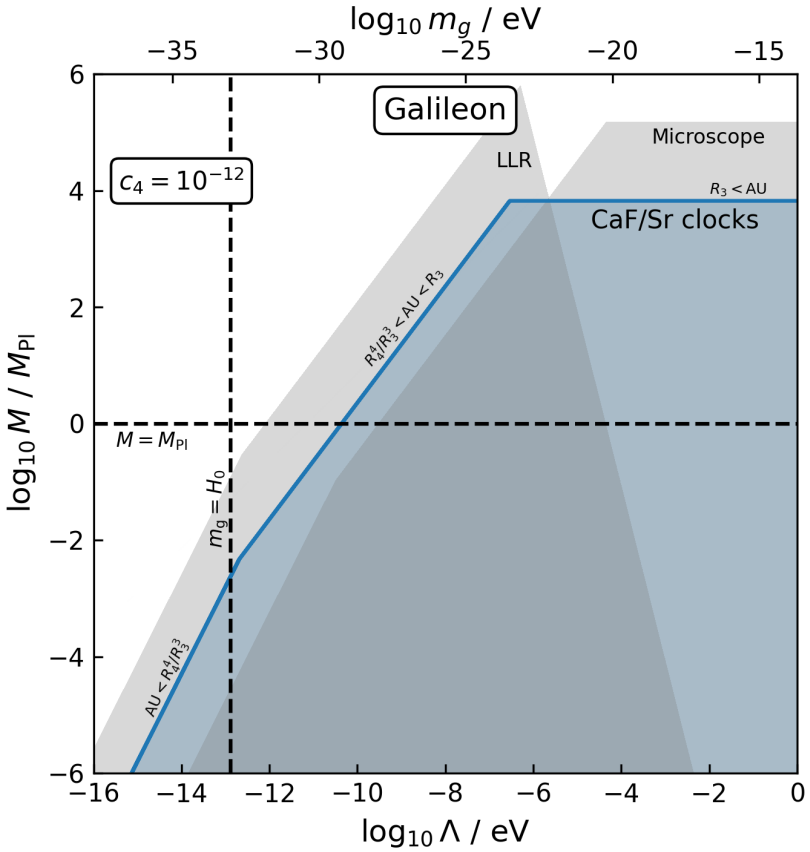

Figure 5.3: Constraints on Galileon parameter space from a CaF/Sr clock pair over a period of three years. The different power laws in the curve correspond to regions where quadratic, cubic, and quartic terms of Eq. (5.12) each dominate. The gray regions are ruled out by the MICROSCOPE experiment and lunar laser ranging, which are discussed in Ref. [3]. Also indicated are $M = M_{\rm Pl}$, which corresponds to a gravitational-strength matter-scalar coupling, and the Λ scale that corresponds to a graviton mass proportional to the current Hubble scale, as given by Eq. (5.11).

On cosmological scales, the field depends only on time, $\phi = \phi(t)$ and is, therefore, a perfect fluid with an equation of state and density

$$w = \frac{\frac{1}{2}\dot{\phi}^2 - V(\phi)}{\frac{1}{2}\dot{\phi}^2 + V(\phi)}\,,$$
$$\rho = \frac{1}{2}\dot{\phi}^2 + V(\phi)\,. \tag{5.19}$$

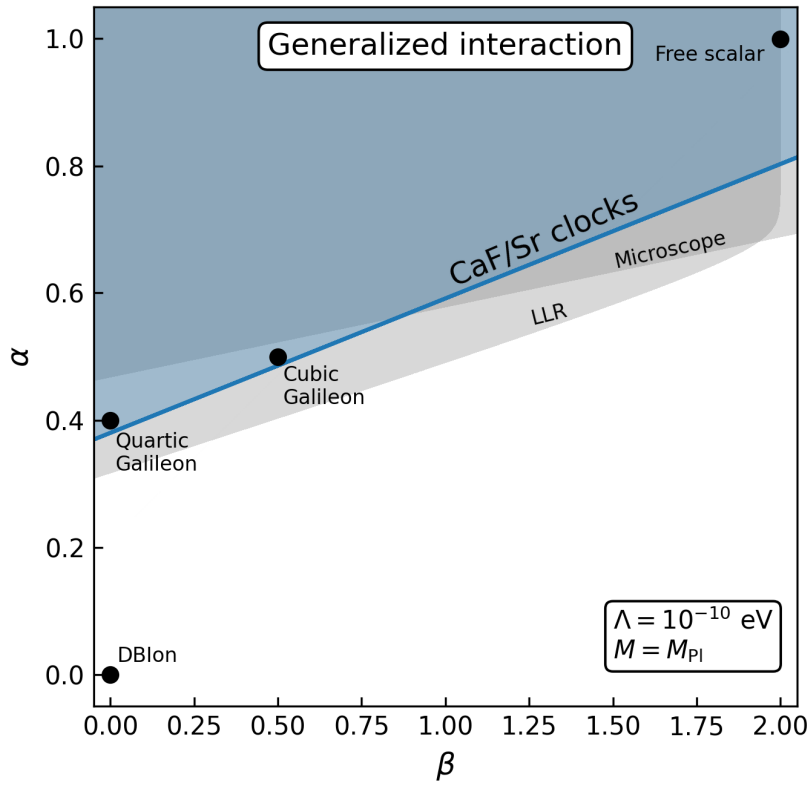

Figure 5.4: Upper panel: constraints on the space of parameters (Λ, M) in the generalized interaction modified gravity model (5.17). The lines define the lower bounds in the region of parameters (Λ, M) that can be ruled out by a CaF/Sr clock pair over a three-year observation time. Particular theories are highlighted: the free scalar, cubic Galileon, and quartic Galileon corresponding to each of the three regimes identified in Eq. (5.12), and also generalized ones that include DBI [217].

We know from cosmological measurements [16] that $w \approx -1$ and $\rho = \Lambda_{\rm DE}^4 = (2.4\ \text{meV})^4$. Clearly, this requires that we choose our potential such that $V(\phi) \approx \Lambda_{\rm DE}^4$, and that the potential is shallow enough such that the field only rolls very slowly $\dot{\phi}^2 \ll \Lambda_{\rm DE}^4$.

In the case $\dot{\phi} = 0$, then the theory reduces to a simple cosmological constant. Any amount of kinetic energy in the field causes the equation of state to deviate from $w = -1$, which then serves as a measure of how dynamical dark energy is. Through the couplings of

Eq. (5.2), it is possible to measure the amount of kinetic energy in the dark energy field via a time-dependent signal in μ.

Previous studies on this topic have focused on a non-minimal coupling to photons [222] (although not in the context of atomic clocks), or suggested using atomic clocks to search for dark energy theories that are coupled to matter via variations in the Higgs vacuum expectation value [223]. In the present case, we rely on two ingredients: the non-minimal couplings of Eq. (5.2) to generate a scalar field-dependent μ, and a nonzero amount of kinetic energy $\dot{\phi}$ to cause the field value to change over time.

If we assume that $\dot{\phi}$ is constant over the timescale of the experiment ($\sim$years) then it is possible to constrain quintessence in a model-independent way. Since $\dot{\phi}$ is constant, over some time period Δt the field changes by an amount $\Delta\phi \approx \dot{\phi}\Delta t$. Then we have via Eq. (5.5)

$$\frac{\Delta\mu}{\bar{\mu}} = \frac{\dot{\phi}}{M_{\rm eff}}\Delta t \approx \frac{\sqrt{2}\Lambda_{\rm DE}^2}{M_{\rm eff}}\sqrt{1+w}\Delta t \ , \tag{5.20}$$

where in the second equality we have used Eq. (5.19) and $V(\phi) \approx \Lambda_{\rm DE}^4$. The maximum allowed deviation from $w = -1$ for a canonical scalar field model of dark energy, as measured by Planck, is $-1 \leq w < -0.95$ at the 95% confidence level [16]. It should also be noted that there may be a growing preference for dynamical dark energy from baryon acoustic oscillations [224].

The scalar field is assumed to be essentially massless on the scale of the Solar System. As such, tests of the equivalence principle and fifth force tests constrain this theory tightly. Assuming equivalence principle violation (as we must in order to measure any change in μ with clocks) then the strongest experimental bound comes from MICROSCOPE (see Ref. [3] for the full derivation). A comparison of the expected constraints from atomic clocks to the bounds from MICROSCOPE and Planck are shown in Fig. 5.5. The clock

bounds strengthen as w increases away from $w = -1$ because this corresponds to more kinetic energy in the dark energy field, giving a larger change to the electron-proton mass ratio over a given period of time.

5.4.3 Dark matter

Dark matter may be modeled as a canonical scalar field with a mass m:

$$\mathscr{L}_\phi = -\frac{1}{2}(\partial\phi)^2 - \frac{1}{2}m^2\phi^2 \,. \tag{5.21}$$

Cosmologically, we once again assume $\phi = \phi(t)$ such that dark matter is a perfect fluid with an equation of state $w_{\rm DM} = 0$ and present-day density $\rho_{\rm DM} \approx 0.3\rho_0$, where ρ_0 is the cosmological energy density. The equation of motion following from Eq. (5.21) is

$$(\Box - m^2)\phi = 0 \,, \tag{5.22}$$

where we are neglecting Hubble drag as well as the Standard Model couplings for the time being. This is a good approximation on short timescales compared to the Hubble time and in regions where the Standard Model field energy densities are small, such as in the vacuum of space. Cosmological solutions depend only on time, so the solution to Eq. (5.22) follows as

$$\phi(t) = \frac{\sqrt{2\rho}}{m}\cos(mt + \delta) \,. \tag{5.23}$$

The normalization is chosen such that ρ is the energy density of the oscillating background field. Using Eq. (5.19) we find an oscillating equation of state $w = \cos 2mt$. Although this equation of state oscillates between -1 and 1, so long as the period m^{-1} is short compared to the Hubble time the oscillations average to zero, giving $w = 0$ on cosmological timescales as desired. The average value of the dark matter density

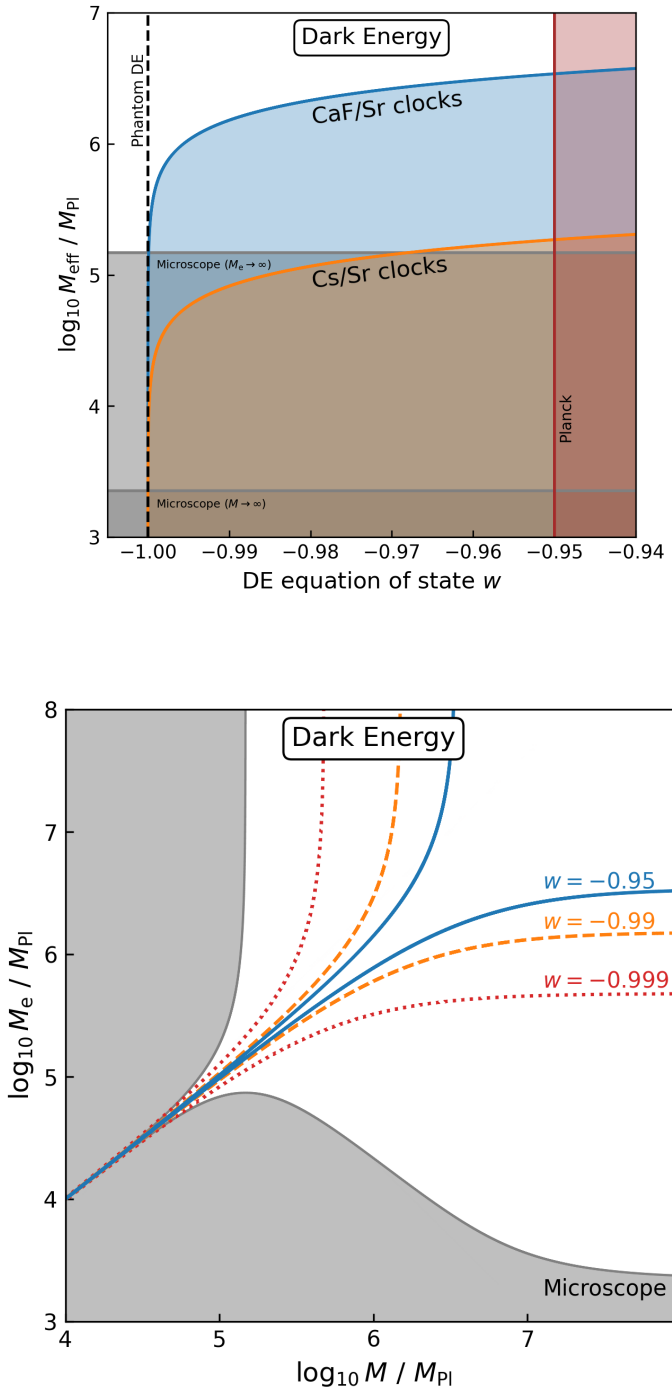

Figure 5.5: Projected bounds from clocks on quintessence dark energy, over an observation time of 3 years. A CaF/Sr clock pair was used for the bottom plot.

in the universe is $\rho_{\rm DM} \approx 10^{-11}$ eV^4. However, this is not the relevant quantity in our Solar System. The local dark matter density is significantly higher at approximately $\rho_{\rm DM,local} \approx 2.6 \times 10^{-6}$ eV^4 [225]. In fact, $\phi(t)$ is much more complicated within the galaxy, but over timescales shorter than the coherence time and length scales shorter than the coherence length, it still takes the form of Eq. (5.23), but with the local dark matter density $\rho_{\rm DM,local}$. The coherence time and coherence length are given by [226, 190]

$$\tau_{\rm C} = \frac{4\pi}{m v_{\rm vir}^2} , \quad \lambda_{\rm C} = \frac{2\pi}{m v_{\rm vir}} , \tag{5.24}$$

where $v_{\rm vir} \approx 200$ km s^{-1} is the virial velocity of our galaxy. The maximum dark matter mass we consider is $m \approx \frac{1}{10 \text{ min}} \approx 10^{-18}$ eV. This corresponds to a coherence length of $\lambda_{\rm C} \approx 10^{12}$ km, which is larger than the Solar System. The corresponding coherence time is $\tau_{\rm C} \approx 240$ years, which is much longer than the measurement time of a few years. As such the whole mass range of dark matter particles under current consideration is well within the regime of applicability of Eq. (5.23).

To compute the resulting variations in μ we combine Eqs. (5.5) and (5.23) and find

$$\frac{\Delta\mu}{\bar{\mu}} = \frac{1}{M_{\rm eff}} \frac{\sqrt{2\rho_{\rm DM}}}{m} \cos(mt + \delta) . \tag{5.25}$$

We see that this is of the form $\Delta\mu/\bar{\mu} \sim \sin(\omega t)/\omega$. Signals of this form were searched for in the simulated clock data, with the result given in Table 5.1. Applying that result to the fundamental theory parameters $M_{\rm eff}$ and m gives the projected constraints in Fig. 5.6.

Also included in that plot is a comparison to existing constraints, the strongest of which come from CMB and large scale structure, the MICROSCOPE satellite, and existing clock constraints. Because the signal oscillates with frequency m, the maximum and minimum

timescales over which data is gathered are directly proportional to the range in m that may be constrained with clocks.

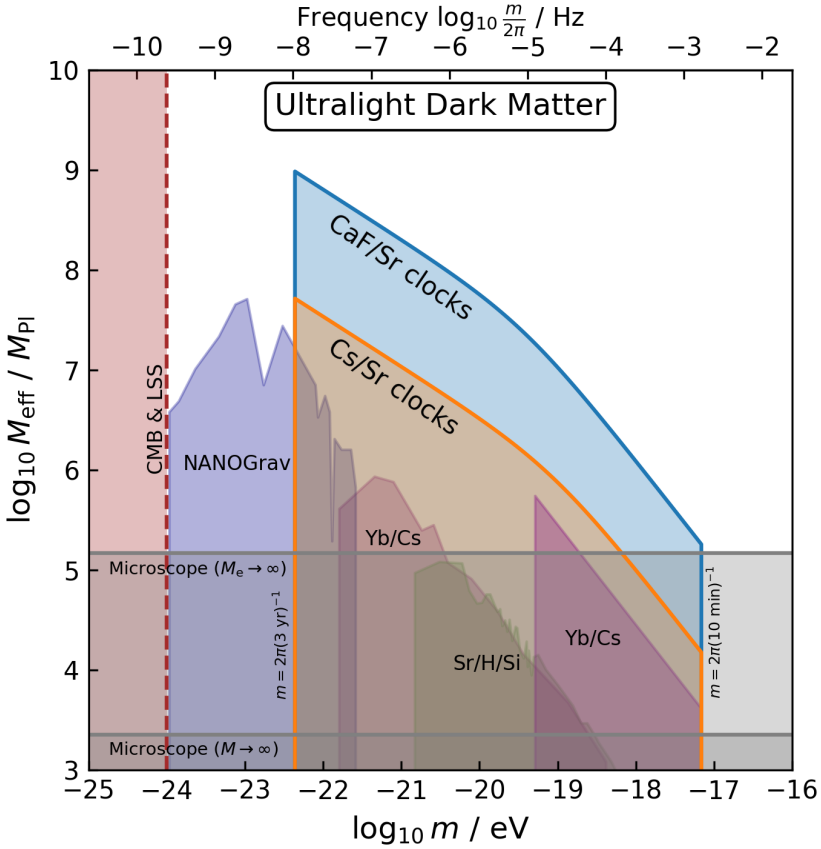

Figure 5.6: Constraints on the space of parameters (M, m) in the Dark Matter model defined in (5.23) after marginalizing over the unknown phase δ, for an observation time of $T = 3$ yr. Also plotted are constraints from NANOGrav [31] and Yb/Cs clocks [200, 190] which were drawn from [202], as well as Sr/H/Si clocks [199], and the MICROSCOPE satellite [177]. The best torsion balance curves [227] sit approximately one order of magnitude below the MICROSCOPE line and hence are not included in the figure. Planned atom interferometry experiments will also be sensitive to the higher end of this mass range (10^{-19} eV $\lesssim m \lesssim 10^{-11}$ eV) within the next few years [228].

5.5 Forecast Tool

In this Section we present a software package which can be used to extract constraints for the three signals described in Section 5.2, and was used in the creation of this work. The tool takes in a set of clock characteristics, a phenomenological model of new fundamental physics, generates a simulated data stream, and applies the MCMC method as described in Sec. 5.3.3 to perform parameter estimation. This forecasts the maximum amplitudes for signals in the time variation of μ that are associated with new physics, specifically dark energy, dark matter, and modified gravity. The results are then used to generate constraint plots for the different theory scenarios.

The key parameters that must be provided by the user are:

- The value of the Allan variance for the instability, the accuracy and the sensitivity coefficient K for all the clocks used,
- A list of clock pairs to be considered and
- The functional form of the phenomenological models one wishes to forecast in the frequency domain. The models used investigated in this work are included.

The software then generates a set of model-independent constraints for the desired signals in $\mu(t)$. We have included the analysis to map those variations onto constraints on the theories.

This setup is designed to be extended to a wide variety of EP-violating theories from arbitrary clock characteristics. This is demonstrated in the following example. Let us assume the user wishes to evaluate the capabilities of two new clocks nicknamed “C1” and “C2”. The user adds a line for each clock in stats/clocks_parameters.csv, supplying the

information on the instability, accuracy and constant K for each clock. Furthermore, the user specifies the clock combination C1/C2 in stats/clocks_pairs.csv. The user then runs the statistical analysis via the supplied makefile, simply running the command "make" from the command line. This generates a new line in the stats/sigma_A_table.csv file, giving the uncertainty in the amplitudes for each of the generalized signals in Table 5.1. These can also be queried programatically via an API that is detailed in the code's documentation, and was used in the generation of the theory bound figures in this work. If desired, one could replace the Cs/Sr clock projections with the C1/C2 clock projection by replacing the clock pair name in each of the plotting scripts supplied with the software package. The software package is publicly available[4] and the version used for this work is permanently archived at [229].

5.6 Gap Analysis

In the previous analysis, it was assumed that the data were taken continuously and had no gaps. However, in real-world long-running clock experiments, data acquisition is often interrupted by various factors, including hardware malfunctions, calibration procedures or environmental disruptions. To evaluate the robustness of signal detection methods under such conditions, it is important to simulate the presence of missing data within otherwise continuous time series.

This section presents a preliminary study to test the effect of gaps in the search for a sinusoidal signal of a period of one year, the signal which corresponds to the modified gravity model.

[4] https://github.com/elizabeth-pa/clock-constraints

5.6.1 Synthetic Dataset Generation of Atomic Clock Noise

To simulate realistic atomic clock noise for this analysis, synthetic time-series datasets were generated using Python, similar to the previous analysis. The simulated noise dataset was generated similarly to the previous analysis (see Sec. 5.3.3, but the dataset is converted to the time domain instead. For this preliminary study, only one set of clocks is used, namely Strontium and Caesium, using state-of-the-art values for their stability accuracy. The total simulated duration was 3 years at 1 Hz resolution.

To generate the time-domain signal, the combined one-sided PSD was used to shape Gaussian white noise in the frequency domain using a fast Fourier transform (FFT)-based method. For white noise, the one sided power spectral density (PSD) was flat and scaled by $h_0 = 2\sigma_1^2$; for pink noise, it followed a $1/f$ profile and was scaled by $h_{-1} = \frac{\sigma_2^2}{2\ln 2}$, where σ_1 and σ_2 are the desired Allan deviations at short and long averaging timescales, based on published values for optical clocks. The signal was then converted back to the time domain via inverse FFT. As the stochastic nature of the process can lead to slight deviations from the theoretical Allan deviation values, the frequency-domain signal was scaled before applying an inverse FFT to match the target Allan deviation at relevant averaging times, i.e. to match the desired instability and accuracy values.

A simulated noise time series was generated for each clock individually. These time series can then be combined by summing them, resulting in a composite dataset that will be used for signal detection, since $K_{\mu,Cs} = 0$ and $K_{\mu,Sr} = -1$. This produces a continuous combined dataset without gaps, suitable for searching for the physics signals under question.

5.6.2 Simulating Realistic Data Gaps

The next step in the process was to introduce gaps in the simulated noise datasets. A custom algorithm was designed and implemented to introduce realistic stochastic gaps into the simulated data. The method takes the full datasets generated for individual clocks and eliminates a percentage of data points to represent missing intervals. The percentage of the total length of the dataset that is eliminated can be determined by the user. For this analysis, we simulated gaps in the range of approximately 30-60% of the total data, which is in line with the amount of data missing from a state-of-the-art clock dataset.

The sizes and frequencies of these gaps are modelled on a mixed probability distribution to reflect close to realistic conditions. In a real clock experiment, smaller gaps are the most frequent, while larger gaps happen with lower probability. For each gap, a random starting index is chosen within the dataset, and a gap is inserted based on the probabilities defined. The process repeats in a loop until the specified proportion of missing data has been reached. In each iteration, a random number is drawn to determine the duration of a gap based on a mixed probability model. Short gaps ($\sim$ 1 second) occur with the highest probability (80%), representing brief data dropouts or glitches. Medium-duration gaps (minutes to several hours) occur with a moderate probability (15%) and the duration is drawn from an exponential distribution with a mean of 30 minutes and capped at 12 hours. Long gaps are also drawn from an exponential distribution with a mean of 5 days and a maximum of $\sim$ 30 days and occur with a probability of 5%. This stochastic method ensures that the location and duration of the gaps in the dataset are random and reflective of real scenarios.

To evaluate the effect of data gaps on signal detection, 1,000 synthetic datasets were generated for each clock type (strontium and caesium) using the method described in

Section 5.6.1. Gaps were introduced into each dataset using the procedure outlined in this section. The two datasets were then combined by summing the simulated noise time series from the two atomic clocks. This process was applied both to the continuous datasets (without gaps) and to those with gaps.

Because the starting index of each gap was chosen randomly, some gaps overlapped. As a result, the actual percentage of missing data points in each individual clock dataset did not match the nominal percentage of gaps that were defined. Table 5.2 presents the average resulting percentage of missing data points for each level of defined gaps in the individual clock datasets, as well as for the resulting combined dataset. A sample time series combined dataset with gaps is shown in Figure 5.7.

Defined Gap %	**Sr Missing %**	**Cs Missing %**	**Combined Missing %**
40	33	33	55
50	39	39	63
60	45	45	70
70	51	51	75
80	55	55	80
90	60	60	83

Table 5.2: Average percentage of missing data (for all 1,000 toy datasets) for the strontium (Sr) datasets, the caesium (Cs) datasets and combined datasets after varying levels of artificially introduced gap percentages.

5.6.3 Model Fitting

A synthetic sinusoidal signal with a one-year period, representing a potential signature from a modified gravity theory, was injected into the combined noise datasets at varying amplitudes. A sinusoidal model with unknown amplitude was then fitted to each dataset using the `scipy.optimize.curve_fit` function in Python. The resulting best-fit amplitudes were extracted and collected across all datasets.

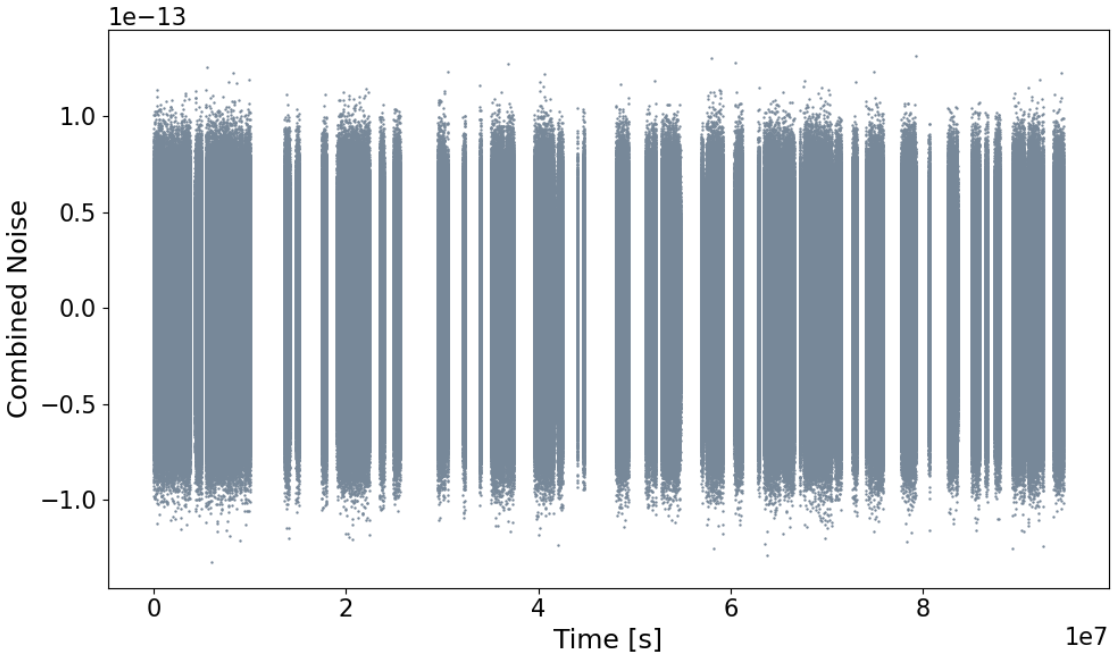

Figure 5.7: Sample of the simulated combined noise time series, obtained by summing the frequency noise deviations from a strontium and a caesium atomic clock. Missing data were introduced independently to each clock with a maximum allowed removal of 40%. In this example, 32% of the caesium data and 36% of the strontium data are missing. Due to overlapping gaps, the resulting combined dataset has approximately 54% missing data over the three-year period sampled at one-second intervals.

This allowed for a comparison of the results produced by using datasets with and without injected signals, as well as a comparison between datasets with and without gaps, to assess how missing data and the varying amplitude of injected signals affect signal recovery. The results of this analysis are presented in the following section.

5.6.4 Results

The distributions of the fitted amplitudes were visualised using histograms. Figure 5.8 shows the distributions of fitted amplitudes from 1000 datasets generated with and without an injected sinusoidal signal of amplitude $A = 10^{-16}$, for both the continuous case and two gapped cases (55 and 75% missing data). In all three subplots, grey histograms represent

the results of the fits on the datasets without an injected signal, while the pink histograms show results with the injected signal.

In both cases, the distribution of the datasets with the injected signal is shifted relative to the noise only distribution, and the mean fitted amplitude closely matches the injected value. In panel (b), with a total of $\sim 55\%$ of the combined clock datasets missing, the injected signal is still detectable, although the distributions show an increased spread, as expected due to the gaps. Vertical dashed lines indicate the mean fitted amplitude in each case.

To further explore the effect of gaps and the amplitude of the injected signal on the recovery of the signal, the mean fitted amplitude against the injected amplitude is plotted in Figure 5.9 for all the missing data percentages tested. These results demonstrate that even with a significant amount of missing data, the fitting procedure remains sensitive to larger to moderate amplitude injected signals.

In the absence of a signal (zero amplitude), the fitted mean amplitude is close to zero but varies for each gap percentage. Figure 5.10 examines the case where no signal was injected, plotting the fitted amplitude as a function of gap percentage. This serves as a baseline for assessing the model's susceptibility to overfitting or noise-driven artefacts in the absence of a signal. Although these values differ, they are all within one order of magnitude and much smaller than the standard deviation of their respective distributions ($\sim 10^{-17}$), suggesting no signal detection. The small difference in the mean amplitude could indicate a bias in the fitting procedure caused by the gaps.

Figure 5.11 shows how the standard deviation of the fitted amplitude varies with increasing gap percentage. This provides a measure of the fitting uncertainty, which is expected to increase as more data points are removed from the analysis. The broader distribution

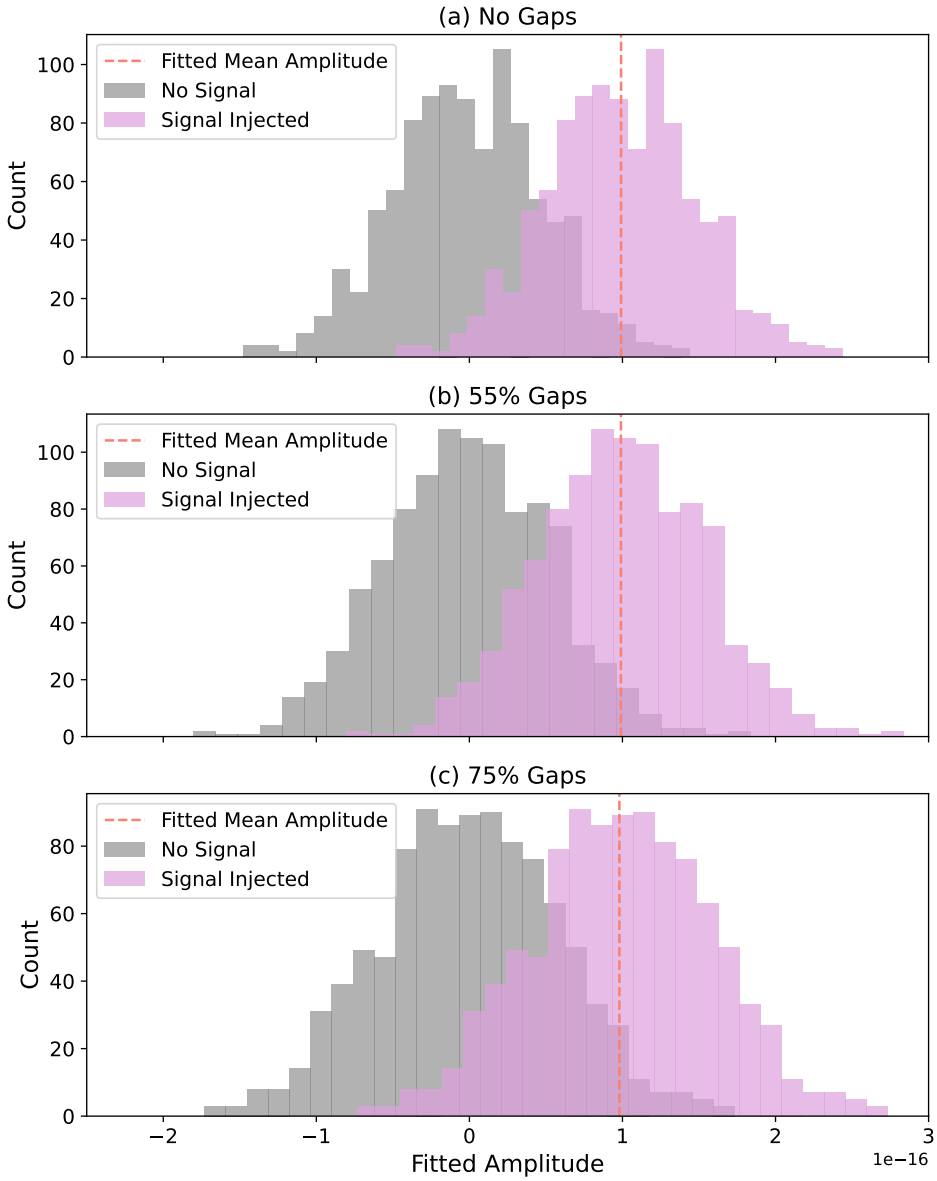

Figure 5.8: Comparison of fitted amplitude distributions with and without an injected signal, for datasets without gaps (top) and with gaps (bottom). Each panel shows the histogram of fitted amplitudes from 1000 noise-only datasets ("No Signal") and 1000 datasets with an injected sinusoidal signal of amplitude $A = 10^{-16}$. Vertical dashed lines indicate the mean fitted amplitude for each signal-injected distribution. The presence of the signal results in a shift of the distribution with a mean very close to the injected signal amplitude for both cases, proving successful signal recovery even with a large amount and duration of gaps in the datasets.

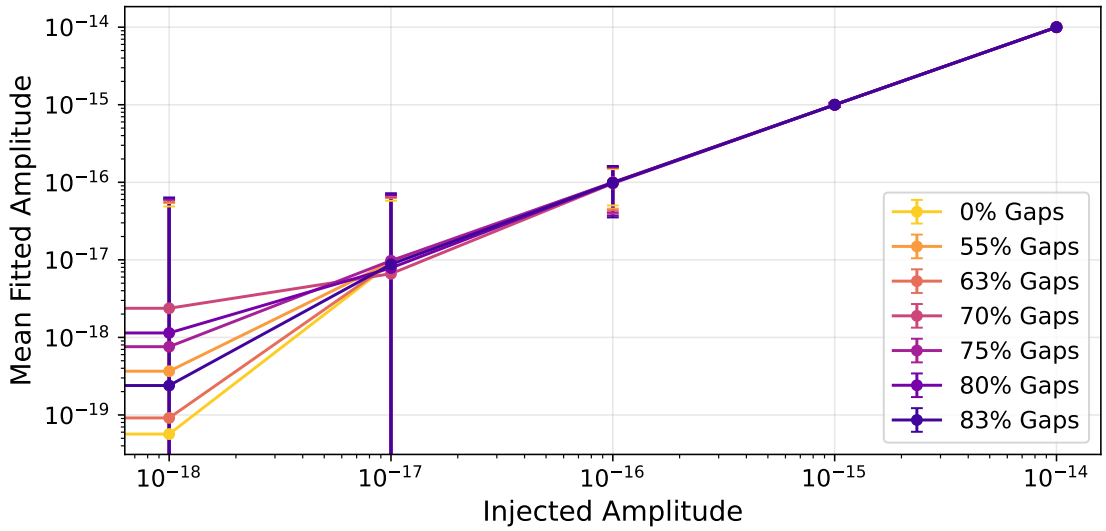

Figure 5.9: Log–log plot showing the relationship between injected and fitted amplitudes for varying levels of artificially introduced data gaps. Each line represents the mean fitted amplitude recovered by fitting a sinusoidal signal of unknown amplitude and a one-year period after injecting sinusoidal signals of different amplitudes into datasets with specified percentages of data missing. The 0% Gaps line represents the datasets without gaps, while higher percentages correspond to increased data reduction (55%–83% of data missing). The error bars correspond to the standard deviation of the distribution of the fitted amplitudes.

in the gapped case indicates a larger uncertainty in signal recovery, which is expected due to the missing data. The standard deviation sets the constraint on the magnitude of the signal that can be detected with the given atomic clocks, as it depends on the noise levels in the datasets. As this specific part of the analysis does not focus on the constraints set we will focus on the comparison between the gaps and no gaps scenarios.

When non-zero amplitude signals are injected, the mean of the fitted amplitudes converges to the true injected amplitude in the higher-amplitude cases (down to approximately 10^{-16}). As expected, increasing the injected amplitude improves the signal-to-noise ratio, resulting in more accurate recovery by the fitting procedure. In particular, for injected amplitudes of 10^{-14}, 10^{-15}, and 10^{-16}, the mean fitted amplitudes obtained from

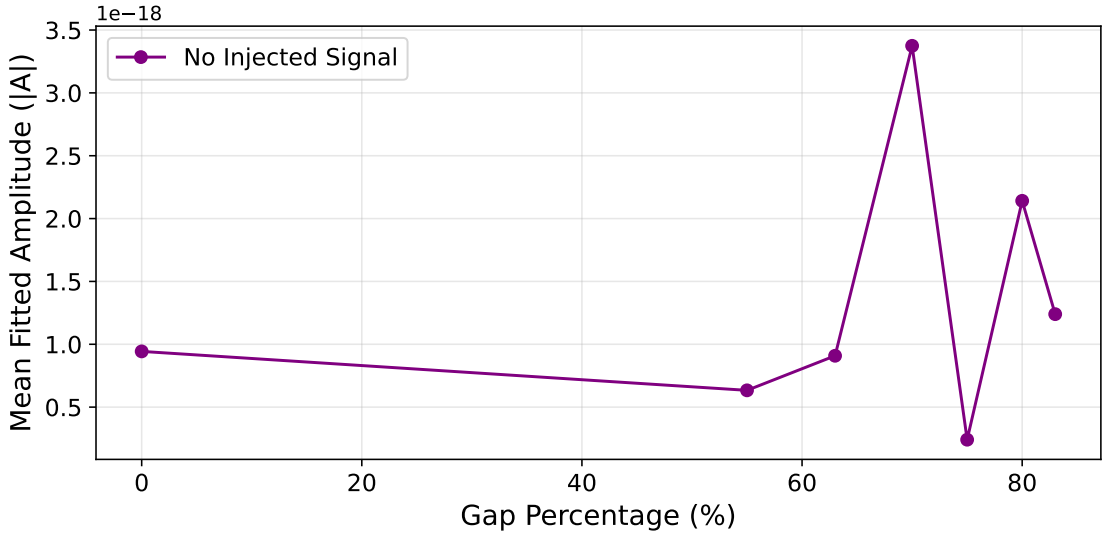

Figure 5.10: Mean fitted amplitude in the absence of an injected signal, shown for each tested gap percentage.

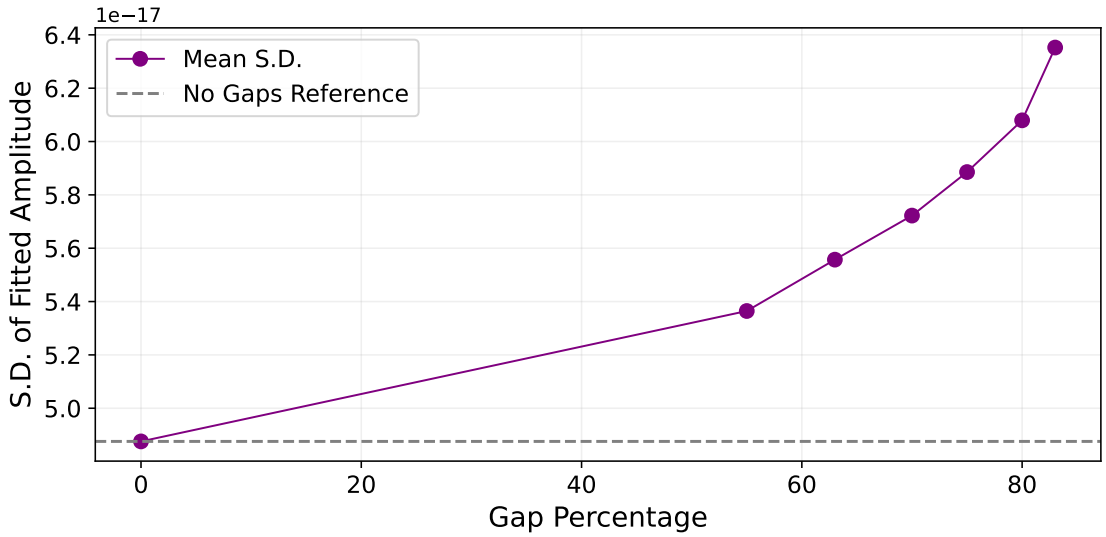

Figure 5.11: Standard deviation of fitted amplitudes across varying levels of missing data. As expected, the variability increases with gap percentage, indicating reduced robustness of the curve fitting as the data spread increases.

the gapped datasets closely match those from the datasets without missing values. This suggests that, within this range, the presence of data gaps does not significantly compromise the signal recovery process.

However, as the injected signal amplitude decreases, the mean recovered amplitudes approach the level of the fitting uncertainty (with a standard deviation at the order of 10^{-17}). This trend is evident in Figure 5.9, where the error bars become increasingly large as the injected amplitude gets smaller. At the 10^{-17} level, deviations between the fitted and true amplitudes can be observed, indicating a breakdown in the ability to recover the injected signal. At the 10^{-18} amplitude level, the signal is effectively buried within the noise, and the recovery fails across all gap conditions, including the case with no missing data. The fitted amplitudes at this level exhibit high variability and no agreement with the injected amplitude, highlighting the limitations of the method when the signal amplitude falls below the standard deviation of the noise.

It should be noted that this analysis is intended as a preliminary study and presents limitations. Although the method used for generating the gaps in this analysis was deemed the best out of the ones trialled, it might not capture the full range of scenarios encountered in real world datasets. Given more time, the study could be expanded to include a comparison of multiple gap-generation methods, including varying gap durations and distributions. Furthermore, due to the nature of the signal model (a sinusoidal signal with a one-year period) and the dataset duration (three years), it is possible that the method of gap generation happened to be relatively robust for this specific case. The combination of sampling rate and dataset length may have allowed sufficient signal coverage despite the missing data. Future studies could investigate the impact of different dataset durations and sampling rates on signal recovery, especially in scenarios where the signal period is closer to the dataset length or less than that.

5.7 Conclusions

Atomic clocks are powerful tools for testing theories involving modified gravity, dark energy, and dark matter by measuring time-dependent changes in fundamental constants like the proton-to-electron mass ratio (μ). Modern atomic clocks have reached an uncertainty of as low as one part in 10^{19}, allowing for the possibility of probing these fundamental constant variations and discovering new physics beyond the Standard Model.

In this chapter, we highlighted several theories that couple differently to protons and electrons, leading to variations in μ. These couplings cause variations in the atoms' transition frequencies, which clocks are sensitive to. The signals, coming from fundamental physics, generally manifest as either a linear drift or sinusoidal oscillations in μ.

A preliminary analysis was conducted using publicly available data from the BIPM Circular T database. As expected, the Circular T constraints were generally sub-leading compared to existing constraints for the theories under investigation. This work also presented forecasts of the sensitivity of state-of-the-art atomic clocks using the Fisher matrix calculation and an MCMC-based analysis pipeline that utilises simulated data.

This simulated signal was then used to project constraints on a range of fundamental physics theories, highlighting classes of theories where atomic clocks would significantly improve upon existing constraints. Those improvements are most profound for dynamical dark energy and dark matter theories. For modified gravity theories, we find an improvement over MICROSCOPE bounds provided that the fifth force falls off more slowly than $1/r^2$. In this case bounds from lunar laser ranging are currently stronger still, although this situation may change as atomic clock measurements improve.

The analysis framework has been turned into a publicly available tool that can be used

by clock operators and researchers to test their clocks' sensitivity to the different theoretical models. The tool enhances the ability to test various models and plan for future experiments. It can also be used to investigate the effects of different clock characteristics, including the level of noise of the clocks, on the ability to detect or further constrain new physics signals. It also presents the possibility to compare the effects of different noise components to allow for informed decision-making in experimental design. This is important for e.g. detecting these fundamental physics signals by taking specific steps to suppress the noise.

Improvements in atomic clock precision and data coverage and quality could significantly enhance the search for time-varying signals of new physics. For the detection of modified gravity signals where it is hypothesised that the period of oscillation is one year, one would need a dataset spanning at least 2-3 years. Gaps in the data (which are common in current datasets from clocks) also cause a limitation when turning to data analysis tools to infer the presence of a signal. The analysis framework presented is, therefore, a good starting point for testing the capabilities of different atomic clocks and motivating the need for atomic clock readouts that are continuous and as precise and accurate as possible.

In this work, we focused on deriving projected constraints from optical, microwave and molecular clock transition combinations with a focus on the combinations that produce the best constraints in time-dependent variations of μ. As technology progresses and new technological platforms for the development of clocks are explored, new types of clocks have surfaced that have increased sensitivity to time-dependent variations of α. Highly charged ion (HCI) clocks such as the californium ion clocks (Cf^{15+} and Cf^{17+}) [230, 231] have emerged as excellent candidates for searching for variations in α due to their high sensitivities ($K_\alpha = 47$ and $K_\alpha = -43.5$ respectively [159]), long excited clock transition lifetimes and their convenient optical transition frequencies [232, 233].

Another promising candidate for detecting α-variations is nuclear clocks [234, 235, 163]. Significant progress has been made in the development of a Thorium-229 nuclear clock [236]. This nuclear transition has an enhanced sensitivity to temporal variations of α with an enhancement factor for α variation of $-(0.82 \pm 0.25) \times 10^4$ [237] and a projected fractional instability of $\sim 10^{-19}$ [238, 239]. The analysis could be extended to variations of α and include these different species of atomic clocks in the future.

In future work, it would be interesting to analyze the capabilities of atomic clock pairs in a highly elliptical orbit around the Earth or Sun. Such a configuration would produce much stronger local variations to atomic frequencies from theories of modified gravity, and would also enable the possibility to map the modified gravity force as a function of distance from the Sun. In the future, it would also be interesting to connect the dark energy bound to specific models of dark energy, along with the bounds of the cosmological variation of particle masses. Additionally, there is the possibility of searching for multiple phenomenological signals present together in the clock measurement datastream. In this case, one could exploit the different time dependence of the signals to disentangle their contributions and perform a parameter estimation on the full set of parameters for all three signals. For the three phenomenological signals considered in this work, a full reconstruction of all the parameter space is possible[5], as the signals have a very different time dependence (which is even more different in the frequency domain) and their individual effect can therefore be disentangled. Given that, we expect that the uncertainty in the reconstruction of all the parameters is expected to be slightly worse than the individual constraints of the present work, while constraining all three phenomenological models simultaneously.

[5] With one caveat: if the frequency and phase of the dark matter modulation are close to the period and phase of the modified gravity effect due to the Earth's motion around the Sun, the two signals are degenerate and their disentanglement would be virtually impossible.

The gap analysis indicated that a reduction of up to approximately 83% of the data due to the introduction of gaps does not significantly affect the recovery of the sinusoidal signal with a period of one year for larger amplitude signals. This analysis demonstrates that the curve fitting method is capable of reliably recovering injected sinusoidal signals down to amplitudes on the order of 10^{-16}, even in the presence of substantial missing data. The accuracy of the signal is primarily dictated by the signal-to-noise ratio rather than the presence of gaps, provided the signal amplitude remains sufficiently large. As the amplitude approaches the level of the standard deviation $\sim 10^{-17}$, the method's ability to resolve the signal begins to degrade. Below this threshold, particularly at 10^{-18}, the injected signal becomes indistinguishable from noise, and the fitted amplitudes exhibit high variance and poor agreement with the true values. These results highlight a clear detection limit for the fitting method and demonstrate its robustness to missing data—within reason—up to moderate gap percentages. Accurate signal detection, therefore, depends more critically on signal strength relative to noise than on continuity of data for this particular model.

In future work, it would be interesting to investigate the impact of gaps on the detection of other signal types, including linear drifts and sinusoidal signals with different periods. It should also be noted that the noise correlation in the time domain has not been taken into account in this analysis. Ideally, a larger number of toy datasets (on the order of 10^4) would also have been generated to strengthen the statistical robustness of the results; however, this was not feasible due to hardware limitations, particularly in terms of CPU power and memory.

5.8 My Contributions

This collaborative project was led by Benjamin Elder, Giorgio Mentasti and me in collaboration and with guidance from Charles F. A. Baynham, Oliver Buchmueller, Carlo R. Contaldi, Claudia de Rham, Richard Hobson, Andrew J. Tolley. I contributed to the methodology, results, and interpretation of the study and led the experimental aspects, beginning with the understanding and mapping of atomic clock frequency ratios to variations in fundamental constants, and extending to the modelling of clock noise. I curated the Circular T dataset and implemented the analysis on this data. I also contributed to the development of the forecasting tool used to simulate atomic clock data streams and extract constraints on time-varying fundamental constants. In addition, I wrote key parts of the paper that this chapter is based on (Ref. [3]) as one of the first three coauthors. The gap analysis presented in Section 5.6 is original work undertaken independently by me and was not included in the paper.

Chapter 6

Conclusion

The work presented in this thesis contributes to the interdisciplinary efforts that lay the groundwork for future quantum sensing experiments, including the AION project, and atomic clock-based searches for new physics.

The AION project presented in Chapter 2 is a collaborative project between atomic physicists and theoretical physicists aimed at using atom interferometry for the detection of ULDM and gravitational waves in the mid-frequency range. In realising such a detector, one of the most important aspects is the production of ultra-cold atoms generated by laser cooling and magneto-optical trapping, techniques that are presented in Chapter 4.

In the early stages of this PhD, I contributed to the AION R&D efforts, working on experimental efforts and setting up the ultra-cold atom lab at Imperial College London. My work focused on setting up the red MOT system for cooling strontium atoms, which achieved sub-μK temperatures as presented in Chapters 3 and 4. This was a key technical milestone for the AION collaboration, and marked a significant step toward realising quantum sensors capable of detecting gravitational waves and ultra-light dark matter. This

work laid the foundation for the development of a prototype atom interferometer and spin squeezing experiments in the future.

The second part of my PhD, the work which is presented in Chapter 5 focused on a collaborative project between experimental physicists and theoretical physicists exploring the use of atomic clocks as sensitive detectors of time-dependent variations in fundamental constants, particularly the proton-to-electron mass ratio μ. We developed a simulation-based forecast framework. The results demonstrate that the clock comparisons tested with our framework place competitive constraints on theories of dark matter, dark energy, and modified gravity and guide the direction of future clock experiments for fundamental physics. Importantly, the analysis pipeline has been made publicly available to enable reproducible, collaborative progress in the field.

Finally, a study examining the effect of temporal gaps in clock data on the recovery of injected sinusoidal signals has been carried out. Using simulated datasets, we found that sinusoidal signals with amplitudes $\geq 10^{-16}$ and a one-year period could be accurately recovered even in the presence of significant temporal gaps (up to 83%). This provides valuable insight into the robustness of signal recovery analysis. However, as the injected amplitude approaches the noise level (around 10^{-17}), the accuracy of signal recovery begins to degrade, and at 10^{-18}, reliable detection is no longer possible, regardless of data completeness. It also highlights key directions for future work, including testing broader signal types and scaling up simulations for statistical robustness.

Looking forward, promising directions of the work presented in the latter part of this thesis, concerning atomic clocks, include extending sensitivity forecasts to models predicting variations in the fine-structure constant α, incorporating new species such as highly charged ions and nuclear clocks, and exploring configurations such as elliptical orbits to

amplify theoretical signatures. In parallel, continued improvements in data quality, noise reduction, and clock network coordination will be essential to fully realize the potential of atomic clocks in fundamental physics.

Collectively, this work contributes both to the experimental advancement of atom interferometer technologies and to the theoretical and statistical frameworks needed to test fundamental physics with atomic clocks. The results underscore the growing potential of quantum sensing in probing beyond-Standard-Model phenomena.

Looking ahead, the AION project will continue toward contributing to the realisation of large-baseline atom interferometers capable of probing ultra-light dark matter and mid-frequency gravitational waves. The 10-metre baseline detector is already in the planning phase, marking a critical step in the AION project. Such large-scale detectors, and especially those in the subsequent stages of the project, require a large collaboration of multi-disciplinary expertise. Therefore, collaboration with the MAGIS experiment in the United States, as well as other long-baseline efforts, presents an exciting opportunity to establish a global network of quantum sensors with complementary capabilities.

In parallel, atomic and molecular clock experiments will benefit from improvements in frequency stability, experimental design, and noise characterisation. These developments will enhance sensitivity to time-varying signals predicted by dark matter, dark energy, and other fundamental physics models. As new clock species, such as molecular and nuclear clocks, are developed and deployed, the potential to explore previously inaccessible regions of parameter space will continue to grow. Together, long-baseline atom interferometry experiments, such as the one proposed by AION, and clock-based experiments form a complementary and powerful set of precision tools for exploring new physics beyond the Standard Model.

Bibliography

[1] B. Stray et al. “Centralized design and production of the ultra-high vacuum and laser-stabilization systems for the AION ultra-cold strontium laboratories”. In: *AVS Quantum Science* 6.1 (Mar. 2024), p. 014409. ISSN: 2639-0213. DOI: 10.1116/5.0172731. eprint: https://pubs.aip.org/avs/aqs/article-pdf/doi/10.1116/5.0172731/19750381/014409_1_5.0172731.pdf. URL: https://doi.org/10.1116/5.0172731.

[2] E. Pasatembou et al. “Progress toward ultra-cold Sr for the AION project—A red MOT and an optical-heterodyne diagnostic tool for injection-locked laser diodes”. In: *AVS Quantum Science* 6.1 (Mar. 2024), p. 014408. ISSN: 2639-0213. DOI: 10.1116/5.0180043. eprint: https://pubs.aip.org/avs/aqs/article-pdf/doi/10.1116/5.0180043/19728280/014408_1_5.0180043.pdf. URL: https://doi.org/10.1116/5.0180043.

[3] Benjamin Elder et al. “Prospects for detecting new dark physics with the next generation of atomic clocks”. In: *Phys. Rev. D* (July 2025). DOI: 10.1103/vghm-4s5p. URL: https://link.aps.org/doi/10.1103/vghm-4s5p.

[4] Planck Collaboration et al. “Planck 2015 results - XIV. Dark energy and modified gravity”. In: *A&A* 594 (2016). DOI: 10.1051/0004-6361/201525814. URL: https://doi.org/10.1051/0004-6361/201525814.

[5] Peter W. Graham, Jeremy Mardon, and Surjeet Rajendran. "Vector dark matter from inflationary fluctuations". In: *Phys. Rev. D* 93 (10 May 2016), p. 103520. DOI: 10.1103/PhysRevD.93.103520. URL: https://link.aps.org/doi/10.1103/PhysRevD.93.103520.

[6] Lam Hui et al. "Ultralight scalars as cosmological dark matter". In: *Phys. Rev. D* 95 (4 Feb. 2017), p. 043541. DOI: 10.1103/PhysRevD.95.043541. URL: https://link.aps.org/doi/10.1103/PhysRevD.95.043541.

[7] D. Antypas et al. "New Horizons: Scalar and Vector Ultralight Dark Matter". In: (Mar. 2022). arXiv: 2203.14915 [hep-ex].

[8] Thomas P. Sotiriou and Valerio Faraoni. "$f(R)$ theories of gravity". In: *Rev. Mod. Phys.* 82 (1 Mar. 2010), pp. 451–497. DOI: 10.1103/RevModPhys.82.451. URL: https://link.aps.org/doi/10.1103/RevModPhys.82.451.

[9] Claudia de Rham. "Massive Gravity". In: *Living Rev. Rel.* 17 (2014), p. 7. DOI: 10.12942/lrr-2014-7. arXiv: 1401.4173 [hep-th].

[10] Marco Battaglieri et al. "US Cosmic Visions: New Ideas in Dark Matter 2017: Community Report". In: *U.S. Cosmic Visions: New Ideas in Dark Matter*. July 2017. arXiv: 1707.04591 [hep-ph].

[11] David J. E. Marsh. "Axion Cosmology". In: *Phys. Rept.* 643 (2016), pp. 1–79. DOI: 10.1016/j.physrep.2016.06.005. arXiv: 1510.07633 [astro-ph.CO].

[12] Claudia de Rham and Andrew J. Tolley. "The Encyclopedia of Cosmology: Volume 1: Modified Gravity". In: *The Encyclopedia of Cosmology*. Ed. by Giovanni G. Fazi. World Scientific, Nov. 2023. DOI: 10.1142/13578-vol1.

[13] Vera C. Rubin and W. Kent Ford Jr. "Rotation of the Andromeda Nebula from a Spectroscopic Survey of Emission Regions". In: 159 (Feb. 1970), p. 379. DOI: 10.1086/150317.

[14] Yoshiaki Sofue and Vera Rubin. "Rotation Curves of Spiral Galaxies". In: 39 (Jan. 2001), pp. 137–174. DOI: 10.1146/annurev.astro.39.1.137. arXiv: astro-ph/0010594 [astro-ph].

[15] Douglas Clowe et al. “A Direct Empirical Proof of the Existence of Dark Matter*”. In: *The Astrophysical Journal* 648.2 (Aug. 2006), p. L109. DOI: 10.1086/508162. URL: https://dx.doi.org/10.1086/508162.

[16] N. Aghanim et al. “Planck 2018 results. VI. Cosmological parameters”. In: *Astron. Astrophys.* 641 (2020). [Erratum: Astron.Astrophys. 652, C4 (2021)], A6. DOI: 10.1051/0004-6361/201833910. arXiv: 1807.06209 [astro-ph.CO].

[17] F. Zwicky. “On the Masses of Nebulae and of Clusters of Nebulae”. In: 86 (Oct. 1937), p. 217. DOI: 10.1086/143864.

[18] Georges Aad et al. “Search for supersymmetry in final states with missing transverse momentum and three or more b-jets in 139 fb^{-1} of proton–proton collisions at $\sqrt{s} =$ 13 TeV with the ATLAS detector”. In: *Eur. Phys. J. C* 83.7 (2023), p. 561. DOI: 10.1140/epjc/s10052-023-11543-6. arXiv: 2211.08028 [hep-ex].

[19] Armen Tumasyan et al. “Search for top squarks in the four-body decay mode with single lepton final states in proton-proton collisions at $\sqrt{s} = 13$ TeV”. In: *Journal of High Energy Physics* 2023.6 (2023), pp. 1–51.

[20] J. Aalbers et al. “First Dark Matter Search Results from the LUX-ZEPLIN (LZ) Experiment”. In: *Phys. Rev. Lett.* 131 (4 July 2023), p. 041002. DOI: 10.1103/PhysRevLett.131.041002. URL: https://link.aps.org/doi/10.1103/PhysRevLett.131.041002.

[21] Gianfranco Bertone and Dan Hooper. “History of dark matter”. In: *Rev. Mod. Phys.* 90 (4 Oct. 2018), p. 045002. DOI: 10.1103/RevModPhys.90.045002. URL: https://link.aps.org/doi/10.1103/RevModPhys.90.045002.

[22] Lam Hui. “Wave Dark Matter”. In: *Annual Review of Astronomy and Astrophysics* 59 (2021), pp. 247–289. DOI: 10.1146/annurev-astro-120920-010024. URL: https://doi.org/10.1146/annurev-astro-120920-010024.

[23] Andrew A. Geraci and Andrei Derevianko. “Sensitivity of Atom Interferometry to Ultralight Scalar Field Dark Matter”. In: *Physical Review Letters* 117 (26 Dec. 2016). ISSN: 10797114. DOI: 10.1103/PhysRevLett.117.261301.

[24] Asimina Arvanitaki et al. “Search for light scalar dark matter with atomic gravitational wave detectors”. In: *Phys. Rev. D* 97 (7 Apr. 2018), p. 075020. DOI: 10.1103/PhysRevD.97.075020. URL: https://link.aps.org/doi/10.1103/PhysRevD.97.075020.

[25] Peter W. Graham et al. “A New method for gravitational wave detection with atomic sensors”. In: *Physical Review Letters* 110 (17 Apr. 2013). ISSN: 00319007. DOI: 10.1103/PhysRevLett.110.171102.

[26] LIGO collaboration, J. Aasi, et al. “Advanced LIGO”. In: *Classical and Quantum Gravity* 32 (7 Apr. 2015). ISSN: 13616382. DOI: 10.1088/0264-9381/32/7/074001.

[27] VIRGO collaboration, F. Acernese, et al. “Advanced Virgo: A second-generation interferometric gravitational wave detector”. In: *Classical and Quantum Gravity* 32 (2 Jan. 2015). ISSN: 13616382. DOI: 10.1088/0264-9381/32/2/024001.

[28] B. P. Abbott et al. “Observation of Gravitational Waves from a Binary Black Hole Merger”. In: *Phys. Rev. Lett.* 116 (6 Feb. 2016), p. 061102. DOI: 10.1103/PhysRevLett.116.061102. URL: https://link.aps.org/doi/10.1103/PhysRevLett.116.061102.

[29] B. P. Abbott et al. “GW170817: Observation of Gravitational Waves from a Binary Neutron Star Inspiral”. In: *Phys. Rev. Lett.* 119 (16 Oct. 2017), p. 161101. DOI: 10.1103/PhysRevLett.119.161101. URL: https://link.aps.org/doi/10.1103/PhysRevLett.119.161101.

[30] Pau Amaro-Seoane et al. *Laser Interferometer Space Antenna*. 2017. arXiv: 1702.00786 [astro-ph.IM]. URL: https://arxiv.org/abs/1702.00786.

[31] Adeela Afzal et al. “The NANOGrav 15 yr Data Set: Search for Signals from New Physics”. In: *Astrophys. J. Lett.* 951.1 (2023). [Erratum: Astrophys.J.Lett. 971, L27 (2024), Erratum: Astrophys.J. 971, L27 (2024)], p. L11. DOI: 10.3847/2041-8213/acdc91. arXiv: 2306.16219 [astro-ph.HE].

[32] Jenny E. Greene, Jay Strader, and Luis C. Ho. “Intermediate-Mass Black Holes”. In: 58 (Aug. 2020), pp. 257–312. DOI: 10.1146/annurev-astro-032620-021835. arXiv: 1911.09678 [astro-ph.GA].

[33] Manuel Arca Sedda et al. “The missing link in gravitational-wave astronomy: discoveries waiting in the decihertz range”. In: *Classical and Quantum Gravity* 37.21 (2020), p. 215011.

[34] Miao Li et al. “Dark Energy: A Brief Review”. In: *Front. Phys. (Beijing)* 8 (2013), pp. 828–846. DOI: 10.1007/s11467-013-0300-5. arXiv: 1209.0922 [astro-ph.CO].

[35] Shinji Tsujikawa. “Quintessence: A Review”. In: *Class. Quant. Grav.* 30 (2013), p. 214003. DOI: 10.1088/0264-9381/30/21/214003. arXiv: 1304.1961 [gr-qc].

[36] Werner Heisenberg. “Über quantentheoretische Umdeutung kinematischer und mechanischer Beziehungen”. In: *Zeitschrift für Physik* 33.1 (1925), pp. 879–893. ISSN: 0044-3328. DOI: 10.1007/BF01328377. URL: https://doi.org/10.1007/BF01328377.

[37] Norman F. Ramsey. “A Molecular Beam Resonance Method with Separated Oscillating Fields”. In: *Phys. Rev.* 78 (6 June 1950), pp. 695–699. DOI: 10.1103/PhysRev.78.695. URL: https://link.aps.org/doi/10.1103/PhysRev.78.695.

[38] Andrew D. Ludlow et al. “Optical atomic clocks”. In: *Rev. Mod. Phys.* 87 (2 May 2015), pp. 637–701. DOI: 10.1103/RevModPhys.87.637. URL: https://link.aps.org/doi/10.1103/RevModPhys.87.637.

[39] Alexander D. Cronin, Jörg Schmiedmayer, and David E. Pritchard. “Optics and interferometry with atoms and molecules”. In: *Rev. Mod. Phys.* 81 (3 July 2009), pp. 1051–1129. DOI: 10.1103/RevModPhys.81.1051. URL: https://link.aps.org/doi/10.1103/RevModPhys.81.1051.

[40] Sven Abend et al. *Terrestrial very-long-baseline atom interferometry: Workshop summary*. June 2024. DOI: 10.1116/5.0185291.

[41] A. Abdalla, M. Abe, S. Abend, et al. “Terrestrial Very-Long-Baseline Atom Interferometry: Summary of the Second Workshop”. In: *EPJ Quantum Technology* 12 (2025), p. 42.

DOI: 10.1140/epjqt/s40507-025-00344-3. URL: https://doi.org/10.1140/epjqt/s40507-025-00344-3.

[42] Regulatory Horizons Council. *Regulating Quantum Technology Applications*. https://www.gov.uk/government/publications/regulatory-horizons-council-regulating-quantum-technology-applications. Accessed: 2025-06-29. 2024.

[43] Regulatory Horizons Council. *The Future Regulation of Space Technologies*. https://www.gov.uk/government/publications/regulatory-horizons-council-the-future-regulation-of-space-technologies. Accessed: 2025-06-29. 2024.

[44] Seb Wilkes and Simon Brawley. *Quantum computing, sensing and communications*. POSTnote 742, UK Parliamentary Office of Science and Technology. Accessed: 2025-06-29. Apr. 2025. DOI: 10.58248/PN742. URL: https://post.parliament.uk/research-briefings/post-pn-0742/.

[45] Mark Kasevich and Steven Chu. *Atomic Interferometry Using Stimulated Raman Transitions*. 1991.

[46] M Kasevich and S Chu. *Applied physics Physics B Chemistry Measurement of the Gravitational Acceleration of an Atom with a Light-Pulse Atom Interferometer*. 1992.

[47] Frank A. Narducci, Adam T. Black, and John H. Burke. "Advances toward fieldable atom interferometers". In: *Advances in Physics: X* 7 (1 2022). ISSN: 23746149. DOI: 10.1080/23746149.2021.1946426.

[48] Achim Peters, Keng Yeow Chung, and Steven Chu. "Measurement of gravitational acceleration by dropping atoms". In: *Nature* 400.6747 (1999), pp. 849–852. DOI: 10.1038/23655.

[49] Zhong Kun Hu et al. "Demonstration of an ultrahigh-sensitivity atom-interferometry absolute gravimeter". In: *Physical Review A - Atomic, Molecular, and Optical Physics* 88 (4 Oct. 2013). ISSN: 10502947. DOI: 10.1103/PhysRevA.88.043610.

[50] J. M. Mc Guirk et al. “Sensitive absolute-gravity gradiometry using atom interferometry”. In: *Physical Review A - Atomic, Molecular, and Optical Physics* 65 (3 2002), pp. 1–14. ISSN: 10502947. DOI: 10.1103/PhysRevA.65.033608.

[51] G. Lamporesi et al. “Determination of the newtonian gravitational constant using atom interferometry”. In: *Physical Review Letters* 100 (5 Feb. 2008). ISSN: 00319007. DOI: 10.1103/PhysRevLett.100.050801.

[52] T. L. Gustavson, P. Bouyer, and M. A. Kasevich. “Precision Rotation Measurements with an Atom Interferometer Gyroscope”. In: *Phys. Rev. Lett.* 78 (11 Mar. 1997), pp. 2046–2049. DOI: 10.1103/PhysRevLett.78.2046. URL: https://link.aps.org/doi/10.1103/PhysRevLett.78.2046.

[53] B. Dubetsky and M. A. Kasevich. “Atom interferometer as a selective sensor of rotation or gravity”. In: *Physical Review A - Atomic, Molecular, and Optical Physics* 74 (2 2006). ISSN: 10502947. DOI: 10.1103/PhysRevA.74.023615.

[54] L. Badurina et al. “AION: An atom interferometer observatory and network”. In: *Journal of Cosmology and Astroparticle Physics* 2020 (May 2020). DOI: 10.1088/1475-7516/2020/05/011.

[55] G. W. Biedermann et al. “Testing gravity with cold-atom interferometers”. In: *Phys. Rev. A* 91 (3 Mar. 2015), p. 033629. DOI: 10.1103/PhysRevA.91.033629. URL: https://link.aps.org/doi/10.1103/PhysRevA.91.033629.

[56] Brian Estey et al. “High-Resolution Atom Interferometers with Suppressed Diffraction Phases”. In: *Phys. Rev. Lett.* 115 (8 Aug. 2015), p. 083002. DOI: 10.1103/PhysRevLett.115.083002. URL: https://link.aps.org/doi/10.1103/PhysRevLett.115.083002.

[57] H. Müller et al. “A new photon recoil experiment: towards a determination of the fine structure constant”. In: *Applied Physics B* 84.4 (2006), pp. 633–642. DOI: 10.1007/s00340-006-2279-x. URL: https://doi.org/10.1007/s00340-006-2279-x.

[58] S Merlet et al. “Comparison between two mobile absolute gravimeters: optical versus atomic interferometers”. In: *Metrologia* 47.4 (June 2010), p. L9. DOI: 10.1088/0026-1394/47/4/L01. URL: https://dx.doi.org/10.1088/0026-1394/47/4/L01.

[59] Ken Van Tilburg et al. “Search for Ultralight Scalar Dark Matter with Atomic Spectroscopy”. In: *Phys. Rev. Lett.* 115 (1 June 2015), p. 011802. DOI: 10.1103/PhysRevLett.115.011802. URL: https://link.aps.org/doi/10.1103/PhysRevLett.115.011802.

[60] Benjamin Elder et al. “Chameleon dark energy and atom interferometry”. In: *Phys. Rev. D* 94 (4 Aug. 2016), p. 044051. DOI: 10.1103/PhysRevD.94.044051. URL: https://link.aps.org/doi/10.1103/PhysRevD.94.044051.

[61] Savas Dimopoulos et al. “Atomic gravitational wave interferometric sensor”. In: *Physical Review D - Particles, Fields, Gravitation and Cosmology* 78 (12 Dec. 2008). ISSN: 15507998. DOI: 10.1103/PhysRevD.78.122002.

[62] Savas Dimopoulos et al. “Gravitational wave detection with atom interferometry”. In: *Physics Letters B* 678.1 (2009), pp. 37–40. ISSN: 0370-2693. DOI: https://doi.org/10.1016/j.physletb.2009.06.011. URL: https://www.sciencedirect.com/science/article/pii/S0370269309006844.

[63] Gabriella Agazie et al. “The NANOGrav 15 yr Data Set: Evidence for a Gravitational-wave Background”. In: *The Astrophysical Journal Letters* 951 (1 July 2023), p. L8. ISSN: 2041-8205. DOI: 10.3847/2041-8213/acdac6.

[64] AEDGE collaboration, Y. A. El-Neaj, et al. “AEDGE: Atomic Experiment for Dark Matter and Gravity Exploration in Space”. In: *EPJ Quantum Technology* 7 (1 Dec. 2020). ISSN: 21960763. DOI: 10.1140/epjqt/s40507-020-0080-0.

[65] Peter W. Graham et al. *Mid-band gravitational wave detection with precision atomic sensors*. Nov. 2017. arXiv: 1711.02225 [astro-ph.IM].

[66] Jon Coleman. “Matter-wave Atomic Gradiometer Interferomentric Sensor (MAGIS-100) at Fermilab”. In: (2018). URL: http://arxiv.org/abs/1812.00482.

[67] Jan Rudolph et al. “Large Momentum Transfer Clock Atom Interferometry on the 689 nm Intercombination Line of Strontium”. In: *Phys. Rev. Lett.* 124 (8 Feb. 2020), p. 083604. DOI: 10.1103/PhysRevLett.124.083604. URL: https://link.aps.org/doi/10.1103/PhysRevLett.124.083604.

[68] M J Snadden et al. *Measurement of the Earth's Gravity Gradient with an Atom Interferometer-Based Gravity Gradiometer*. 1998.

[69] Alex Sugarbaker et al. “Enhanced Atom Interferometer Readout through the Application of Phase Shear”. In: *Phys. Rev. Lett.* 111 (11 Sept. 2013), p. 113002. DOI: 10.1103/PhysRevLett.111.113002. URL: https://link.aps.org/doi/10.1103/PhysRevLett.111.113002.

[70] Simon Stellmer, Rudolf Grimm, and Florian Schreck. “Production of quantum-degenerate strontium gases”. In: *Physical Review A - Atomic, Molecular, and Optical Physics* 87 (1 Jan. 2013). ISSN: 10502947. DOI: 10.1103/PhysRevA.87.013611.

[71] S. L. Campbell et al. “A Fermi-degenerate three-dimensional optical lattice clock”. In: *Science* 358.6359 (2017), pp. 90–94. DOI: 10.1126/science.aam5538. eprint: https://www.science.org/doi/pdf/10.1126/science.aam5538. URL: https://www.science.org/doi/abs/10.1126/science.aam5538.

[72] Liang Hu et al. “Atom Interferometry with the Sr Optical Clock Transition”. In: *Physical Review Letters* 119 (26 Dec. 2017). ISSN: 10797114. DOI: 10.1103/PhysRevLett.119.263601.

[73] Tomoya Akatsuka et al. “Three-stage laser cooling of Sr atoms using the 5s5p P2 3 metastable state below Doppler temperatures”. In: *Physical Review A* 103 (2 Feb. 2021). ISSN: 24699934. DOI: 10.1103/PhysRevA.103.023331.

[74] Hidetoshi Katori et al. “Magneto-optical trapping and cooling of strontium atoms down to the photon recoil temperature”. In: *Physical Review Letters* 82 (6 1999), pp. 1116–1119. ISSN: 10797114. DOI: 10.1103/PhysRevLett.82.1116.

[75] Takashi Mukaiyama et al. “Recoil-Limited Laser Cooling of 87Sr Atoms near the Fermi Temperature”. In: *Physical Review Letters* 90 (11 2003), p. 4. ISSN: 10797114. DOI: 10.1103/PhysRevLett.90.113002.

[76] Xinye Xu et al. “Cooling and trapping of atomic strontium”. In: *Journal of the Optical Society of America B Optical Physics* 20.5 (2003), pp. 968–976. DOI: 10.1364/JOSAB.20.000968.

[77] F. Sorrentino et al. “Laser cooling and trapping of atomic strontium for ultracold atoms physics, high-precision spectroscopy and quantum sensors”. In: *Modern Physics Letters B* 20 (21 Sept. 2006), pp. 1287–1320. ISSN: 02179849. DOI: 10.1142/S0217984906011682.

[78] Ingo Nosske et al. “Two-dimensional magneto-optical trap as a source for cold strontium atoms”. In: *Phys. Rev. A* 96 (5 Nov. 2017), p. 053415. DOI: 10.1103/PhysRevA.96.053415. URL: https://link.aps.org/doi/10.1103/PhysRevA.96.053415.

[79] Shayne Bennetts et al. “Steady-State Magneto-Optical Trap with 100-Fold Improved Phase-Space Density”. In: *Phys. Rev. Lett.* 119 (22 Dec. 2017), p. 223202. DOI: 10.1103/PhysRevLett.119.223202. URL: https://link.aps.org/doi/10.1103/PhysRevLett.119.223202.

[80] Matteo Barbiero et al. “Sideband-Enhanced Cold Atomic Source for Optical Clocks”. In: *Phys. Rev. Appl.* 13 (1 Jan. 2020), p. 014013. DOI: 10.1103/PhysRevApplied.13.014013. URL: https://link.aps.org/doi/10.1103/PhysRevApplied.13.014013.

[81] Jianing Li et al. “Bi-color atomic beam slower and magnetic field compensation for ultracold gases”. In: *AVS Quantum Science* 4.4 (Dec. 2022), p. 046801. ISSN: 2639-0213. DOI: 10.1116/5.0126745. URL: https://doi.org/10.1116/5.0126745.

[82] Thomas H. Loftus et al. “Narrow line cooling and momentum-space crystals”. In: *Physical Review A - Atomic, Molecular, and Optical Physics* 70 (6 Dec. 2004). ISSN: 10502947. DOI: 10.1103/PhysRevA.70.063413.

[83] Kwang-Hoon Ko et al. “Measurement of the isotope selectivity of the strontium magneto-optical trap by a time-of-flight mass spectrometer”. In: *J. Opt. Soc. Am. B* 23.12 (Dec.

2006), pp. 2465–2469. DOI: 10.1364/JOSAB.23.002465. URL: http://opg.optica.org/josab/abstract.cfm?URI=josab-23-12-2465.

[84] A. Lurio, M. Mandel, and R. Novick. "Second-Order Hyperfine and Zeeman Corrections for an (sl) Configuration". In: *Phys. Rev.* 126.5 (June 1962), pp. 1758–1767. DOI: 10.1103/PhysRev.126.1758. URL: https://link.aps.org/doi/10.1103/PhysRev.126.1758.

[85] Andrew Ludlow. "The Strontium Optical Lattice Clock: Optical Spectroscopy with Sub-Hertz Accuracy". PhD thesis. Boulder, Mar. 2008, p. 251.

[86] M. M. Boyd. "High Precision Spectroscopy of Strontium in an Optical Lattice: Towards a New Standard for Frequency and Time". PhD thesis. University of Colorado, 2007.

[87] Masao Takamoto and Hidetoshi Katori. "Spectroscopy of the $^1S_0 - ^3P_0$ Clock Transition of ^{87}Sr in an Optical Lattice". In: *Phys. Rev. Lett.* 91 (22 Nov. 2003), p. 223001. DOI: 10.1103/PhysRevLett.91.223001. URL: https://link.aps.org/doi/10.1103/PhysRevLett.91.223001.

[88] Paul D. Lett et al. "Observation of Atoms Laser Cooled below the Doppler Limit". In: *Phys. Rev. Lett.* 61 (2 July 1988), pp. 169–172. DOI: 10.1103/PhysRevLett.61.169. URL: https://link.aps.org/doi/10.1103/PhysRevLett.61.169.

[89] Jason M. Hogan, David M. S. Johnson, and Mark A. Kasevich. "Light-pulse atom interferometry". In: *arXiv* (June 2008). URL: http://arxiv.org/abs/0806.3261.

[90] Brenton Young, Mark Kasevich, and Steven Chu. "Precision Atom Interferometry with Light Pulses". In: *Atom Interferometry*. Ed. by Paul R. Berman. San Diego: Academic Press, 1997, pp. 363–406. ISBN: 978-0-12-092460-8. DOI: https://doi.org/10.1016/B978-012092460-8/50010-2. URL: https://www.sciencedirect.com/science/article/pii/B9780120924608500102.

[91] Sven Abend et al. "Atom interferometry and its applications". In: *arXiv* (Jan. 2020). Accessed: Month day, year. URL: http://arxiv.org/abs/2001.10976.

[92] Jörg Schmiedmayer et al. “Optics and Interferometry with Atoms and Molecules”. In: *Atom Interferometry*. Ed. by Paul R. Berman. San Diego: Academic Press, 1997, pp. 1–83. ISBN: 978-0-12-092460-8. DOI: https://doi.org/10.1016/B978-012092460-8/50002-3. URL: https://www.sciencedirect.com/science/article/pii/B9780120924608500023.

[93] Christian J. Bordé. “Matter-Wave Interferometers: A Synthetic Approach”. In: *Atom Interferometry*. Ed. by Paul R. Berman. San Diego: Academic Press, 1997, pp. 257–292. ISBN: 978-0-12-092460-8. DOI: https://doi.org/10.1016/B978-012092460-8/50008-4. URL: https://www.sciencedirect.com/science/article/pii/B9780120924608500084.

[94] Leonardo Badurina. “Ultralight Dark Matter Phenomenology at Atom Interferometers”. Accessed: 20 September 2024. PhD thesis. King’s College London, 2023. URL: https://kclpure.kcl.ac.uk/portal/en/studentTheses/ultralight-dark-matter-phenomenology-at-atom-interferometers.

[95] Luca Pezzè et al. “Quantum metrology with nonclassical states of atomic ensembles”. In: *Reviews of Modern Physics* 90 (3 Sept. 2018). ISSN: 15390756. DOI: 10.1103/RevModPhys.90.035005.

[96] Nan Yu and Massimo Tinto. “Gravitational wave detection with single-laser atom interferometers”. In: *General Relativity and Gravitation* 43 (7 July 2011), pp. 1943–1952. ISSN: 00017701. DOI: 10.1007/s10714-010-1055-8.

[97] Liang Hu et al. “Sr atom interferometry with the optical clock transition as a gravimeter and a gravity gradiometer”. In: (July 2019). DOI: 10.1088/1361-6382/ab4d18. URL: http://arxiv.org/abs/1907.10537%20http://dx.doi.org/10.1088/1361-6382/ab4d18.

[98] Jason Michael Hogan. “Towards Precision Tests of General Relativity Using an Atom Interferometer”. English. Ph.D. thesis, electronic resource; 1 online resource. PhD thesis.

Stanford University, Department of Physics, 2010. URL: https://purl.stanford.edu/cf210zm6017.

[99] Asimina Arvanitaki et al. "Search for light scalar dark matter with atomic gravitational wave detectors". In: *Physical Review D* 97 (7 Apr. 2018). ISSN: 24700029. DOI: 10.1103/PhysRevD.97.075020.

[100] Jenny E. Greene, Jay Strader, and Luis C. Ho. "Intermediate-Mass Black Holes". In: *Annual Review of Astronomy and Astrophysics* 58.1 (Aug. 2020), pp. 257–312. ISSN: 1545-4282. DOI: 10.1146/annurev-astro-032620-021835. URL: http://dx.doi.org/10.1146/annurev-astro-032620-021835.

[101] Thibault Damour and John F. Donoghue. "Phenomenology of the equivalence principle with light scalars". In: *Classical and Quantum Gravity* 27 (20 Oct. 2010). ISSN: 02649381. DOI: 10.1088/0264-9381/27/20/202001.

[102] Thibault Damour and John F. Donoghue. "Equivalence principle violations and couplings of a light dilaton". In: *Physical Review D - Particles, Fields, Gravitation and Cosmology* 82 (8 Oct. 2010). ISSN: 15507998. DOI: 10.1103/PhysRevD.82.084033.

[103] T. A. Wagner et al. "Torsion-balance tests of the weak equivalence principle". In: *Classical and Quantum Gravity* 29 (18 Sept. 2012). ISSN: 02649381. DOI: 10.1088/0264-9381/29/18/184002.

[104] A. Hees et al. "Searching for an Oscillating Massive Scalar Field as a Dark Matter Candidate Using Atomic Hyperfine Frequency Comparisons". In: *Physical Review Letters* 117 (6 Aug. 2016). ISSN: 10797114. DOI: 10.1103/PhysRevLett.117.061301.

[105] Joel Bergé et al. "MICROSCOPE Mission: First Constraints on the Violation of the Weak Equivalence Principle by a Light Scalar Dilaton". In: *Physical Review Letters* 120 (14 Apr. 2018). ISSN: 10797114. DOI: 10.1103/PhysRevLett.120.141101.

[106] John Ellis Oliver Buchmueller and Ulrich Schneider. "Large-scale atom interferometry for fundamental physics". In: *Contemporary Physics* 64.2 (2023), pp. 93–110. DOI: 10.

1080/00107514.2023.2239008. eprint: https://doi.org/10.1080/00107514.2023.2239008. URL: https://doi.org/10.1080/00107514.2023.2239008.

[107] D. Schlippert et al. "Matter-Wave Interferometry for Inertial Sensing and Tests of Fundamental Physics". In: *CPT and Lorentz Symmetry*. WORLD SCIENTIFIC, 2019, pp. 37–40. DOI: 10.1142/9789811213984_0010. eprint: https://www.worldscientific.com/doi/pdf/10.1142/9789811213984_0010. URL: https://www.worldscientific.com/doi/abs/10.1142/9789811213984_0010.

[108] L. Zhou et al. "Development of an atom gravimeter and status of the 10-meter atom interferometer for precision gravity measurement". In: *General Relativity and Gravitation* 43 (7 July 2011), pp. 1931–1942. ISSN: 00017701. DOI: 10.1007/s10714-011-1167-9.

[109] B. Canuel et al. "Exploring gravity with the MIGA large scale atom interferometer". In: *Scientific Reports* 8 (1 Dec. 2018). ISSN: 20452322. DOI: 10.1038/s41598-018-32165-z.

[110] Ming-Sheng Zhan et al. "ZAIGA: Zhaoshan long-baseline atom interferometer gravitation antenna". In: *International Journal of Modern Physics D* 29.04 (2020), p. 1940005. DOI: 10.1142/S0218271819400054. eprint: https://doi.org/10.1142/S0218271819400054. URL: https://doi.org/10.1142/S0218271819400054.

[111] B. Canuel et al. "ELGAR - A European Laboratory for Gravitation and Atom-interferometric Research". In: *Classical and Quantum Gravity* 37 (22 Nov. 2020). ISSN: 13616382. DOI: 10.1088/1361-6382/aba80e.

[112] G. Arduini et al. "A Long-Baseline Atom Interferometer at CERN: Conceptual Feasibility Study". In: (Apr. 2023). http://arxiv.org/abs/2304.00614. arXiv: 2304.00614 [physics.atom-ph].

[113] Holger Ahlers et al. *STE-QUEST: Space Time Explorer and QUantum Equivalence principle Space Test*. 2022. arXiv: 2211.15412 [physics.space-ph]. URL: https://arxiv.org/abs/2211.15412.

[114] C.S Adams, M Sigel, and J Mlynek. "Atom optics". In: *Physics Reports* 240.3 (1994), pp. 143–210. ISSN: 0370-1573. DOI: https://doi.org/10.1016/0370-1573(94)90066-3. URL: https://www.sciencedirect.com/science/article/pii/0370157394900663.

[115] B. J. DeSalvo et al. "Degenerate Fermi Gas of ^{87}Sr". In: *Phys. Rev. Lett.* 105 (3 July 2010), p. 030402. DOI: 10.1103/PhysRevLett.105.030402. URL: https://link.aps.org/doi/10.1103/PhysRevLett.105.030402.

[116] R. Jördens et al. *ARTIQ*. https://m-labs.hk/artiq/. 2023.

[117] Patrick Alken, Erwan Thébault, C. D. Beggan, et al. "International Geomagnetic Reference Field: the thirteenth generation". In: *Earth, Planets and Space* 73 (2021), p. 49. DOI: 10.1186/s40623-020-01288-x. URL: https://doi.org/10.1186/s40623-020-01288-x.

[118] British Geological Survey. *The Earth's Magnetic Field: An Overview*. https://geomag.bgs.ac.uk/education/earthmag.html. Accessed: 2025-01-14. 2025.

[119] British Geological Survey. *IGRF Magnetic Field Calculator*. Accessed: 2025-01-14. 2025. URL: https://geomag.bgs.ac.uk/data_service/models_compass/igrf_calc.html.

[120] M. Misakian. "Equations for the Magnetic Field Produced by One or More Rectangular Loops of Wire in the Same Plane". In: *Journal of Research of the National Institute of Standards and Technology* 105.4 (Aug. 2000), pp. 557–564. DOI: 10.6028/jres.105.045.

[121] Sheng-wey Chiow et al. "102$\hbar k$ Large Area Atom Interferometers". In: *Phys. Rev. Lett.* 107 (13 Sept. 2011), p. 130403. DOI: 10.1103/PhysRevLett.107.130403. URL: https://link.aps.org/doi/10.1103/PhysRevLett.107.130403.

[122] Eric D. Black. "An introduction to Pound–Drever–Hall laser frequency stabilization". In: *American Journal of Physics* 69 (1 Jan. 2001), pp. 79–87. ISSN: 0002-9505. DOI: 10.1119/1.1286663.

[123] D. T. C. Allcock et al. “Urukul – Open-source Frequency Synthesizer Module for Quantum Physics”. In: *International Journal of Electronics and Telecommunications* (2023). URL: https://api.semanticscholar.org/CorpusID:260046786.

[124] John P. Bartolotta et al. “Laser cooling by sawtooth-wave adiabatic passage”. In: *Physical Review A* 98 (2 Aug. 2018). ISSN: 24699934. DOI: 10.1103/PhysRevA.98.023404.

[125] S. Snigirev et al. “Fast and dense magneto-optical traps for strontium”. In: *Physical Review A* 99 (6 June 2019). ISSN: 24699934. DOI: 10.1103/PhysRevA.99.063421.

[126] Takashi Mukaiyama et al. “Recoil-Limited Laser Cooling of 87Sr Atoms near the Fermi Temperature”. In: *Physical Review Letters* 90 (11 2003), p. 4. ISSN: 10797114. DOI: 10.1103/PhysRevLett.90.113002.

[127] H. L. Stover and W. H. Steier. “Locking of laser oscillators by light injection”. In: *Applied Physics Letters* 8 (4 1966), pp. 91–93. ISSN: 00036951. DOI: 10.1063/1.1754502.

[128] Fei Yuan. *Injection-Locking of Oscillators: An Overview*. Springer International Publishing, 2020, pp. 1–23. DOI: 10.1007/978-3-030-17364-7.

[129] Zhixin Liu and Radan Slavík. “Optical Injection Locking: From Principle to Applications”. In: *Journal of Lightwave Technology* 38.1 (2020), pp. 43–59. DOI: 10.1109/JLT.2019.2945718.

[130] Mark W. Fleming and Aram Mooradian. “Spectral Characteristics of External-Cavity Controlled Semiconductor Lasers”. In: *IEEE Journal of Quantum Electronics* 17 (1 1981), pp. 44–59. ISSN: 15581713. DOI: 10.1109/JQE.1981.1070634.

[131] Ziting Chen et al. “Active control of a diode laser with injection locking using a laser line filter”. In: *Review of Scientific Instruments* 92.12 (Dec. 2021), p. 123005. ISSN: 0034-6748. DOI: 10.1063/5.0057245. eprint: https://pubs.aip.org/aip/rsi/article-pdf/doi/10.1063/5.0057245/16133228/123005_1_online.pdf. URL: https://doi.org/10.1063/5.0057245.

[132] Gunjan Verma et al. “A scalable laser system at 461 nm for laser cooling and trapping of Sr atoms”. In: *Applied Physics B* 128 (May 2022). DOI: 10.1007/s00340-022-07815-w.

[133] Umang Mishra et al. “Monitoring and active stabilization of laser injection locking using beam ellipticity”. In: *Opt. Lett.* 48.15 (Aug. 2023), pp. 3973–3976. DOI: 10.1364/OL.495553. URL: https://opg.optica.org/ol/abstract.cfm?URI=ol-48-15-3973.

[134] F. Mogensen, H. Olesen, and G. Jacobsen. “Locking conditions and stability properties for a semiconductor laser with external light injection”. In: *IEEE Journal of Quantum Electronics* 21.7 (1985), pp. 784–793. DOI: 10.1109/JQE.1985.1072760.

[135] S.W. Henderson et al. “Coherent laser radar at 2 mu m using solid-state lasers”. In: *IEEE Transactions on Geoscience and Remote Sensing* 31.1 (1993), pp. 4–15. DOI: 10.1109/36.210439.

[136] Steven Chu et al. “Three-dimensional viscous confinement and cooling of atoms by resonance radiation pressure”. In: *Phys. Rev. Lett.* 55 (1 July 1985), pp. 48–51. DOI: 10.1103/PhysRevLett.55.48. URL: https://link.aps.org/doi/10.1103/PhysRevLett.55.48.

[137] William D. Phillips, John V. Prodan, and Harold J. Metcalf. “Laser cooling and electromagnetic trapping of neutral atoms”. In: *J. Opt. Soc. Am. B* 2.11 (Nov. 1985), pp. 1751–1767. DOI: 10.1364/JOSAB.2.001751. URL: https://opg.optica.org/josab/abstract.cfm?URI=josab-2-11-1751.

[138] J. Dalibard and C. Cohen-Tannoudji. “Laser cooling below the Doppler limit by polarization gradients: simple theoretical models”. In: *J. Opt. Soc. Am. B* 6.11 (Nov. 1989), pp. 2023–2045. DOI: 10.1364/JOSAB.6.002023. URL: https://opg.optica.org/josab/abstract.cfm?URI=josab-6-11-2023.

[139] C.J. Foot. *Atomic Physics*. Oxford Master Series in Physics. OUP Oxford, 2005. ISBN: 9780198506959. URL: https://books.google.co.uk/books?id=_CoSDAAAQBAJ.

[140] William D. Phillips. “Laser cooling and trapping of neutral atoms”. In: *Rev. Mod. Phys.* 70 (3 July 1998), pp. 721–741. DOI: 10.1103/RevModPhys.70.721. URL: https://link.aps.org/doi/10.1103/RevModPhys.70.721.

[141] D. J. Wineland and Wayne M. Itano. “Laser cooling of atoms”. In: *Phys. Rev. A* 20 (4 Oct. 1979), pp. 1521–1540. DOI: 10.1103/PhysRevA.20.1521. URL: https://link.aps.org/doi/10.1103/PhysRevA.20.1521.

[142] Y. Castin, H. Wallis, and J. Dalibard. “Limit of Doppler cooling”. In: *J. Opt. Soc. Am. B* 6.11 (Nov. 1989), pp. 2046–2057. DOI: 10.1364/JOSAB.6.002046. URL: https://opg.optica.org/josab/abstract.cfm?URI=josab-6-11-2046.

[143] Claude N. Cohen-Tannoudji. “Nobel Lecture: Manipulating atoms with photons”. In: *Rev. Mod. Phys.* 70 (3 July 1998), pp. 707–719. DOI: 10.1103/RevModPhys.70.707. URL: https://link.aps.org/doi/10.1103/RevModPhys.70.707.

[144] P. D. Lett et al. “Optical molasses”. In: *J. Opt. Soc. Am. B* 6.11 (Nov. 1989), pp. 2084–2107. DOI: 10.1364/JOSAB.6.002084. URL: https://opg.optica.org/josab/abstract.cfm?URI=josab-6-11-2084.

[145] C.S. Adams and E. Riis. “Laser cooling and trapping of neutral atoms”. In: *Progress in Quantum Electronics* 21.1 (1997), pp. 1–79. ISSN: 0079-6727. DOI: https://doi.org/10.1016/S0079-6727(96)00006-7. URL: https://www.sciencedirect.com/science/article/pii/S0079672796000067.

[146] Rodney Loudon. *The Quantum Theory of Light*. Oxford University Press, Sept. 2000. ISBN: 9780198501770. DOI: 10.1093/oso/9780198501770.001.0001. URL: https://doi.org/10.1093/oso/9780198501770.001.0001.

[147] Gilbert Grynberg, Alain Aspect, and Claude Fabre. *Introduction to Quantum Optics: From the Semi-classical Approach to Quantized Light*. Cambridge University Press, 2010.

[148] E. L. Raab et al. “Trapping of Neutral Sodium Atoms with Radiation Pressure”. In: *Phys. Rev. Lett.* 59 (23 Dec. 1987), pp. 2631–2634. DOI: 10.1103/PhysRevLett.59.2631. URL: https://link.aps.org/doi/10.1103/PhysRevLett.59.2631.

[149] Harold Metcalf. "Magneto-optical trapping and its application to helium metastables". In: *J. Opt. Soc. Am. B* 6.11 (Nov. 1989), pp. 2206–2210. DOI: 10.1364/JOSAB.6.002206. URL: https://opg.optica.org/josab/abstract.cfm?URI=josab-6-11-2206.

[150] Tomasz M. Brzozowski et al. "Time-of-flight measurement of the temperature of cold atoms for short trap-probe beam distances". In: *Journal of Optics B: Quantum and Semiclassical Optics* 4 (1 Feb. 2002), pp. 62–66. ISSN: 14644266. DOI: 10.1088/1464-4266/4/1/310.

[151] Hidetoshi Katori et al. "Magneto-Optical Trapping and Cooling of Strontium Atoms down to the Photon Recoil Temperature". In: *Phys. Rev. Lett.* 82 (6 Feb. 1999), pp. 1116–1119. DOI: 10.1103/PhysRevLett.82.1116. URL: https://link.aps.org/doi/10.1103/PhysRevLett.82.1116.

[152] C. F. A. Baynham et al. *A Prototype Atom Interferometer to Detect Dark Matter and Gravitational Waves*. 2025. arXiv: 2504.09158 [hep-ex]. URL: https://arxiv.org/abs/2504.09158.

[153] Alexander Aeppli et al. "Clock with 8×10^{-19} Systematic Uncertainty". In: *Phys. Rev. Lett.* 133 (2 July 2024), p. 023401. DOI: 10.1103/PhysRevLett.133.023401. URL: https://link.aps.org/doi/10.1103/PhysRevLett.133.023401.

[154] Jean-Philippe Uzan. "The Fundamental Constants and Their Variation: Observational Status and Theoretical Motivations". In: *Rev. Mod. Phys.* 75 (2003), p. 403. DOI: 10.1103/RevModPhys.75.403. arXiv: hep-ph/0205340.

[155] Jean-Philippe Uzan. *Varying Constants, Gravitation and Cosmology*. 2011. URL: http://www.livingreviews.org/lrr-2011-2http://www2.iap.fr/users/uzan/.

[156] M. S. Safronova et al. "Search for new physics with atoms and molecules". In: *Reviews of Modern Physics* 90 (2 June 2018), p. 025008. ISSN: 0034-6861. DOI: 10.1103/RevModPhys.90.025008. URL: http://arxiv.org/abs/1710.01833%20http://dx.doi.org/10.1103/RevModPhys.90.025008%20https://link.aps.org/doi/10.1103/RevModPhys.90.025008.

[157] Marianna S. Safronova. *The Search for Variation of Fundamental Constants with Clocks*. May 2019. DOI: 10.1002/andp.201800364.

[158] N. Huntemann et al. "Improved Limit on a Temporal Variation of m_p/m_e from Comparisons of Yb^+ and Cs Atomic Clocks". In: *Phys. Rev. Lett.* 113 (21 Nov. 2014), p. 210802. DOI: 10.1103/PhysRevLett.113.210802. URL: https://link.aps.org/doi/10.1103/PhysRevLett.113.210802.

[159] Giovanni Barontini et al. "Measuring the stability of fundamental constants with a network of clocks". In: *EPJ Quantum Technology* 9 (Dec. 2022). DOI: 10.1140/epjqt/s40507-022-00130-5.

[160] Andrew D. Ludlow et al. "Optical atomic clocks". In: *Reviews of Modern Physics* 87 (2 June 2015). ISSN: 15390756. DOI: 10.1103/RevModPhys.87.637.

[161] M. Fischer et al. "New limits on the drift of fundamental constants from laboratory measurements". In: *Physical Review Letters* 92 (23 June 2004). ISSN: 00319007. DOI: 10.1103/PhysRevLett.92.230802.

[162] R. M. Godun et al. "Frequency Ratio of Two Optical Clock Transitions in $^{171}Yb^+$ and Constraints on the Time Variation of Fundamental Constants". In: *Phys. Rev. Lett.* 113 (21 Nov. 2014), p. 210801. DOI: 10.1103/PhysRevLett.113.210801. URL: https://link.aps.org/doi/10.1103/PhysRevLett.113.210801.

[163] Asimina Arvanitaki, Junwu Huang, and Ken Van Tilburg. "Searching for dilaton dark matter with atomic clocks". In: *Phys. Rev. D* 91.1 (2015), p. 015015. DOI: 10.1103/PhysRevD.91.015015. arXiv: 1405.2925 [hep-ph].

[164] Ken Van Tilburg et al. "Search for ultralight scalar dark matter with atomic spectroscopy". In: *Phys. Rev. Lett.* 115.1 (2015), p. 011802. DOI: 10.1103/PhysRevLett.115.011802. arXiv: 1503.06886 [physics.atom-ph].

[165] R. Le Targat et al. "Experimental realization of an optical second with strontium lattice clocks". In: *Nature Communications* 4 (2013). ISSN: 20411723. DOI: 10.1038/ncomms3109.

[166] Neil Ashby, Thomas E. Parker, and Bijunath R. Patla. "A null test of general relativity based on a long-term comparison of atomic transition frequencies". In: *Nature Physics* 14 (8 Aug. 2018), pp. 822–826. ISSN: 17452481. DOI: 10.1038/s41567-018-0156-2.

[167] R. Lange et al. "Improved Limits for Violations of Local Position Invariance from Atomic Clock Comparisons". In: *Physical Review Letters* 126 (1 Jan. 2021). ISSN: 10797114. DOI: 10.1103/PhysRevLett.126.011102.

[168] Bureau International des Poids et Mesures (BIPM). *BIPM Annual Report 2020*. 2020. URL: https://webtai.bipm.org/ftp/pub/tai/annual-reports/bipm-annual-report/annual_report_2020.pdf.

[169] G. Barontini et al. "QSNET, a network of clocks for measuring the stability of fundamental constants". In: *Quantum Technology: Driving Commercialisation of an Enabling Science II*. Ed. by Miles J. Padgett et al. Vol. 11881. International Society for Optics and Photonics. SPIE, 2021, 118810K. DOI: 10.1117/12.2600493. URL: https://doi.org/10.1117/12.2600493.

[170] Kyle Beloy et al. "Frequency ratio measurements at 18-digit accuracy using an optical clock network". In: *Nature* 591.7851 (2021), pp. 564–569. DOI: 10.1038/s41586-021-03253-4. arXiv: 2005.14694 [physics.atom-ph].

[171] Bureau International des Poids et Mesures (BIPM). *BIPM - Bureau International des Poids et Mesures*. https://www.bipm.org/en/. Accessed: 23-October-2024.

[172] Masatoshi Kajita. "The fundamentals of an atomic clock". In: IOP Publishing, Sept. 2018, pp. 3-1-3–27. DOI: 10.1088/978-0-7503-2124-2ch3.

[173] William Riley and David Howe. *Handbook of Frequency Stability Analysis*. July 2008. URL: https://tsapps.nist.gov/publication/get_pdf.cfm?pub_id=50505.

[174] Sergio Sevillano Muñoz. "A particle's perspective on screening mechanisms". In: *JCAP* 12 (2024), p. 052. DOI: 10.1088/1475-7516/2024/12/052. arXiv: 2407.08779 [hep-ph].

[175] T. A. Wagner et al. “Torsion-balance tests of the weak equivalence principle”. In: *Class. Quant. Grav.* 29 (2012), p. 184002. DOI: 10.1088/0264-9381/29/18/184002. arXiv: 1207.2442 [gr-qc].

[176] Joel Bergé et al. “MICROSCOPE Mission: First Constraints on the Violation of the Weak Equivalence Principle by a Light Scalar Dilaton”. In: *Phys. Rev. Lett.* 120.14 (2018), p. 141101. DOI: 10.1103/PhysRevLett.120.141101. arXiv: 1712.00483 [gr-qc].

[177] Pierre Touboul et al. “MICROSCOPE Mission: Final Results of the Test of the Equivalence Principle”. In: *Phys. Rev. Lett.* 129.12 (2022), p. 121102. DOI: 10.1103/PhysRevLett.129.121102. arXiv: 2209.15487 [gr-qc].

[178] A. I. Vainshtein. “To the problem of nonvanishing gravitation mass”. In: *Phys. Lett.* 39B (1972), pp. 393–394. DOI: 10.1016/0370-2693(72)90147-5.

[179] Eugeny Babichev and Cédric Deffayet. “An introduction to the Vainshtein mechanism”. In: *Class. Quant. Grav.* 30 (2013), p. 184001. DOI: 10.1088/0264-9381/30/18/184001. arXiv: 1304.7240 [gr-qc].

[180] Justin Khoury and Amanda Weltman. “Chameleon fields: Awaiting surprises for tests of gravity in space”. In: *Phys. Rev. Lett.* 93 (2004), p. 171104. DOI: 10.1103/PhysRevLett.93.171104. arXiv: astro-ph/0309300.

[181] T. Damour and Alexander M. Polyakov. “The String dilaton and a least coupling principle”. In: *Nucl. Phys. B* 423 (1994), pp. 532–558. DOI: 10.1016/0550-3213(94)90143-0. arXiv: hep-th/9401069.

[182] Massimo Pietroni. “Dark energy condensation”. In: *Phys. Rev. D* 72 (2005), p. 043535. DOI: 10.1103/PhysRevD.72.043535. arXiv: astro-ph/0505615.

[183] Keith A. Olive and Maxim Pospelov. “Environmental dependence of masses and coupling constants”. In: *Phys. Rev. D* 77 (2008), p. 043524. DOI: 10.1103/PhysRevD.77.043524. arXiv: 0709.3825 [hep-ph].

[184] Philippe Brax et al. “Nonlinear Structure Formation with the Environmentally Dependent Dilaton”. In: *Phys. Rev. D* 83 (2011), p. 104026. DOI: 10.1103/PhysRevD.83.104026. arXiv: 1102.3692 [astro-ph.CO].

[185] Kurt Hinterbichler et al. “Symmetron Cosmology”. In: *Phys. Rev. D* 84 (2011), p. 103521. DOI: 10.1103/PhysRevD.84.103521. arXiv: 1107.2112 [astro-ph.CO].

[186] R. R. Caldwell, Rahul Dave, and Paul J. Steinhardt. “Cosmological imprint of an energy component with general equation of state”. In: *Phys. Rev. Lett.* 80 (1998), pp. 1582–1585. DOI: 10.1103/PhysRevLett.80.1582. arXiv: astro-ph/9708069.

[187] Elisa G. M. Ferreira. “Ultra-light dark matter”. In: *Astron. Astrophys. Rev.* 29.1 (2021), p. 7. DOI: 10.1007/s00159-021-00135-6. arXiv: 2005.03254 [astro-ph.CO].

[188] Kenneth Nordtvedt. “Lunar laser ranging: A Comprehensive probe of postNewtonian gravity”. In: *Villa Mondragone International School of Gravitation and Cosmology: From the Hubble Length to the Planck Length*. Jan. 2003, pp. 97–113. arXiv: gr-qc/0301024.

[189] W. F. McGrew et al. “Towards the optical second: verifying optical clocks at the SI limit”. In: *Optica* 6.4 (Apr. 2019), p. 448. DOI: 10.1364/OPTICA.6.000448. arXiv: 1811.05885 [physics.atom-ph].

[190] Nathaniel Sherrill et al. “Analysis of atomic-clock data to constrain variations of fundamental constants”. In: *New Journal of Physics* 25.9 (Sept. 2023), p. 093012. DOI: 10.1088/1367-2630/aceff6. URL: https://dx.doi.org/10.1088/1367-2630/aceff6.

[191] V. V. Flambaum et al. “Limits on variations of the quark masses, QCD scale, and fine structure constant”. In: *Phys. Rev. D* 69 (11 June 2004), p. 115006. DOI: 10.1103/PhysRevD.69.115006. URL: https://link.aps.org/doi/10.1103/PhysRevD.69.115006.

[192] V. V. Flambaum and A. F. Tedesco. “Dependence of nuclear magnetic moments on quark masses and limits on temporal variation of fundamental constants from atomic clock ex-

periments". In: *Phys. Rev. C* 73 (5 May 2006), p. 055501. DOI: 10.1103/PhysRevC.73.055501. URL: https://link.aps.org/doi/10.1103/PhysRevC.73.055501.

[193] T. H. Dinh et al. "Sensitivity of hyperfine structure to nuclear radius and quark mass variation". In: *Phys. Rev. A* 79 (5 May 2009), p. 054102. DOI: 10.1103/PhysRevA.79.054102. URL: https://link.aps.org/doi/10.1103/PhysRevA.79.054102.

[194] V. V. Flambaum and R. B. Wiringa. "Enhanced effect of quark mass variation in ^{229}Th and limits from Oklo data". In: *Phys. Rev. C* 79 (3 Mar. 2009), p. 034302. DOI: 10.1103/PhysRevC.79.034302. URL: https://link.aps.org/doi/10.1103/PhysRevC.79.034302.

[195] Gianna Panfilo. "The coordinated universal time". In: *IEEE Instrumentation and Measurement Magazine* 19.3 (2016), pp. 28–33. DOI: 10.1109/MIM.2016.7477951.

[196] G Panfilo and F Arias. "The Coordinated Universal Time (UTC)". In: *Metrologia* 56.4 (June 2019), p. 042001. DOI: 10.1088/1681-7575/ab1e68. URL: https://dx.doi.org/10.1088/1681-7575/ab1e68.

[197] Daniel Foreman-Mackey et al. "emcee: The MCMC Hammer". In: *pasp* 125.925 (Mar. 2013), p. 306. DOI: 10.1086/670067. arXiv: 1202.3665 [astro-ph.IM].

[198] Scott Dodelson and Fabian Schmidt. *Modern Cosmology*. Elsevier Science, 2020. DOI: 10.1016/C2017-0-01943-2.

[199] Colin J. Kennedy et al. "Precision Metrology Meets Cosmology: Improved Constraints on Ultralight Dark Matter from Atom-Cavity Frequency Comparisons". In: *Phys. Rev. Lett.* 125.20 (2020), p. 201302. DOI: 10.1103/PhysRevLett.125.201302. arXiv: 2008.08773 [physics.atom-ph].

[200] Takumi Kobayashi et al. "Search for Ultralight Dark Matter from Long-Term Frequency Comparisons of Optical and Microwave Atomic Clocks". In: *Physical Review Letters* 129.24 (Dec. 2022). ISSN: 1079-7114. DOI: 10.1103/physrevlett.129.241301. URL: http://dx.doi.org/10.1103/PhysRevLett.129.241301.

[201] A. Hees et al. “Searching for an oscillating massive scalar field as a dark matter candidate using atomic hyperfine frequency comparisons”. In: *Phys. Rev. Lett.* 117.6 (2016), p. 061301. DOI: 10.1103/PhysRevLett.117.061301. arXiv: 1604.08514 [gr-qc].

[202] Ciaran O’Hare. *cajohare/AxionLimits: AxionLimits*. https://cajohare.github.io/AxionLimits/. Version v1.0. July 2020. DOI: 10.5281/zenodo.3932430.

[203] Hugo Lévy and Jean-Philippe Uzan. “Testing screened scalar-tensor theories of gravity with atomic clocks”. In: *Phys. Rev. D* 111.6 (2025), p. 064012. DOI: 10.1103/PhysRevD.111.064012. arXiv: 2410.17292 [gr-qc].

[204] Austin Joyce et al. “Beyond the Cosmological Standard Model”. In: *Phys. Rept.* 568 (2015), pp. 1–98. DOI: 10.1016/j.physrep.2014.12.002. arXiv: 1407.0059 [astro-ph.CO].

[205] Yashar Akrami et al. *Modified Gravity and Cosmology. An Update by the CANTATA Network*. Ed. by Emmanuel N. Saridakis et al. Springer, 2021. arXiv: 2105.12582 [gr-qc].

[206] Philippe Brax et al. “Testing Screened Modified Gravity”. In: *Universe* 8.1 (2021), p. 11. DOI: 10.3390/universe8010011. arXiv: 2201.10817 [gr-qc].

[207] Dawid Brzeminski et al. “Searching for a fifth force with atomic and nuclear clocks”. In: *Phys. Rev. D* 106 (9 Nov. 2022), p. 095031. DOI: 10.1103/PhysRevD.106.095031. URL: https://link.aps.org/doi/10.1103/PhysRevD.106.095031.

[208] G. R. Dvali, Gregory Gabadadze, and Massimo Porrati. “4-D gravity on a brane in 5-D Minkowski space”. In: *Phys. Lett. B* 485 (2000), pp. 208–214. DOI: 10.1016/S0370-2693(00)00669-9. arXiv: hep-th/0005016.

[209] G. R. Dvali, G. Gabadadze, and M. Porrati. “Metastable gravitons and infinite volume extra dimensions”. In: *Phys. Lett. B* 484 (2000), pp. 112–118. DOI: 10.1016/S0370-2693(00)00631-6. arXiv: hep-th/0002190.

[210] Claudia de Rham et al. “Cascading gravity: Extending the Dvali-Gabadadze-Porrati model to higher dimension”. In: *Phys. Rev. Lett.* 100 (2008), p. 251603. DOI: 10.1103/PhysRevLett.100.251603. arXiv: 0711.2072 [hep-th].

[211] Claudia de Rham et al. “Cascading Gravity and Degravitation”. In: *JCAP* 02 (2008), p. 011. DOI: 10.1088/1475-7516/2008/02/011. arXiv: 0712.2821 [hep-th].

[212] Claudia de Rham, Gregory Gabadadze, and Andrew J. Tolley. “Resummation of Massive Gravity”. In: *Phys. Rev. Lett.* 106 (2011), p. 231101. DOI: 10.1103/PhysRevLett.106.231101. arXiv: 1011.1232 [hep-th].

[213] Claudia de Rham et al. “Cosmic Acceleration and the Helicity-0 Graviton”. In: *Phys. Rev. D* 83 (2011), p. 103516. DOI: 10.1103/PhysRevD.83.103516. arXiv: 1010.1780 [hep-th].

[214] Cedric Deffayet et al. “Nonperturbative continuity in graviton mass versus perturbative discontinuity”. In: *Phys. Rev. D* 65 (2002), p. 044026. DOI: 10.1103/PhysRevD.65.044026. arXiv: hep-th/0106001.

[215] Markus A. Luty, Massimo Porrati, and Riccardo Rattazzi. “Strong interactions and stability in the DGP model”. In: *JHEP* 09 (2003), p. 029. DOI: 10.1088/1126-6708/2003/09/029. arXiv: hep-th/0303116.

[216] Alberto Nicolis, Riccardo Rattazzi, and Enrico Trincherini. “The Galileon as a local modification of gravity”. In: *Phys. Rev. D* 79 (2009), p. 064036. DOI: 10.1103/PhysRevD.79.064036. arXiv: 0811.2197 [hep-th].

[217] Claudia de Rham and Andrew J. Tolley. “DBI and the Galileon reunited”. In: *JCAP* 05 (2010), p. 015. DOI: 10.1088/1475-7516/2010/05/015. arXiv: 1003.5917 [hep-th].

[218] Claudia de Rham et al. “Graviton Mass Bounds”. In: *Rev. Mod. Phys.* 89.2 (2017), p. 025004. DOI: 10.1103/RevModPhys.89.025004. arXiv: 1606.08462 [astro-ph.CO].

[219] Gia Dvali, Andrei Gruzinov, and Matias Zaldarriaga. “The Accelerated universe and the moon”. In: *Phys. Rev. D* 68 (2003), p. 024012. DOI: 10.1103/PhysRevD.68.024012. arXiv: hep-ph/0212069.

[220] Philippe Brax, Clare Burrage, and Anne-Christine Davis. “Laboratory Tests of the Galileon”. In: *JCAP* 09 (2011), p. 020. DOI: 10.1088/1475-7516/2011/09/020. arXiv: 1106.1573 [hep-ph].

[221] Shinji Tsujikawa. "Lunar Laser Ranging constraints on nonminimally coupled dark energy and standard sirens". In: *Phys. Rev. D* 100.4 (2019), p. 043510. DOI: 10.1103/PhysRevD.100.043510. arXiv: 1903.07092 [gr-qc].

[222] John D. Barrow and David F. Mota. "Gauge invariant perturbations of varying alpha cosmologies". In: *Class. Quant. Grav.* 20 (2003), pp. 2045–2062. DOI: 10.1088/0264-9381/20/11/307. arXiv: gr-qc/0212032.

[223] Soumya Chakrabarti. "Cosmic variation of proton-to-electron mass ratio with an interacting Higgs scalar field". In: *Mon. Not. Roy. Astron. Soc.* 506.2 (2021), pp. 2518–2532. DOI: 10.1093/mnras/stab1910. arXiv: 2107.00543 [gr-qc].

[224] A. G. Adame et al. "DESI 2024 VI: cosmological constraints from the measurements of baryon acoustic oscillations". In: *JCAP* 02 (2025), p. 021. DOI: 10.1088/1475-7516/2025/02/021. arXiv: 2404.03002 [astro-ph.CO].

[225] Peter W. Graham et al. "Dark Matter Direct Detection with Accelerometers". In: *Phys. Rev. D* 93.7 (2016), p. 075029. DOI: 10.1103/PhysRevD.93.075029. arXiv: 1512.06165 [hep-ph].

[226] David J. E. Marsh. "Measuring the Quantum State of Dark Matter". In: *Annalen Phys.* 536.1 (2024), p. 2200609. DOI: 10.1002/andp.202200609. arXiv: 2211.13602 [hep-ph].

[227] E. G. Adelberger, Blayne R. Heckel, and A. E. Nelson. "Tests of the gravitational inverse square law". In: *Ann. Rev. Nucl. Part. Sci.* 53 (2003), pp. 77–121. DOI: 10.1146/annurev.nucl.53.041002.110503. arXiv: hep-ph/0307284.

[228] Oliver Buchmueller, John Ellis, and Ulrich Schneider. "Large-scale atom interferometry for fundamental physics". In: *Contemp. Phys.* 64.2 (2023), pp. 93–110. DOI: 10.1080/00107514.2023.2239008. arXiv: 2306.17726 [astro-ph.CO].

[229] *Clock constraints on fundamental physics*. Zenodo code repository, 10.5281/zenodo.15175279. DOI: 10.5281/zenodo.15175279.

[230] J. C. Berengut et al. “Optical Transitions in Highly Charged Californium Ions with High Sensitivity to Variation of the Fine-Structure Constant”. In: *Phys. Rev. Lett.* 109 (7 Aug. 2012), p. 070802. DOI: 10.1103/PhysRevLett.109.070802. URL: https://link.aps.org/doi/10.1103/PhysRevLett.109.070802.

[231] S. G. Porsev et al. “Optical clocks based on the Cf^{15+} and Cf^{17+} ions”. In: *Phys. Rev. A* 102 (1 July 2020), p. 012802. DOI: 10.1103/PhysRevA.102.012802. URL: https://link.aps.org/doi/10.1103/PhysRevA.102.012802.

[232] J. C. Berengut, V. A. Dzuba, and V. V. Flambaum. “Enhanced Laboratory Sensitivity to Variation of the Fine-Structure Constant using Highly Charged Ions”. In: *Phys. Rev. Lett.* 105 (12 Sept. 2010), p. 120801. DOI: 10.1103/PhysRevLett.105.120801. URL: https://link.aps.org/doi/10.1103/PhysRevLett.105.120801.

[233] M. G. Kozlov et al. “Highly charged ions: Optical clocks and applications in fundamental physics”. In: *Rev. Mod. Phys.* 90 (4 Dec. 2018), p. 045005. DOI: 10.1103/RevModPhys.90.045005. URL: https://link.aps.org/doi/10.1103/RevModPhys.90.045005.

[234] V. V. Flambaum. “Enhanced Effect of Temporal Variation of the Fine Structure Constant and the Strong Interaction in ^{229}Th”. In: *Phys. Rev. Lett.* 97 (9 Aug. 2006), p. 092502. DOI: 10.1103/PhysRevLett.97.092502. URL: https://link.aps.org/doi/10.1103/PhysRevLett.97.092502.

[235] E Peik et al. “Nuclear clocks for testing fundamental physics”. In: *Quantum Science and Technology* 6.3 (Apr. 2021), p. 034002. DOI: 10.1088/2058-9565/abe9c2. URL: https://dx.doi.org/10.1088/2058-9565/abe9c2.

[236] Chuankun Zhang et al. “Frequency ratio of the 229mTh nuclear isomeric transition and the 87Sr atomic clock”. In: *Nature* 633.8028 (Sept. 2024), pp. 63–70. ISSN: 1476-4687. DOI: 10.1038/s41586-024-07839-6. URL: https://doi.org/10.1038/s41586-024-07839-6.

[237] Pavel Fadeev, Julian C. Berengut, and Victor V. Flambaum. “Sensitivity of ^{229}Th nuclear clock transition to variation of the fine-structure constant”. In: *Phys. Rev. A* 102 (5 Nov.

2020), p. 052833. DOI: 10.1103/PhysRevA.102.052833. URL: https://link.aps.org/doi/10.1103/PhysRevA.102.052833.

[238] C. J. Campbell et al. "Single-Ion Nuclear Clock for Metrology at the 19th Decimal Place". In: *Phys. Rev. Lett.* 108 (12 Mar. 2012), p. 120802. DOI: 10.1103/PhysRevLett.108.120802. URL: https://link.aps.org/doi/10.1103/PhysRevLett.108.120802.

[239] G A Kazakov et al. "Performance of a 229Thorium solid-state nuclear clock". In: *New Journal of Physics* 14.8 (Aug. 2012), p. 083019. DOI: 10.1088/1367-2630/14/8/083019. URL: https://dx.doi.org/10.1088/1367-2630/14/8/083019.

[240] Bureau International des Poids et Mesures. *Explanatory Supplement to the International Atomic Time (TAI)*. 2021. URL: https://webtai.bipm.org/ftp/pub/tai/other-products/notes/explanatory_supplement_v0.6.pdf.

[241] Huidong Kim et al. "Absolute frequency measurement of the 171Yb optical lattice clock at KRISS using TAI for over a year". In: *Metrologia* 58.5 (Aug. 2021), p. 055007. DOI: 10.1088/1681-7575/ac1950. URL: https://dx.doi.org/10.1088/1681-7575/ac1950.

[242] Marco Schioppo et al. "Ultrastable optical clock with two cold-atom ensembles". In: *Nature Photonics* 11.1 (2017), pp. 48–52. DOI: 10.1038/nphoton.2016.231. URL: https://doi.org/10.1038/nphoton.2016.231.

[243] W. F. McGrew et al. "Atomic clock performance enabling geodesy below the centimetre level". In: *Nature* 564.7734 (2018), pp. 87–90. DOI: 10.1038/s41586-018-0738-2. URL: https://doi.org/10.1038/s41586-018-0738-2.

[244] Marianna S. Safronova et al. "Two Clock Transitions in Neutral Yb for the Highest Sensitivity to Variations of the Fine-Structure Constant". In: *Phys. Rev. Lett.* 120 (17 Apr. 2018), p. 173001. DOI: 10.1103/PhysRevLett.120.173001. URL: https://link.aps.org/doi/10.1103/PhysRevLett.120.173001.

[245] Christian Sanner et al. “Optical clock comparison for Lorentz symmetry testing”. In: *Nature* 567 (2019), pp. 204–208. DOI: 10.1038/s41586-019-0972-2. URL: https://www.nature.com/articles/s41586-019-0972-2.

[246] M. Filzinger et al. “Improved Limits on the Coupling of Ultralight Bosonic Dark Matter to Photons from Optical Atomic Clock Comparisons”. In: *Phys. Rev. Lett.* 130 (25 June 2023), p. 253001. DOI: 10.1103/PhysRevLett.130.253001. URL: https://link.aps.org/doi/10.1103/PhysRevLett.130.253001.

[247] A Tofful et al. “171Yb+ optical clock with 2.2×10^{-18} systematic uncertainty and absolute frequency measurements”. In: *Metrologia* 61.4 (June 2024), p. 045001. DOI: 10.1088/1681-7575/ad53cd. URL: https://dx.doi.org/10.1088/1681-7575/ad53cd.

[248] Tobias Bothwell et al. “JILA SrI optical lattice clock with uncertainty of 2.0×10^{-18}”. In: *Metrologia* 56.6 (Oct. 2019), p. 065004. DOI: 10.1088/1681-7575/ab4089. URL: https://dx.doi.org/10.1088/1681-7575/ab4089.

[249] L. Sonderhouse et al. “Demonstration of 4.8×10^{-17} stability at 1 s for two independent optical clocks”. In: *Nature Photonics* 13.10 (2019), pp. 714–719. DOI: 10.1038/s41566-019-0493-4. URL: https://doi.org/10.1038/s41566-019-0493-4.

[250] K Szymaniec et al. “NPL Cs fountain frequency standards and the quest for the ultimate accuracy”. In: *Journal of Physics: Conference Series* 723.1 (June 2016), p. 012003. DOI: 10.1088/1742-6596/723/1/012003. URL: https://dx.doi.org/10.1088/1742-6596/723/1/012003.

[251] S Weyers et al. “Advances in the accuracy, stability, and reliability of the PTB primary fountain clocks”. In: *Metrologia* 55.6 (Oct. 2018), p. 789. DOI: 10.1088/1681-7575/aae008. URL: https://dx.doi.org/10.1088/1681-7575/aae008.

Appendix A

From Circular T data to $\Delta\mu/\mu$

Circular T reports the fractional deviation d of the scale interval of the International Atomic Time (TAI) with respect to the SI second on the geoid (or Terrestrial Time (TT)). This quantity reflects how much the length of one second in TAI differs from the SI second (in the time domain). This quantity relates to the fractional frequency deviation of TAI as follows:

$$d = -y_{\mathrm{TAI}} = \frac{\text{length of 1s in TAI} - \text{length of 1s in TT}}{\text{length of 1s in TT}}. \tag{A.1}$$

The values of d for individual Primary Frequency Standards (PFS) and Secondary Frequency Standards (SFS) contributions are also published. These values denote the second as realized by each standard, and they compare TAI frequency with that of the given Primary and Secondary Frequency Standards (PFS/SFS). These are found in Section 3 of the

Circular T datasheets [240]. We define the value of d_i for individual standards as:

$$d_i \approx -y_i = \frac{f_i}{f_{\mathrm{TAI}}} - 1\,, \tag{A.2}$$

with

$$f_i := \frac{\nu_i}{\nu_{i,0}}, \tag{A.3}$$

where ν_i is the measured frequency and $\nu_{i,0}$ is the nominal frequency of the atomic transition.

We will only use the values for d for optical atomic clocks, i.e. strontium and ytterbium, for which $K_\mu = 0$. We assume that the dominant contribution to f_{TAI} is from Caesium-based clocks that use a microwave transition with $K_\mu = -1$. In this way, using Eq. (5.6) we can assume that $\frac{\Delta\mu}{\mu} = -d$ (based on the sensitivities of optical and microwave clocks to variations of μ (Table B.1).

Whether a clock contributes to Circular T depends on whether it runs in a given month and whether data is submitted for the calculation of UTC. Secondary Frequency Standards based on optical transitions do not typically contribute as regularly as microwave standards, leading to long gaps sometimes of many months between datapoints. A graphical representation of all the Primary and Secondary Frequency Standards evaluations reported since September 2003 is shown on the BIPM website [1].

One value for d is recorded for each frequency standard, i.e. each atomic clock, per month (if the clock was running that month). Fractional uptimes for each clock are also reported monthly (section 3 of the datasheets). Up-to-date tables containing all the available data for each clock can be found on the BIPM website [2]. Figure A.1 shows the values for d

[1] https://webtai.bipm.org/database/show_psfs.html
[2] https://webtai.bipm.org/ftp/pub/tai/other-products/taipsfs/

for all the optical clocks reported in Circular T up to the time of writing. The value of d is reported along with several uncertainty values, which are then summed in quadrature to obtain the final error reported for the values of d. The uncertainties reported are that of the instability of the standard, the combined uncertainty from systematic effects, uncertainties in the link between the TAI-participating clock and the standard relating to dead time and systematic effects and the uncertainty in the link to TAI [240].

The date in Circular T is reported in Modified Julian Date MJD (start and end for each period of estimation). MJD gives the number of days since midnight on November 17 1858. For the modified gravity case, the phase of the sinusoidal signal is defined by the time that aphelion/perihelion happens during the year. Perihelion and aphelion times vary from year to year. Table A.1 gives an average time of when perihelion and aphelion occur during the year and the corresponding phase in terms of days since the beginning of the MJD calendar.

	Perihelion	Aphelion
Date	4 January	5 July
Phase	48 days	230 days

Table A.1: Average time of the year that perihelion and aphelion happen. The number of days from the beginning of the MJD calendar to the first instance of perihelion and aphelion are also reported as phases.

The phase could be set to 48 days but since we have data from 2016 onwards, the MJD day that the perihelion happens in the data (4 January 2017 in MJD = 57757) can be subtracted from the data and then fit the equation without the phase.

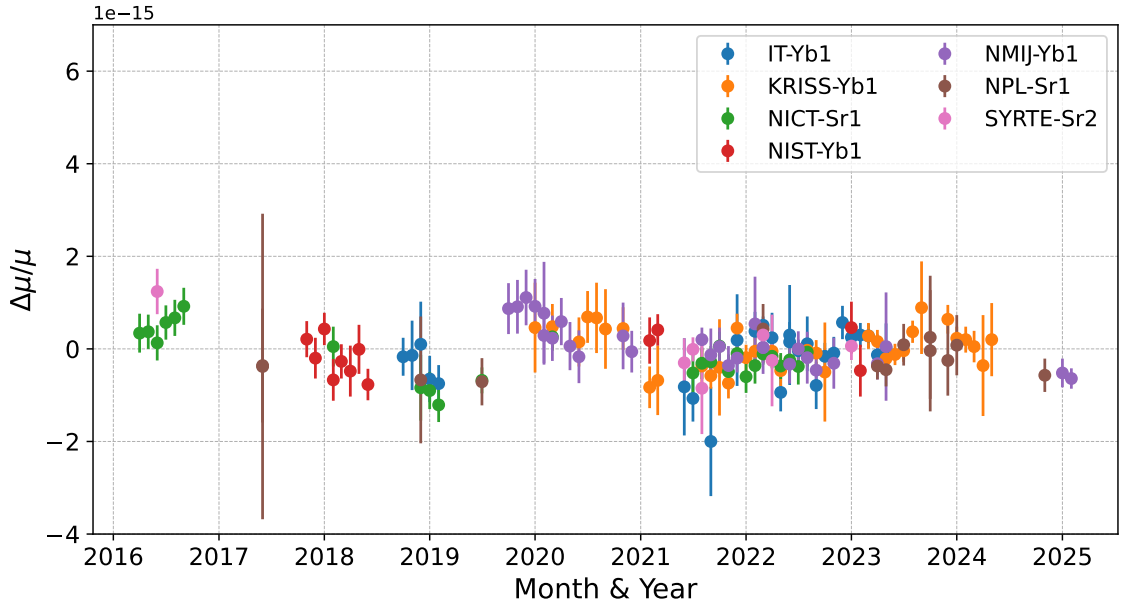

Figure A.1: Plot of $\frac{\Delta\mu}{\mu}$ $(= -d)$ vs month and year for each optical clock used in the analysis.

Appendix B

Current Clock Characteristics

Table B.1 presents different species of clocks and their sensitivity to variation in α and μ along with the clock instability and accuracy (systematic uncertainty).

There are two types of errors in frequency standards: (a) statistical errors originating from measurement fluctuations and (b) systematic uncertainties [38]. The performance of the clock is characterized by determining the (1) fractional frequency instability $\sigma_y(\tau)$ and (2) systematic frequency uncertainty. The clock stability is limited by the quantum projection noise or shot noise and thermal noise. The systematic frequency fluctuations originate from magnetic and electric fields, which induce perturbations in the natural frequencies of the atoms (e.g. Zeeman and Stark shift). More information on how noise is characterized in clocks can be found in [38, 173].

The major noise sources can be modeled as white noise and pink (flicker) frequency noise. The total noise of the system can be derived by summing all the noise terms.

In the frequency domain, the one-sided Power Spectral Density (PSD) function for frac-

tional frequency fluctuations of the clock is:

$$S_y(f) = h_0 + \frac{1}{f} h_{-1} \,. \tag{B.1}$$

where h_0 is the white frequency modulation (WFM) component (white noise) and the $\frac{1}{f} h_{-1}$ is the flicker frequency modulations (FFM) or pink noise component.

The relationship between Allan variance and PSD coefficients h_0 and h_{-1} depend on the power law model of the noise. The conversions are given by:

$$\begin{aligned} \sigma_y^2(\tau) &= \frac{1}{2\tau} h_0 \,, \\ \sigma_y^2(\tau) &= 2\ln(2) h_{-1} \,. \end{aligned} \tag{B.2}$$

Plots of the combined PSD of the clocks listed in Table B.1 are presented in Fig. B.1b. The sensitivity of different pairs of clocks to variations in μ is also presented as a function of frequency.

Clock	Instability / $\sqrt{\tau/s}$	h_0 / s	Accuracy	h_{-1}	K_α	K_μ
Yb [241]	1.4×10^{-16} [242]	4.0×10^{-32}	1.4×10^{-18} [243]	1.4×10^{-36}	0.37 [244]	0
$^{171}Yb^{+}$ [245]	1.1×10^{-15} [246]	2.4×10^{-30}	2.2×10^{-18} [247]	3.5×10^{-36}	−5.95 [244]	0
^{87}Sr [248]	4.8×10^{-17} [249]	4.6×10^{-33}	8.0×10^{-19} [153]	4.6×10^{-37}	0.06	0
^{133}Cs [250, 251]	2.5×10^{-14}	1.3×10^{-27}	$1–2 \times 10^{-16}$	2.9×10^{-32}	2.83	−1
CaF [159]	1.5×10^{-15}	4.5×10^{-30}	7.5×10^{-18}	4.1×10^{-35}	0	−0.5
N_2^+ [159]	1.2×10^{-14}	2.9×10^{-28}	3.9×10^{-18}	1.1×10^{-35}	0	−0.5

Table B.1: Clock instability and accuracy of each type of clock used in this analysis. The accuracy is defined as the systematic uncertainty of the clock or flicker noise. The coefficients of the power spectral density of the modeled white and pink noise of the clocks are also stated along with the sensitivity of each clock to variations in α and μ. The instabilities quoted here are based on state-of-the-art clock results except for the CaF and N_2^+ clocks where projections of the instability and systematic uncertainty are taken from [159].

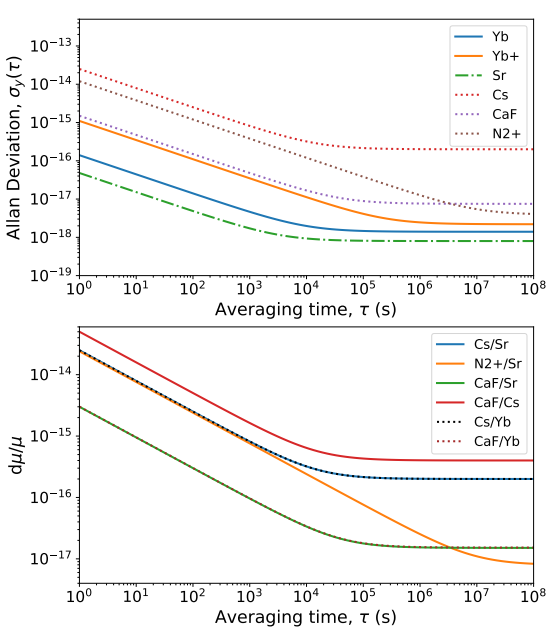

(a) Allan deviation as a function of averaging time.

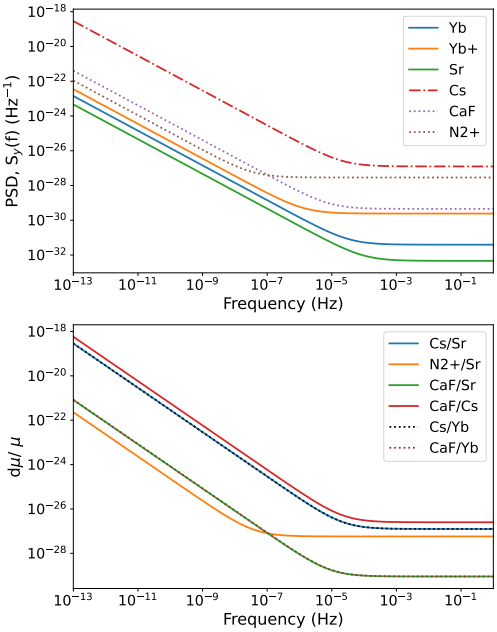

(b) Power Spectral Density as a function of frequency.

Figure B.1: (a) Allan deviation (fractional uncertainty) as a function of averaging time for different clock species. The sloped region represents white noise fluctuations (instability), while the flat region corresponds to flicker/pink noise (inaccuracy). The bottom plot illustrates sensitivities to variations in μ over time for different clock combinations. (b) Power Spectral Density as a function of frequency for different clock species. The flat region represents white noise fluctuations (instability), while the sloped region corresponds to flicker/pink noise (inaccuracy). The bottom plot shows sensitivities to variations in μ as a function of frequency for different clock combinations. Note: In both bottom plots, the Cs/Sr and Cs/Yb curves overlap, as do the CaF/Cs and CaF/Yb curves.